Title
An Exploration of the Electromechanical Response of Suspended Graphene and Its Applications

Author
Ng, Jimmy

Publication Date
2018

Peer reviewed|Thesis/dissertation

UNIVERSITY OF CALIFORNIA

Los Angeles

An Exploration of the Electromechanical Response of Suspended Graphene and Its Applications

A dissertation submitted in partial satisfaction of the

requirements for the degree Doctor of Philosophy

in Materials Science and Engineering

by

Jimmy Ng

2018

ABSTRACT OF THE DISSERTATION

An Exploration of the Electromechanical Response of Suspended Graphene and Its Applications

by

Jimmy Ng

Doctor of Philosophy in Materials Science and Engineering

University of California, Los Angeles, 2018

Professor Ya-Hong Xie, Chair

Graphene is a 2D sheet of carbon atoms arranged in a hexagonal lattice whose unique structure gives rise to extraordinary mechanical and electronic properties. For these reasons, suspended graphene structures have potential applications in micro-electromechanical systems (MEMS). This dissertation serves as an exposition exploring the electromechanical response of suspended graphene and its applications in MEMS. After a thorough introduction to graphene is provided, the dissertation presents a series of studies. First, a suspended graphene ribbon device was studied as a mechanical switch used to provide electrostatic discharge protection to

semiconductor integrated circuits, establishing proof of concept via standard electrostatic discharge industry testing. Second, the effect of polymer residue from device fabrication processes on the electromechanical response of suspended graphene was investigated. After rigorous study using innovative compliant mechanisms, polymer residue was found to have two prominent effects on suspended graphene: 1) a variation polymer residue thickness led to a variation in end device parameters such as the pull-in voltage and 2) the polymer residue itself supports the suspension of graphene by increasing the rigidity of the suspended structure. These results have implications to the manufacturability and reliability of suspended graphene MEMS devices. Finally, a theoretical study modeling the suspended graphene ribbon device was conducted for a separate application: a resonator for high frequency power conversion, an idea that was made attractive again by the extraordinary material properties of graphene. In this study, the device design, electromechanical modeling, and results relevant to high frequency power conversion applications are presented and discussed. The results indicate that a suspended graphene ribbon resonator can generate oscillation frequencies within the THz gap when the graphene sheet itself approaches sufficiently small dimensions; however, there also exists a tradeoff between the power generated and the signal quality which must be taken into account when designing these resonators. In all the studies presented, the device design, experimental procedures, algorithms for computer modeling, etc. are explained in detail. Lastly, standard semiconductor industry fabrication and characterization techniques were primarily used in doing this work, imbuing the potential for industrial large-scale adoption in the future.

The dissertation of Jimmy Ng is approved.

Jenn-Ming Yang

Ximin He

Jonathan Hopkins

Ya-Hong Xie, Committee Chair

University of California, Los Angeles

2018

Dedicated to my mother

Table of Contents

List of Figures

List of Tables

Acknowledgements

First of all, I would like to express my deepest gratitude to Professor Ya-Hong Xie for his guidance and patience in helping me navigate the arduous yet rewarding process that is a PhD. He is not only a knowledgeable professional who taught me how to conduct scientific research but also kindhearted and reliable man who instill in me these same characteristics. I cannot thank you enough for challenging me and helping me grow during my years at UCLA.

I also would like to give a warm thank you to my many collaborators. Thank you to Professor Albert Wang and his student Qi Chen from the Laboratory of Integrated Circuits and Systems at UC Riverside who I had insightful conversations with and helped me with electrical probe station measurements. Thank you to Professor Jonathan Hopkins and his student Talmage Jones from the Flexible Research Group at UCLA who we shared a wonderful collaboration with. Thank you for your extensive help designing compliant mechanisms and conducting molecular dynamics simulations to move our research forward. Thank you to Professor Kang Wang and his students Isaac Martinez-Velis and Shin-Hung (Rick) Tsai from the Device Research Laboratory at UCLA for your help in the thorough characterization of polymer residue on graphene. Thank you to Professor Yahachi Saito from Nagoya University for the opportunity to conduct scientific research in Japan; my time here was an once-in-a-lifetime opportunity. Thank you to Professor Asghar Hashmi, Professor Khalid Mahmood, and Salma Irfan for a wonderful trip in Pakistan; this was a truly eye-opening experience and was one of the highlights of my PhD. Without everyone's help, my research would not have been possible.

Next, I want to thank the members of my own research group who I worked extensively and intimately with. This list includes but is not limited to the following members: Zhongbo

Yan, Owen Liang, Jia Wang, Peiyi Ye, Pu (Penny) Wang, Xinke Yu, Ming Dong, Yao Yang, and Yiye Sun. I'd like to give a special thanks to former PhD student Wei Zhang who mentored me and passed his research project onto me, giving me the honor of continuing his work. I'd like to give a special thanks to former PhD student Ming Xia who provided extensive mentorship in semiconductor process engineering and lab management. I'd like to give a special thanks to Zirui Liu for taking over the group's semiconductor processing responsibilities after I graduate. I'd like to give a special thanks to Shan Huang for taking over the group's lab management responsibilities after I graduate. Lastly, I'd like to reserve special thanks to the people who I have the honor of mentoring: Wei (Winnie) Huang, Feng (Crystal) Ji, Hannes Funk, and Naoki Kamimura; thank you helping me grow as a mentor and teacher and I wish you all the best for the future.

Lastly, I want to thank my loved ones. Thank you to all my close friends that kept me sane through the PhD; I will never forget our board game nights, workout sessions, music festivals, and spontaneous trips. Thank you to my mother, sister, and grandmothers for raising me and allowing me to pursue this course of study. Last but not least, I'd like to thank my girlfriend and best friend, Ms. Amy Dang, for an amazing and unique experience at UCLA. Your presence allowed me not only to survive but also growth and thrive through the PhD process. Because of you, I look to the future with head held high and my heart open wide. I am truly lucky to have you.

This research was made possible by funding from NSF grants 1405558 and 1405059 and from support from the Alexander von Humboldt Foundation Research Award. I also acknowledge help from the UCLA Nanoelectronics Research Facility; without them, device

fabrication would not have been possible. We also acknowledge help from Professor Sergey Prikhodko at UCLA for permission and support in doing SEM and Raman spectroscopy.

VITA

2012 Bachelor of Arts in Physics

University of California Berkeley

Berkeley, CA

2014 Master of Science in Materials Science

University of California Los Angeles

Los Angeles, CA

Publications:

1. **Ng J.**, Jones T., Hopkins J., Xie Y.H.: 'A suspended graphene resonator for THz DC-to-AC conversion', *Submitted,* 2018.
2. **Ng J**., Jones T., Velis I., Tsai S-H., Chen Q., Wang A., Hopkins J., Xie Y.H.: 'The effects of polymer residue on the pull-in of suspended graphene', *Submitted*, 2018.
3. **Ng J**., Chen Q., Wu T., Wang A., Xie Y.H.: 'Comparative study between the fracture stress of poly- and single- crystalline graphene using a suspended NEMS structure', *IET Micro and Nano Letters,* 2017, 12, (11), pp. 907-912.
4. **Ng J.**, and Xie Y.H.: 'Source identification and method for drastic reduction of Fe contamination on wet transferred graphene', *Thin Solid Films,* 2017, 639, pp. 36-41.
5. Chen Q., **Ng J**., Cheng L., Lu F., Wang C., Zhang F., Xie Y.H., Wang, A.: 'Systematic transient characterization of graphene NEMS switch for ESD protection', *IET Micro and Nano Letters,* 2017, 12, (11), pp. 875-880.

6. Zhang W., Ma E., Chen Q., Xia M., **Ng J**., Wang A., Xie Y.H.: 'The electro-mechanical responses of suspended graphene ribbons for electrostatic discharge applications', *Applied Physics Letters*, 2016, 108, Article number: 153103.

Selected Conferences:

1. **Ng J.,** Jones T., Hopkins J., Xie Y.H.: 'A suspended graphene resonator for THz DC-to-AC conversion', *Accepted for 2018 IEEE 14th International Conference on Solid State and Integrated Circuit Technology*, 2018.
2. **Ng J.**, Chen Q., Zhang W., Ma R., Wang A., Xie Y.H: 'Optimization of suspended graphene NEMS devices for electrostatic discharge protection', *2017 IEEE 12th International Conference on Nano/Micro Engineered and Molecular Systems (NEMS)*.
3. **Ng J.**, Chen Q., Zhang W., Wang A., Xie Y.H: 'Optimization of suspended graphene NEMS devices for electrostatic discharge protection', *2017 5th International Conference on Materials Science and Nanotechnology*.
4. **Ng J.**, Chen Q., Zhang W., Wang A., Xie Y.H: 'Optimization of suspended graphene NEMS devices for electrostatic discharge protection', *2017 International Conference on Semiconductor Materials and Nano-Devices*.

Chapter 1: Introduction

1.1 Introduction to graphene

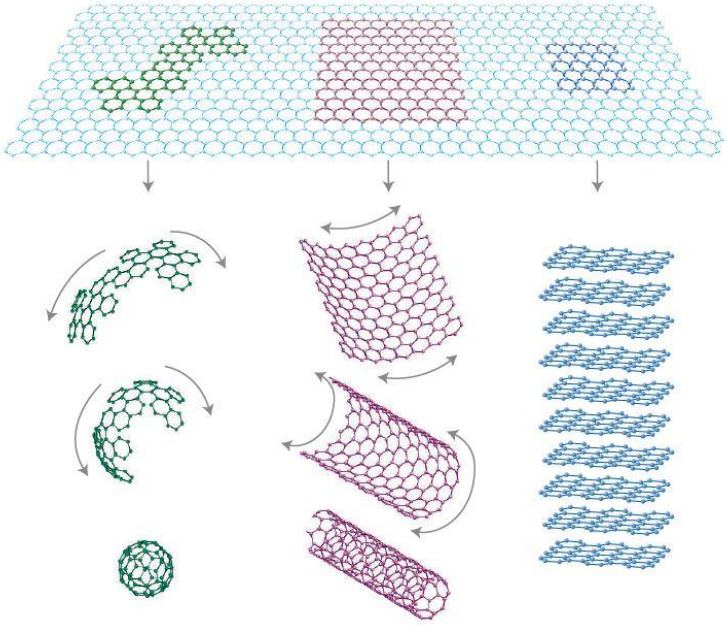

Fig. 1.1 Illustration of 2D graphene and how it serves as a building block for other carbon materials: 0D fullerenes, 1D carbon nanotubes, and 3D graphite. Courtesy of A. K. Geim and N. S. Novoselov. [1]

Graphene is a 2-dimensional sheet of carbon atoms arranged in a hexagonal lattice and serves as the building block of all other carbon materials, as seen in Fig. 1.1 [1]. It can be rolled up into 0D fullerenes [2] and 1D carbon nanotubes [3]. On the other hand, 3D graphite can be obtained by stacking layers of graphene on top of one another [1]. Graphene has been theoretically studied for the past sixty years [4-5] but was only considered an "academic material" for most of that time. This was because 2D materials were thought not to be thermodynamically stable and unable to exist. Theory by Landau and Peierls argued that thermal fluctuations in low-dimensional crystal structures should lead to displacements of atoms on the

order of inter-atomic distances at any finite temperature [4], resulting in dislocations and structural crystal defects that should destroy the material. However, in 2004, Geim and Novoselov proved previous theories incorrect when they experimentally discovered graphene [6]. Furthermore, graphene was found to be able to exist as a high quality continuous film that exhibited many of the properties predicted by theory. For their ground-breaking work, Geim and Novoselov won the 2010 Nobel Prize in Physics [1].

Since then, graphene's popularity in the research community has exploded because of its extraordinary electronic, mechanical, thermal, and chemical properties and the potential applications those properties promise [1]. For example, much work has been done on using graphene in next-generation electronics because of its high charge carrier mobility at room temperature [7]. Furthermore, due its high optical transmittance and conductivity, many have touted graphene as a replacement to indium tin-oxide, which is made using expensive rare earth metals [8]. Graphene's mechanical robustness and molecular sensitivity has prompted research on using it in various chemical and biological sensor applications [9]. The applications listed here are just several of many; unfortunately, there is not enough time to cover all of them. Instead, I will focus on the electronic and mechanical properties, as it pertains more to my research; then, I will specifically cover the applications involving the electromechanical responses of suspended graphene.

1.2 Electronic properties of graphene

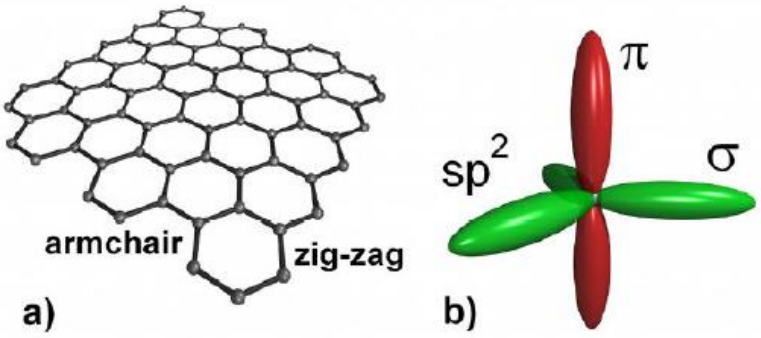

Fig. 1.2 Graphene geometry and bonding among between carbon atoms. Courtesy of Lemme et al. [10]

Graphene's two-dimensionality makes its electronic properties very different than its 3D counterpart, graphite. Its exceptional electronic properties are derived from the bonding characteristics of its carbon atoms. As seen in Fig. 1.2, each carbon atom has four valence electrons, and three out of those four electrons participate in σ-bonding with its nearest neighbor in the hexagonal lattice. The fourth valence electron occupies an orbital perpendicular to the graphene sheet, creating delocalized π-bonding. This creates a two-dimensional electron gas with high mobility within the sheet. [10]

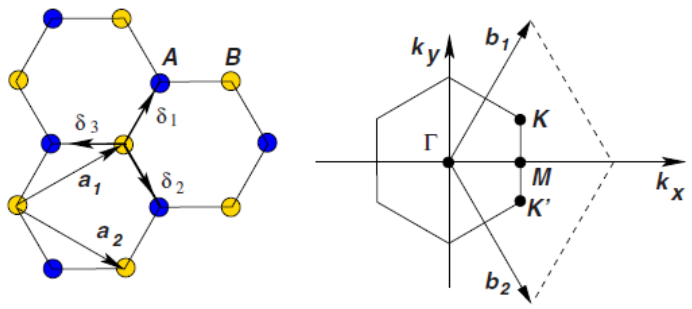

Fig. 1.3 Crystal lattice and Brillouin zone of graphene. $\mathbf{a}_1$ and $\mathbf{a}_2$ are lattice unit vectors. The Dirac cones are located at the K and K' points. Courtesy of Castro Neto et al. [11]

Next, I elaborate on graphene's band structure, which quantitatively explains its electronic properties, by beginning with the material's crystal structure. Graphene's crystal structure can be seen as a triangular lattice with a basis of 2 atoms per unit cell, as seen in Fig. 1.3. Its lattice vectors, $\mathbf{a}_1$ and $\mathbf{a}_2$, are given by the following [11]:

$$a_1 = \frac{a}{2}(3, \sqrt{3}) \tag{1.1}$$

$$a_2 = \frac{a}{2}(3, -\sqrt{3}) \tag{1.2}$$

a is the distance between carbon atoms, which is ≈ 1.42 Å. The reciprocal lattice vectors, $\mathbf{b}_1$ and $\mathbf{b}_2$, are given by the following [11]:

$$b_1 = \frac{2\pi}{3a}(1, \sqrt{3}) \tag{1.3}$$

$$b_2 = \frac{2\pi}{3a}(1, -\sqrt{3}) \tag{1.4}$$

The two points at the corner of the Brillouin zone, K and K', are called the Dirac points. The importance of these points will be clear later on. Their positions in momentum space are given by the following [11]:

$$K = (\frac{2\pi}{3a}, \frac{2\pi}{\sqrt{3}a}) \tag{1.5}$$

$$K' = (\frac{2\pi}{3a}, -\frac{2\pi}{\sqrt{3}a}) \tag{1.6}$$

For simplicity, the tight-binding model will be used considering only nearest neighbor carbon atoms. The nearest neighbor vectors in real space are given by the following [11]:

$$\delta_1 = \frac{a}{2}\left(1, \sqrt{3}\right) \tag{1.7}$$

$$\delta_2 = \frac{a}{2}\left(1, -\sqrt{3}\right) \tag{1.8}$$

$$\delta_3 = \frac{a}{2}(-2,0) \tag{1.9}$$

The tight-binding Hamiltonian, H, for electrons in graphene assuming they can only hop to its nearest neighbor is given by the following [11]:

$$H = -t\sum_{<i,j>,\sigma}(a_{\sigma,i}{}^{+}\, b_{\sigma,j} + H.C) \tag{1.10}$$

$a_{\sigma,i}$ ($a_{\sigma,i}{}^{+}$) annihilates (creates) an electron with spin σ, which σ = ↑ or ↓, and t is the nearest neighbor hoping energy (≈ 2.8 eV). Units were chosen so that ħ = 1. The energy bands derived from this Hamiltonian have the following form [11]:

$$E_{\pm}(k_x, k_y) = \pm t\sqrt{3 + 2\cos\left(\sqrt{3}k_y a\right) + 4\cos\left(\frac{\sqrt{3}}{2}k_y a\right)\cos(\frac{3}{2}k_x a)} \tag{1.11}$$

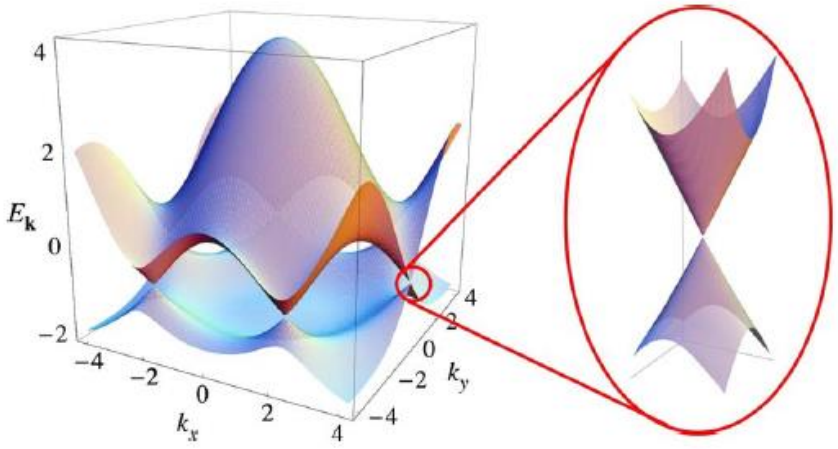

Fig. 1.4 Electronic energy dispersion in graphene with a close-up at the Dirac point circled in red. The energy dispersion forms cones near the Dirac points, called the Fermi-Dirac cones. Courtesy of Castro Neto et al. [1]

A plot of the electronic energy dispersion of graphene is shown in Fig. 1.4. The + sign in Eq. (1.11) represents the upper band, π*, and the – sign represents the lower band, π. Circled in Fig. 1.4 is a close-up of one of the Dirac points. The dispersion here can be obtained by expanding close to the K or K' vector in Eq. (1.11) with k = K + q where q << K. The dispersion is then given by the following [11]:

$$E_{\pm}(q) = \pm v_f|q| + O[\left(\frac{q}{K}\right)^2] \tag{1.12}$$

q is the momentum relative to the Dirac point and v_F is the Fermi velocity, which is about 10^6 m/s. [11]

First of all, it's important to note that graphene's band structure creates a direct band-gap semi-metal. Secondly, compared to the usual case ($E(q) = q^2/2m$), the Fermi velocity in Eq. (1.12) does not depend on the energy or momentum. In the usual case, the velocity changes

greatly with the energy. This means graphene's charge carriers behave as Dirac fermions, with a zero effective mass that allows for ballistic transport [11]. Furthermore, graphene has been shown to have carrier mobilities upwards of 15,000 cm^2/Vs at room temperature, with highest ever recorded mobility of over 200,000 cm^2/Vs under ideal conditions [1].

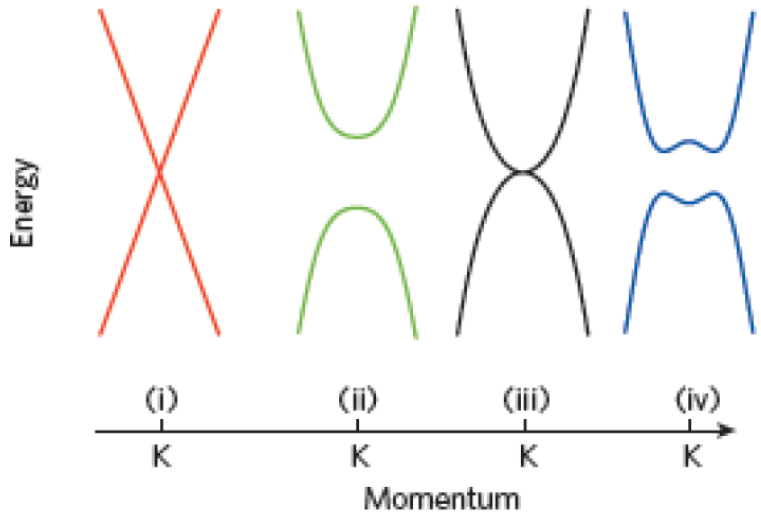

Fig. 1.5 Fermi-Dirac cone of graphene for the following cases: (i) pristine graphene, (ii) chemical or geometry-restrictive doping, (iii) bilayer graphene, and (iv) doped bilayer graphene. Courtesy of F Schweirz. [12]

For electronic applications, many researchers have done work in attempt to modify the band structure and dope graphene, as seen in Fig. 1.5. The Fermi-Dirac cone can be modified by having additional layers or from doping contaminants (typically metal or polymer in contact with the surface of graphene) [13]. Graphene with doping levels upwards of 10^{13} cm^{-2} have been reported [14]. Furthermore, doping contaminants shift the Fermi level up or down and cause rounding of the energy bands, resulting in a decrease in the charge carrier mobility [12].

1.3 Mechanical properties of graphene

Along with its electronic properties, graphene has also been touted as a wonder material for its mechanical strength. With graphene and other 2D materials, mechanical properties play an important role in manufacturing, integration with other materials, and performance in potential applications. Moreover, as a 2D material, graphene has extremely high in-plane stiffness and strength but very low flexural rigidity [15].

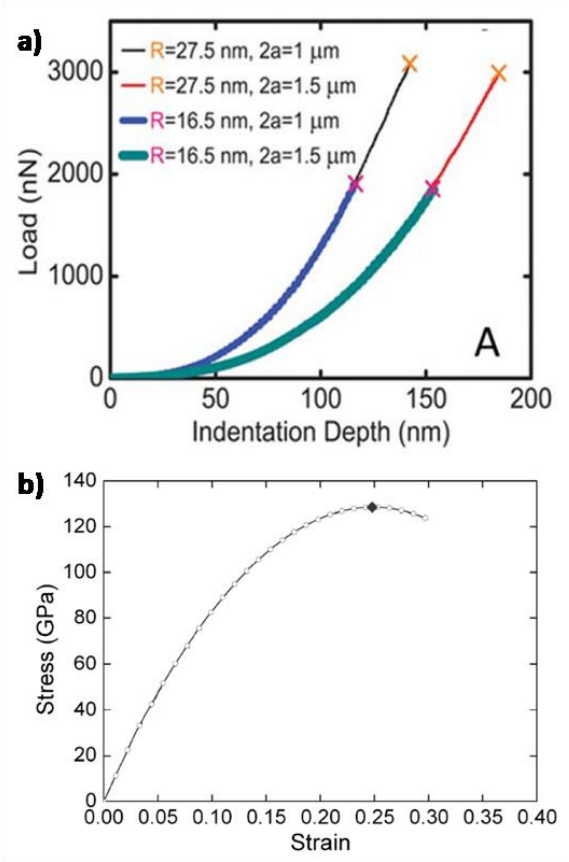

Fig. 1.6 a) Force-displacement data from AFM nano-indentaiton of suspended monolayer graphene, with different tip radii and specimen diameters. Fracture loads are indicated by × marks. b) Stress-strain curve put together by Gary Paradee using nano-indentation measurements conducted by Lee et al. Courtesy of Lee et al. [16]

Lee et al. were the first to directly measure the mechanical properties of graphene. They synthesized pristine monolayer graphene flakes through mechanical exfoliation, suspended them, and then measured the material's mechanical properties via nano-indentation using an atomic force microscope (AFM). Through analysis of the indentation force-displacement behavior shown in Fig. 1.6a, they extracted a 2D Young's modulus of 340 N/m, 3D Young's modulus of about 1 TPa (assuming a thickness of 0.34 nm), an intrinsic strength of 130 GPa, and a strain limit of about 25%—establishing graphene as the strongest material ever measured. A stress-strain curve was put together using the information above by Gary Paradee and is shown in Figure 1.6b, summarizing pristine graphene's mechanical properties. [16]

Graphene's experimentally measured mechanical properties are in good agreement with first principles based simulations such as DFT and molecular dynamics [17-18]. It turns out graphene's high in-plane stiffness is due to the strong σ-bonding between carbon atoms in its hexagonal lattice [16]. In addition, being atomically thin makes graphene highly flexible, with flexural deformation commonly observed in the form of wrinkling or folding [15]. Furthermore, Paradee et al. has paid special attention to graphene's fatigue characteristics, experimentally measuring an extremely high endurance limit of ~ 40 GPa [19]. This combination of mechanical strength, flexibility, and reliability make graphene an ideal material for micro and nano-electromechanical systems (M/NEMS) applications, which will be elaborated later.

1.4 Effects of polycrystallinity on the electronic and mechanical properties of graphene

Geim and Novoselov used mechanical exfoliation to first synthesize graphene in 2004. Although pristine graphene can be achieved using this method, the graphene flakes it renders are on the order of microns, which is impractically small [6]. Currently, the most popular way to

synthesize large-area high quality films of graphene is via chemical vapor deposition (CVD) on copper foils [20]. This is the method we used to synthesize graphene, and it will be elaborated later. Many believe this method has the most potential for large-scale industrial adoption. Unfortunately, this method also has drawbacks. The films produced using CVD are typically polycrystalline, in that the film is composed of a collection of single crystalline grains of graphene stitched together at the grain boundaries (GBs) [21]. In general, GBs are detrimental to charge transport in semiconductor materials and the semiconductor industry generally favors high-quality single crystalline materials. Furthermore, it's intuitive to think that GBs will greatly alter graphene's mechanical properties, such as the elasticity and fracture strength, because of weaker carbon-carbon bonding at those locations. It is clear to see that the effects of polycrystallinity are important and is investigated in this section. [20]

In polycrystalline graphene, charge transport is limited by two factors: charge scattering due to the GBs and charge scattering within the grains. It turns out that the two sources of resistance can be captured by the following equation [22]:

$$R_s = {R_s}^0 + \frac{\rho_{GB}}{l_G} \tag{1.13}$$

R_s is the sheet resistance of a polycrystalline sample, ${R_s}^0$ is the sheet resistance for single crystalline graphene, ρ_{GB} is the average GB resistivity, and l_G is the average grain size in the sample. For samples with large grains, ${R_s}^0$ will dominate and R_s is independent of the grain size. For samples with small grains, R_s will be dominated by ρ_{GB} and will scale inversely with the grain size. [22]

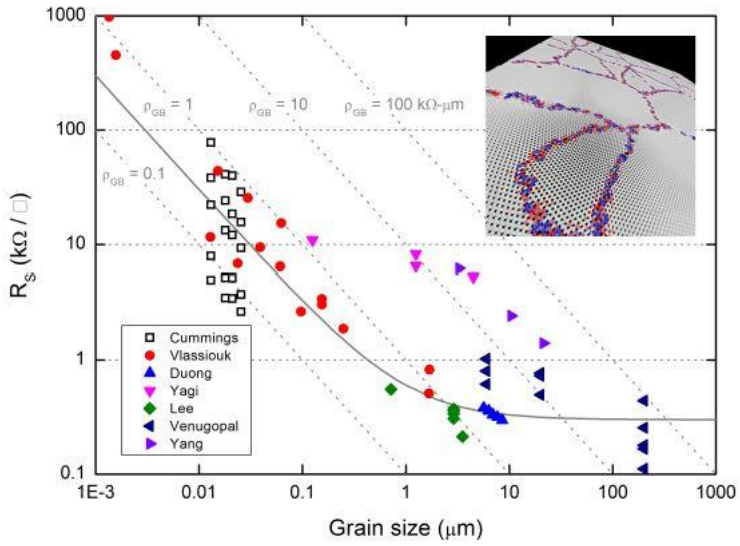

Fig. 1.7 A summary of the sheet resistance as a function of the average grain size in polycrystalline graphene samples [22]. The solid symbols are experimental measurements [23-27], and the open squares are numerical calculations from [24]. The grey solid line shows the behavior of the ohmic scaling law from equation 13, assuming R_s^0 = 300 Ω/μm and ρ_{GB} = 0.3 kΩ-um. Courtesy of Isacsson et al.

To show how R_s scales, a summary of measured R_s values of polycrystalline graphene was put together by Isacsson et al. and plotted in Fig. 1.7 [22]. Using this figure, it is clear how global electronic properties scale with the average grain size in polycrystalline graphene samples and that minimizing the impact of GBs is important for electronic applications. Today, it is possible to grow graphene with grain sizes on the order of cms [28]; however, there is a significant trade-off between the grain size and the complexity, growth time, costs, etc. in CVD growth. In industrial applications, it's important to fully understand what the global electronic properties are needed so that growth conditions can be optimized for it.

In addition, research with a more global view on polycrystalline graphene suggests that GBs play an important role in the material's mechanical properties and that these properties strongly depend on the grain size, l_G, and the system size, L. Theoretical and experimental studies showed that if l_G is similar to L, then the polycrystalline sample's mechanical properties will be very similar to single crystalline graphene's (~ 1 TPa) [29-32]. However, in theoretical MD simulations and experimental nano-indentation studies where $L >> l_G$, it was shown that polycrystalline graphene had a significantly lower 3D Young's modulus, 600 GPa and 150 GPa respectively [33-34]. The decrease in elasticity was attributed to out-of-plane buckling due to the GBs. [22]

The fracture strength of polycrystalline graphene was also studied, which is naturally expected to diminish with the presence of GBs. However, MD simulations showed that in certain configurations, GBs can be just as strong as carbon-carbon bonding [29]. Experimental studies found polycrystalline fracture strengths (ranging from ~ 35 to 110 GPa) to be diminished but on the order of single crystalline fracture strengths (~130 GPa) [21], [32], [34]. Like for electronic properties, this information is useful because it's important to understand what mechanical properties are needed so that growth conditions can be optimized for it.

1.5 Graphene synthesis methods

Since it was first experimentally produced in 2004, the scientific community has been hard at work in hopes to create a scalable synthesis method for large-area graphene films. In this section, the four most popular synthesis methods are surveyed: mechanical exfoliation, liquid phase exfoliation, SiC thermal decomposition, and chemical vapor deposition (CVD).

The simplest method is mechanical exfoliation. This method was first reported by Geim and Novoselov in 2004 and still happens to be the method that produces that highest quality graphene. This method involves peeling highly order pyrolytic graphite (HOPG) using adhesive tape. Because the graphene layers are weakly bonded via van der Waals bonding in graphite, it's possible to mechanically cleave graphene by repeatedly peeling graphite using tape. However, this method results in randomly distributed monolayer and few layer graphene flakes that are typically on the order of microns. For these reasons, this method is typically used in laboratory experiments, and it is not practical to use this method for large-scale production of graphene. [6]

Another common graphene synthesis method is liquid phase exfoliation, first reported by Hernandez et al. Here, graphene is exfoliated from graphite using a solvent (typically acetic acid, sulfuric acid, or hydrogen peroxide) and ultrasonication. This method can quickly and easily produce graphene samples; however, the method yields randomly distributed graphene nano-ribbons (width < 10 nm). Therefore, like mechanical exfoliation, this method is not feasible for the scalable production of large-area graphene films. [35]

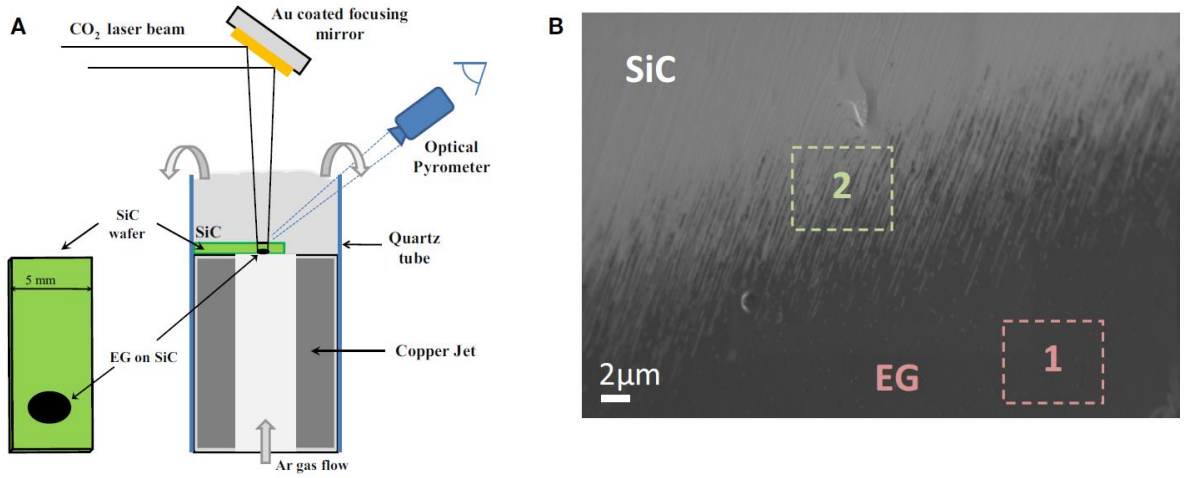

Fig. 1.8 a) Schematic showing how thermal decomposition on SiC is achieved using a CO_2 laser. b) SEM image showing the formation of epitaxial graphene (zone 1) on 6H-SiC (0001) (zone 2). Courtesy of Yannopolous et al. [36]

In 2012, Yannopolous et al. reported a drastically different graphene synthesis method: thermal decomposition from a 6H-SiC (0001) surface. A schematic of this method is shown in Fig. 1.8a. Effectively, the only step in this method is to heat the SiC surface using a CO_2 laser, causing decomposition of SiC to graphene at the heated areas. Fig. 1.8b shows an SEM image of graphene formation on the SiC surface. This method does not require high-vacuum, can be operated at low temperatures, and happens at time scales on the order of seconds. Furthermore, the stacking order of epitaxial graphene can be controlled, and the laser beam can be used to draw out graphene patterns on the SiC substrate. [36]

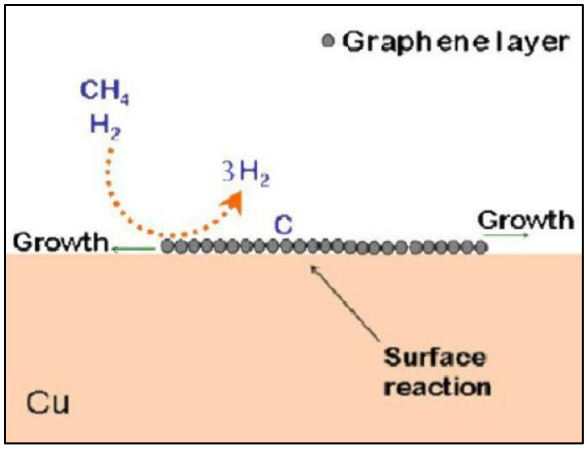

Fig. 1.9 Illustration showing chemical vapor deposition of graphene on Cu foil. Courtesy of Y. Zhang et al. [20]

However, despite the advantages the thermal decomposition method has, it is still relatively expensive and time consuming for large-scale graphene growth compared to the most prominent graphene synthesis method today: chemical vapor deposition (CVD) on Cu. Here, a Cu foil is first placed into a CVD furnace and pumped down. Then, hydrogen gas is flowed through the chamber while the furnace is heated to over 1000 °C. Hydrogen has many purposes. First, it eliminates any native oxides. For example, CuO and Cu_2O on the Cu foil surface will be reduced. Secondly, hydrogen acts a protection layer, preventing the metal from oxidizing at high temperatures. Lastly, hydrogen also acts as an activator of surface-bound carbon when the carbon source is introduced into the chamber, which occurs in the next growth step. A hydrocarbon gas (typically methane) is then introduced into the furnace, providing the carbon species for growth. Transition metals enable low-energy pathways for forming intermediate compounds needed for graphene growth. Carbon decomposes from methane and goes to the Cu

surface, and then nucleation and growth occurs. Carbon on the surface does not diffuse into the bulk because Cu has very low carbon solubility and instead diffuses along the Cu surface. After some time, a monolayer of graphene fully covers the surface. A second layer does not form on top of the first because it is not thermodynamically stable at such high growth temperatures. Lastly, the methane flow is stopped and the furnace is cooled back down to room temperature while hydrogen is left flowing for protection. In this way, good monolayer graphene growth is achieved. [20]

CVD on Cu foils was chosen for our experiments because it is relatively low cost, offers good monolayer growth control, and produces complete large-area high quality films. Typically, labs are able to grow graphene films on the order of cm^2 [20]. In our lab, we were able to produce graphene films on the order of hundreds on cm^2. However, this method also has drawbacks. Unlike mechanical and liquid phase exfoliation, CVD results in polycrystalline graphene, with grain sizes that are dependent on the growth conditions [21]. Furthermore, in order to use the CVD graphene grown on Cu, it must be transferred onto a target substrate; unfortunately, most transfer methods involve introduction of contamination, which ultimately affects graphene's electronic and mechanical properties and the device graphene is used to make [37], [38]. These issues are addressed in chapter 4 of the dissertation.

1.6 Graphene transfer methods

As mentioned in the previous section, some synthesis methods, such as CVD method we use, require graphene to be transferred from the growth substrate onto the target substrate. This section provides a review of the most popular transfer methods and concludes with the one we used for our experiments.

As in the growth section, the simplest transfer method is mechanical exfoliation. Here, HOPG is repeatedly cleaved using tape adhesive tape on the target substrate. Because graphene layers in graphite are weakly bonded by van der Waals bonding, it is possible to mechanically cleave single and few layer graphene. In this way, graphene is transferred onto the target substrate. However, as stated in the section 1.5, this method results in randomly distributed micron-sized graphene flakes; therefore, it is not ideal for transferring large-area graphene. [6]

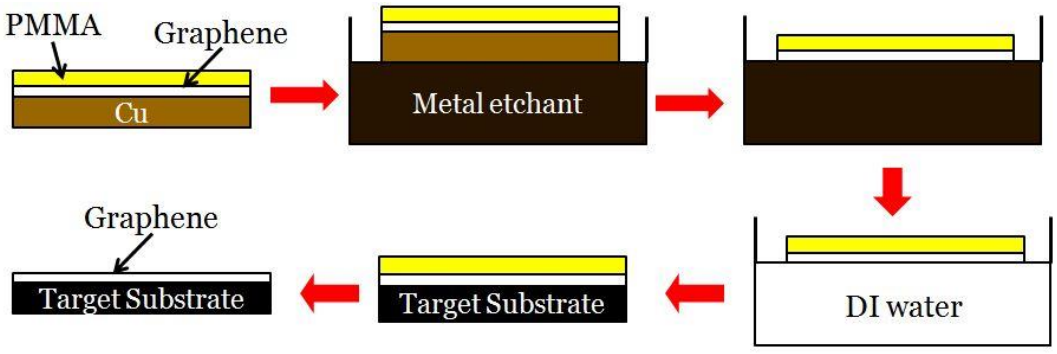

Fig. 1.10 Polymer assisted wet transfer of graphene. PMMA is used as the polymer support as an example. [37]

Instead, most of the graphene today is transferred using polymer assisted wet transfer, as outline in Fig. 1.10. First, graphene is typically grown via CVD on Cu foil [20], as described in section 1.5. Then, a polymer is placed on top of the graphene/Cu. Its purpose is to protect graphene as it is moved around during the transfer process. Polymer/graphene/Cu is then placed on top of metal etchant and left to float. After some time, the Cu is etched away, leaving only polymer/graphene. The sample is then scooped and transferred onto a beaker of DI water using a Si wafer. This is done several times to wash away any residual metal and residual etchant. Then,

polymer/graphene is scooped onto the target substrate and left to dry. This ensures graphene adheres well to the substrate. After drying, the polymer support is removed, typically with a solvent like acetone or chloroform, leaving only graphene on the target substrate. [37]

One of the first polymers employed for graphene transfer was PDMS (polydimethysiloxane). PDMS was chosen because it is durable, resistant to many solvents, and has a low surface free energy. First, PDMS is brought into contact with the graphene/Cu, acting as a mechanical support as Cu is etched. After the washing step, PDMS/graphene is brought into contact with the target substrate. Because PDMS has a low surface free energy, it maintains a low adhesion force with graphene. Therefore, when PDMS/graphene comes into contact with the target substrate, graphene prefers to adhere to the substrate instead of PDMS. In this way, graphene is freed from PDMS and left on the target substrate. [39]

Despite PDMS's advantages, PMMA (poly(methy methacrylate)) is the polymer of choice in polymer assisted wet transfer of graphene today. PMMA first demonstrated its usefulness in 2008 when it was used to transfer carbon nanotube films [40]. Unlike PDMS which forms weak van der Waals bonds with graphene, PMMA forms covalent bonds with the nano-material, providing better support as it gets moved around during the transfer process. Furthermore, PMMA can be easily spin-coated onto large-area graphene/Cu films, allowing the potential for scalable graphene transfer. However, this method also has drawbacks, the biggest one being that it is hard to completely remove PMMA. To make matters worse, PMMA residue tends to have a p-doping effect on graphene, which also results in increased charge scattering and lowered mobility [13]. Furthermore, because PMMA residue is typically on the order of nanometers whereas graphene's thickness is 0.34 nm, PMMA can significantly change the

mechanical response of suspended graphene [1]. Unfortunately, semiconductor manufacturing processes typically used to remove polymer residue such as oxygen plasma etching are too abrasive to graphene. Over the years, amendments have been made to improve the PMMA assisted transfer process, such as the use of thermal annealing and stronger solvents [41-42]; however, PMMA residue is still an significant issue in graphene research and its relevance to my research will be addressed in chapter 4 of this dissertation.

The transfer method can also be done without a polymer support, as Bae et al. reported in 2010. Although this avoids potential polymer contamination, it turns out that graphene is too prone to tearing and ripping during the etching and scooping process, breaking apart even with the slightest disturbance. For these reasons, many researchers, including myself and Bae et al., prefer using a polymer support to ensure safe transfer. [43]

In addition to the methods already mentioned, Caldwell et al. reported a new transfer method using thermal release tape in 2010. Here, the group applied thermal release tape using a steel pressure plate on epitaxially grown graphene on SiC; this same method is also applicable to CVD graphene on Cu. By the force of the adhesive, graphene is pulled from the growth substrate and then placed onto the target substrate. Afterwards, simply applying heat removes the tape, leaving graphene on the target substrate. [44]

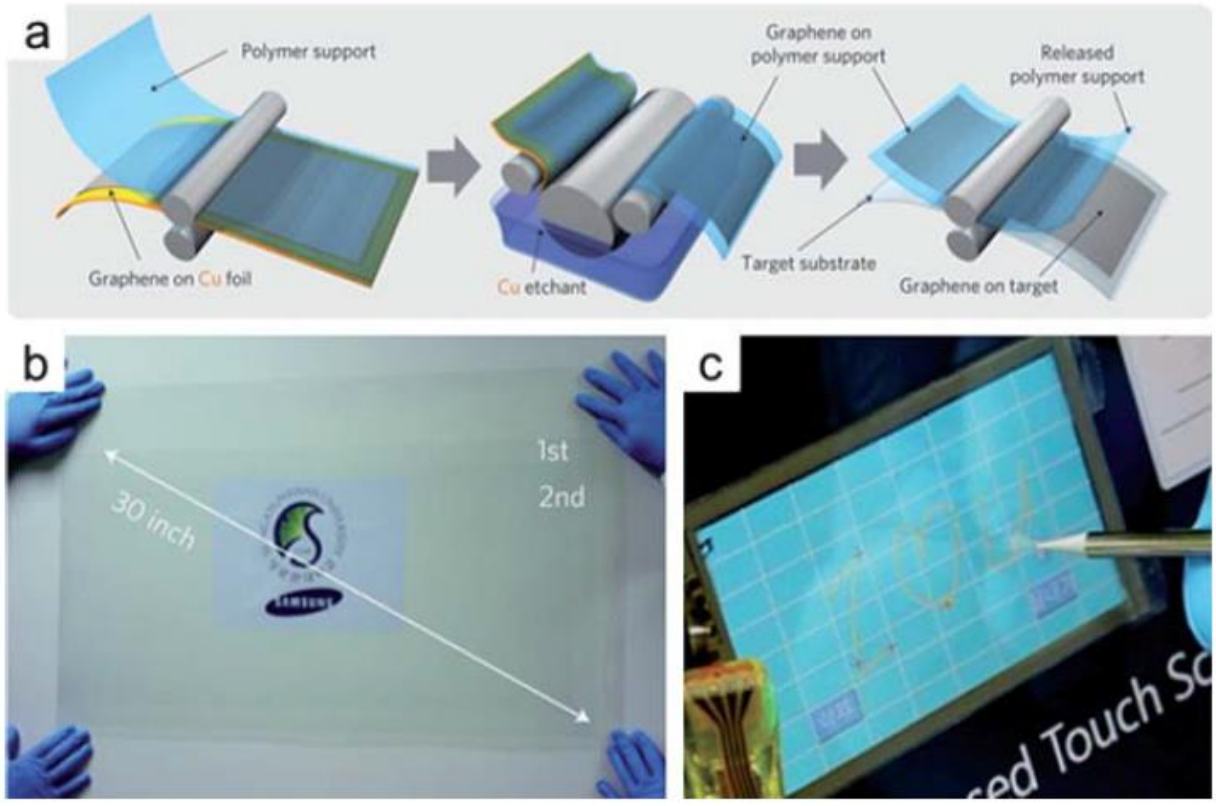

Fig. 1.11 Roll-to-roll production of large-scale, continuous graphene film on flexible substrate. (a) Schematics of the roll-to-roll graphene transfer. The process includes attachment of a polymer support on graphene/Cu foil, copper etching, and dry-transfer-printing on a target substrate. (b) 30 in diagonal graphene sheet on a PET substrate. (c) Photograph touch screen panel using roll-to-roll graphene. Courtesy of Bae et al. [45]

Furthermore, this method can be modified to include a roll-to-roll process, as outlined in Fig. 1.11a. This highlights the merit of using thermal release tape because it allows for scalable continuous large area graphene transfer. The roll-to-roll process is typically used in the paper and metal rolling industries where heat and pressure are applied to paper or metal in between two spinning roller pins. Bae et al. also reported using this to attach thermal release tape to a 30 in

diagonal piece of graphene on Cu foil grown inside an 8 in diameter furnace (Fig. 1.11b). Next, Cu is removed using a metal etchant then transferred to a flexible PET (polyethylene terephthalate) substrate. Lastly, the thermal tape is released by being moved between the two roller pins again at a low temperature of 120 °C. Fig. 1.11c shows Bae et al.'s success in applying roll-to-roll graphene on PET and using that as a touch screen panel. [45]

Despite the advantages the roll-to-roll process has, it can also lead to cracks and holes in graphene if the substrate is too rigid or if too much pressure is applied during rolling. Furthermore, like polymer assisted wet transfer, this process can leave behind polymer contamination on graphene and unintentionally affect the nano-material's physical properties. To circumvent the issues that cause cracks and holes, Kang et al. suggested using a hot press method instead of rollers [46]. Here, hot presses apply pressure on the tape/graphene/substrate from the top and bottom, eliminating shear stress from the roll-to-roll process. However, this method still does not address the polymer contamination issue and needs further development.

Considering all the popular transfer methods available, we chose to use PMMA assisted wet transfer using PMMA because it is compatible with CVD graphene, allows us to easily transfer wafer scale films, and is relatively low cost. However, as mentioned earlier, polymer contamination left behind affects graphene's electronic and mechanical properties, an issue addressed in chapter 4.

1.7 Raman spectroscopy of graphene

Raman spectroscopy has become a very commonly used characterization tool in the graphene research community because it's easy to use, non-destructive, and electronic and structural material properties can be extracted from it. Because I and other members of my group extensively used it during my PhD, I will devote this section of my dissertation to go over the basics of Raman spectroscopy and then delve into how it is specifically applied to graphene. [47], [48]

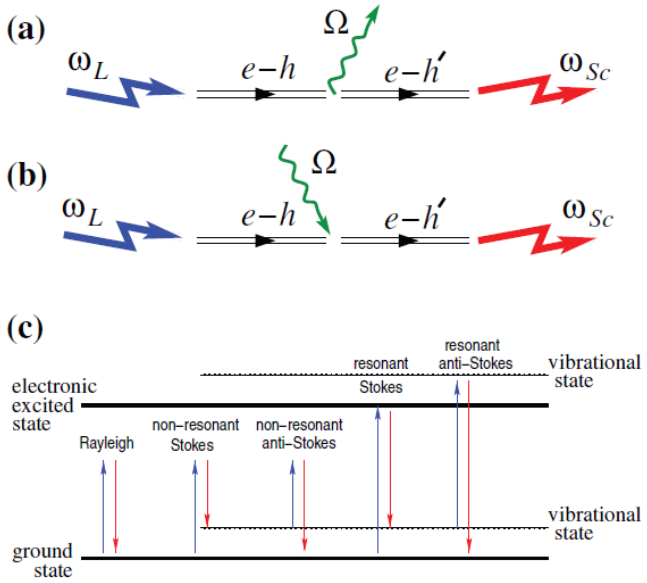

Fig. 1.12 Illustration of Raman scattering. a) Stokes process. b) Anti-Stokes process. c) Rayleigh and Raman scattering under resonant and non-resonant conditions. Courtesy of A Ferrari et al. [47]

First of all, the scattering of light by a material can be generalized into two broad categories: elastic and inelastic scattering. Elastic, or Rayleigh, scattering takes place when the

system returns to its initial state after the scattering event. That is, the incident photon, with energy $\hbar\omega_L$, and the emitted photon have the same energy (or frequency). When light is shined on a material, most of the scattering is elastic. On the other hand, inelastic, or Raman, scattering takes place when the incident photon and the emitted photon have different energies and occurs at a much lower probability than elastic scattering. As seen in Fig. 1.12a, the incident photon can excite an electron-hole pair e-h, and then the e-h can decay into a phonon Ω and another electron-hole pair e-h'. e-h' subsequently recombines and emits a photon with energy $\hbar\omega_{Sc}$, in which $\hbar\omega_{Sc} < \hbar\omega_L$. This scattering process is known as the Stokes process.

Un-intuitively, the emitted photon can also have a greater energy than the incident photon ($\hbar\omega_{Sc} > \hbar\omega_L$) after the scattering event, as seen in Fig. 1.12b. Here, a phonon Ω is absorbed by the electron-hole pair (e-h), resulting in another electro-hole pair e-h'. e-h' subsequently decays to the ground state, emitting a photon with energy $\hbar\omega_{Sc}$ in the process. This process is known as the anti-Stokes process. [47]

The Stokes process is much more probable than the anti-Stokes process because the Stokes process begins by exciting an electron-hole pair from the ground state. Therefore, the vast majority of Raman spectra in the literature are Stokes measurements. On a Raman spectrum, the intensity of scattered light is plotted against the "Raman shift", the difference between the incident and scattered photon energy. For historical reasons, the Raman shift is plotted in units of energy cm^{-1}, in which 1 meV = 8.0655447 cm^{-1}. In addition, most of the Raman spectra in the literature are non-resonant processes, in which the photon energy $\hbar\omega_L$ does not excite an electron to a stationary electronic state. If the excitation is excited to match a specific level, as seen in Fig. 1.12c, then the process is resonant and the intensities are strongly enhanced. [47]

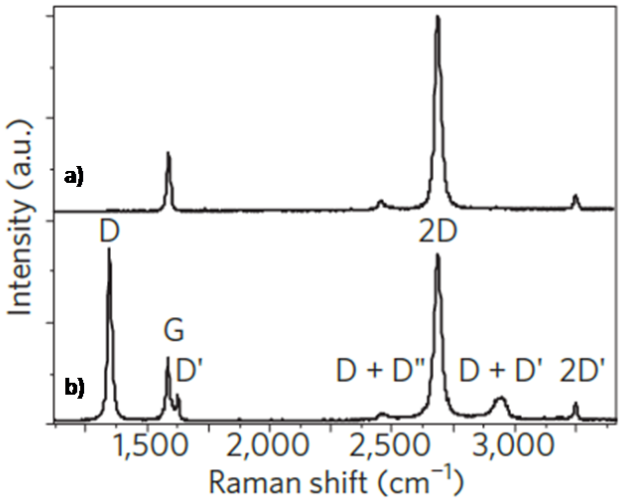

Fig. 1.13 Typical Raman spectra of (a) pristine graphene and (b) defected graphene. Courtesy of A Ferrari et al. [47]

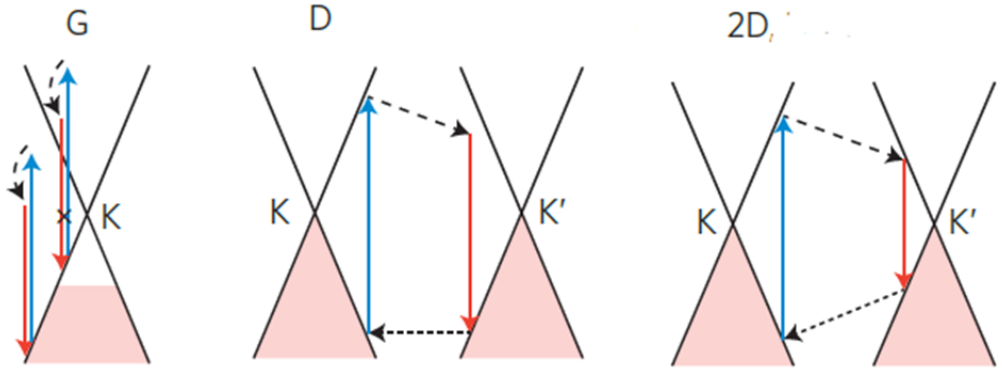

Fig. 1.14 Schematic illustrating how G, D, and 2D peaks arise in graphene with electronic energy bands. Electron dispersion (solid black lines), occupied states (shaded areas), inter-band transitions neglecting the photon momentum, accompanied by photon absorption (blue arrows) and emission (red arrows), intra-band transitions accompanied by phonon emission (dashed arrows), and electron scattering on a defect (horizontal dotted arrows). Courtesy of A Ferrari et al. [47]

The photon-phonon interaction involved in Raman spectroscopy allows users to extract useful information from graphene. Fig. 1.13 shows typical Raman spectra of pristine and defected graphene labeled with graphene's main characteristic peaks: the G, D, and 2D peaks. The G peak arises from carbon-carbon bond stretching between atoms in graphene and is present in all graphitic materials. For the D peak to occur, a charge carrier must be excited and in-elastically scattered by a phonon and then elastically scattered by a defect or zone boundary, resulting in recombination. Therefore, D peak arises from disorder in graphene's crystal structure and its intensity can be used to measure the material's defect density. On the other hand, the 2D peak occurs when a charge carrier is excited and in-elastically scattered twice. Fig. 1.14 shows schematics illustrating examples of how the G, D, and 2D peaks arise. [47]

1.8 Importance of my research

After introducing the basics of graphene, it's appropriate to discuss the contributions of my research before going into the research details. First, the NSF grant that provided funding for my research was to explore how suspended graphene can be used for electrostatic discharge (ESD) protection. Wei Zhang, a former PhD student in our group, was the person who spearheaded this project. I helped Wei on the project until he graduated and then took over. Early on, we fabricated suspended graphene ribbon devices and were able to show that their electromechanical responses can be used to shuttle charge via the MEMS pull-in phenomenon, thereby offering ESD protection as a mechanical switch that actuated after sensing the excess stray charge from an ESD event. Furthermore, we showed that ESD protection parameters can be tuned with the device geometry, offering a new and unique way of providing protection.

After this, I decided to explore different avenues of research to improve the device performance. First, nail structures were explored to pin down the ribbon during pull-in, improving the device reliability. Secondly, compliant mechanism ribbon designs were explored with the help of the Flexible Research Group from UCLA's Mechanical and Aerospace Engineering Department. Third, the effects of polymer residue on the electromechanical responses of suspended graphene were also explored. Finally, we looked beyond just using the device as a mechanical switch and theoretically explored its potential as a high frequency resonator. Through these different projects, we not only achieved our initial goal of showing suspended graphene can be used for ESD protection but also contributed to the body of graphene and M/NEMS research in the literature and broadened the possibility of using M/NEMS devices by enlisting graphene.

Chapter 2: Suspended graphene ribbons for ESD applications

2.1 Introduction to ESD

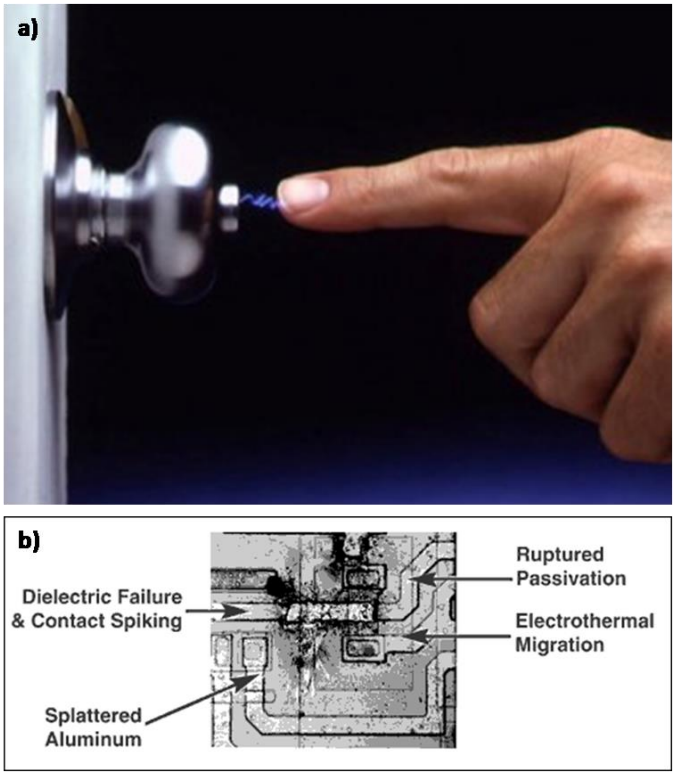

Fig. 2.1 Electrostatic discharge. a) Illustration of touching a door knob and getting shocked, a commonly experienced ESD event [49]. b) An unprotected semiconductor IC (RS-232 receiver) that experienced a 15kV ESD event [50]. Courtesy of gokimo.com and maximintegrated.com respectively.

This chapter elaborates on the first project I undertook during my PhD: using suspended graphene ribbons for electrostatic discharge (ESD) applications. To begin, this section provides a brief history of ESD research and a review of commonly used ESD protection devices today, giving context to the project.

In essence, ESD occurs when two objects with an electric potential difference experience charge transfer. There is a lot of history behind ESD research. For example, in the 15th century, it was reported that European military agencies developed ways to protect against ESD to handle munitions safely. In the 18th century, Benjamin Franklin made major contributions with the invention of the lightning rod, arguably the most significant ESD protection device in history. Today, ESD remains a common phenomenon that most of us experience in everyday life. For example, as seen in Fig. 2.1a, an ESD event occurs when you get shocked after walking on a carpet and touching a door knob. Unbeknownst to you, you were collecting charge while shuffling around, and touching a door knob gives a pathway for that charge to flow. [51]

ESD events, as well as protection from them, are also important in engineering today, especially when designing semiconductor integrated circuits (ICs). ESD became an escalating problem in the 1970s as ICs began to become more and more complex and sensitive. According to the National Semiconductor Corporation, today, over 30% of all IC failures are due to ESD [52]. Generally, there are two ways ESD events lead to failure: 1) high currents are generated leading to irreversible thermal damage in the semiconductor material and/or metal interconnects and 2) high electric fields generated rupture dielectric thin films. Figure 2.1b is a photo of an unprotected RS-232 receiver that experienced a 15kV ESD event, showing the damage that ESD can actually do [50]. In general, engineers are looking to provide protection against pulses as fast as 150 ns, currents on the order of tens of Amperes, and voltages on the order of kVs. [51]

2.2 Traditional ESD protection devices

Over the years, engineers have come up with many ways to provide ESD protection. The basic function of any ESD device is to turn on when it senses a surge of charge then provide a low impedance path for discharge. The more advanced devices can clamp the voltage at a lower level, allowing safer discharge. Many different semiconductor devices can be used to do this; however, for brevity, only the two most popular ESD protection devices will be discussed here: reversed biased Zener diodes and ground gate NMOSFETs. Their I-V curves are shown in Fig. 2.2 [51]

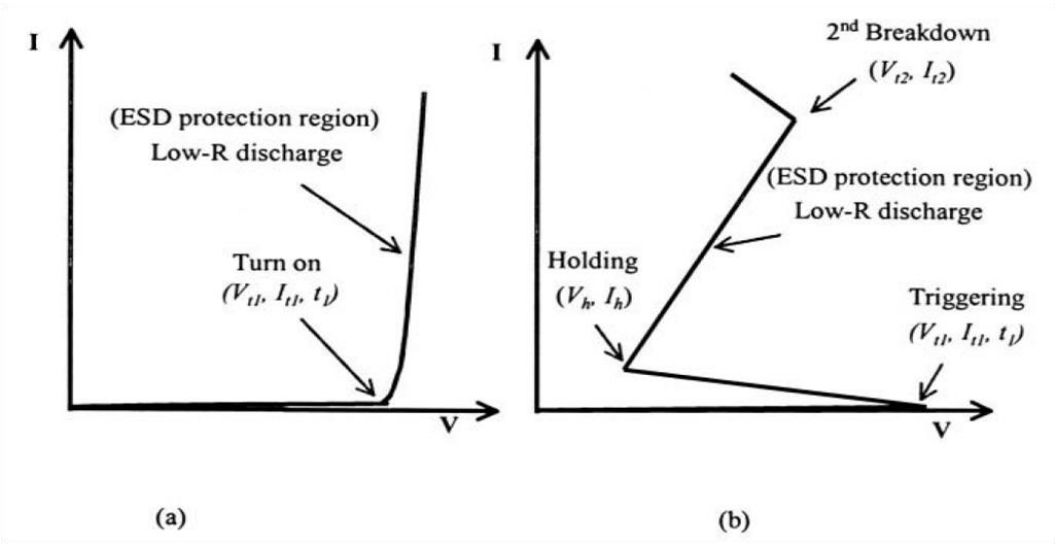

Fig. 2.2 I-V curves for commonly used ESD protection devices: a) reversed biased Zener diodes and b) ggNMOSFETs. Courtesy of A. Wang. [51]

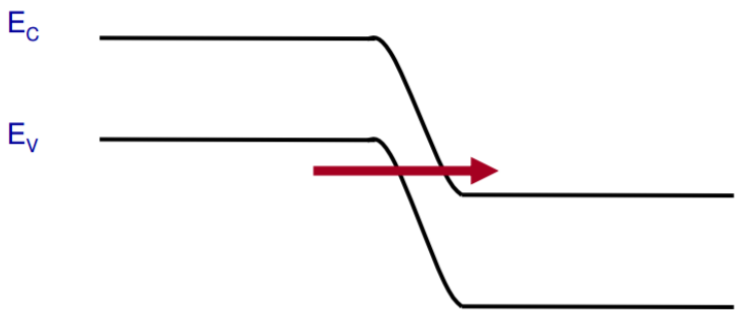

Fig. 2.3 Band diagram illustrating the Zener effect. Courtesy of O. Acosta. [53]

Diodes are the “dinosaurs” of ESD protection devices; however, they are still widely used in the industry because they are simple and efficient [51]. As engineers, we know that a simple solution is best, given that it provides adequate protection. Although forward biased diodes can be used, the most commonly used diodes used are actually reversed biased Zener diodes. Here, the depletion region is made small by heavily doping the p- and n- sides. At sufficiently high reversed bias, the electric field causes electrons from the valence band on the p-side to tunnel through the junction to the conduction band on the n-side, causing a sharp increase in the reverse current, as seen in Fig. 2.3 [53]. This phenomenon is known as Zener breakdown, and the voltage at which this breakdown occurs is the trigger voltage of the ESD protection device, V_{t1}. Zener diodes are designed such that Zener breakdown occurs before avalanche breakdown. In this way, reversed-bias Zener diodes are made to turn on when there is a sudden surge of charge and allow a low impedance path for discharge, providing ESD protection. [51]

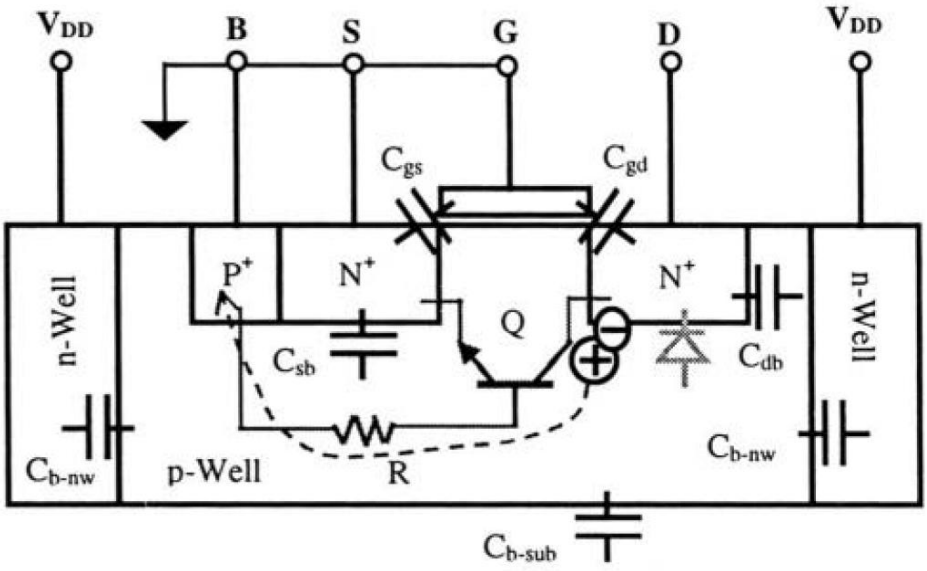

Fig. 2.4 Cross-sectional device diagram of a ggNMOSFET used for ESD protection. Courtesy of A. Wang. [51]

Despite the widespread use of diodes in ESD protection, it turns out that MOSFETs, specifically ground gate NMOSFETs (ggNMOSFETs), are the most commonly used ESD protection device due to its ability to achieve snapback and its compatibility with CMOS technologies. Fig. 2.4 shows a diagram of how the device is used for ESD protection. Here, the drain (D) is connected to the I/O pad, which is vulnerable to ESD events; on the other hand, the gate (G), source (S), and base (B) are all shorted together to ground. When a positive ESD event appears at the I/O pad, or D in this case, with respect to ground, the BD p-n junction is reversed biased all the way to avalanche breakdown. As a result, electron-hole pairs are created, generating a hole current which flows to ground though B. This builds up a potential, V_R, across the parasitic capacitance R. This V_R positively biases the BS p-n junction, eventually turning on the DBS n-p-n transistor. In this way, the device enters the snapback regime, clamping the

voltage at a lower level and allowing for safer discharge. If a negative ESD pulse appears at D, then the BD p-n junction will be forward biased and will provide a path for discharge. [51]

Other than Zener diodes and ggNMOSFETs, some other commonly used ESD protection devices are bipolar junction transistors and silicon controlled rectifiers. These single device structures have been dominant in providing ESD protection until the 1990s. However, as ICs became unbearably complex, single device structures evolved into ESD protection circuits. Today, customized protection circuits are made using the aforementioned components, with different circuits employed within the same chip sometimes. Unfortunately, because of the convoluted interaction of breakdown mechanisms involved among devices, it is hard to accurately simulate a practical ESD protection circuit. The circuit design is becoming so complex that engineers are currently resorting to a lengthy trial-and-error process to fulfill protection requirements. The engineer lays out the protection circuit and then tweaks a parameter, simulates, and hopes for the best, heavily relying on intuition and luck. These steps are re-iterated until the protection requirements are fulfilled. Then, their design is physically made in a semiconductor fabrication plant, with the hope that their circuit physically behaves in the way their simulation predicted. [51]

These barriers that ESD protection engineers were running up against prompted researchers to look for something new. In the following sections, I review how we showed that suspended graphene ribbons can be used to provide ESD protection. Furthermore, we show that the ESD protection parameters can be easily tuned by changing the device geometry, offering a novel and unique way of providing protection. [54], [55]

2.3 Introduction to suspended graphene ribbon device and the MEMS pull-in phenomenon

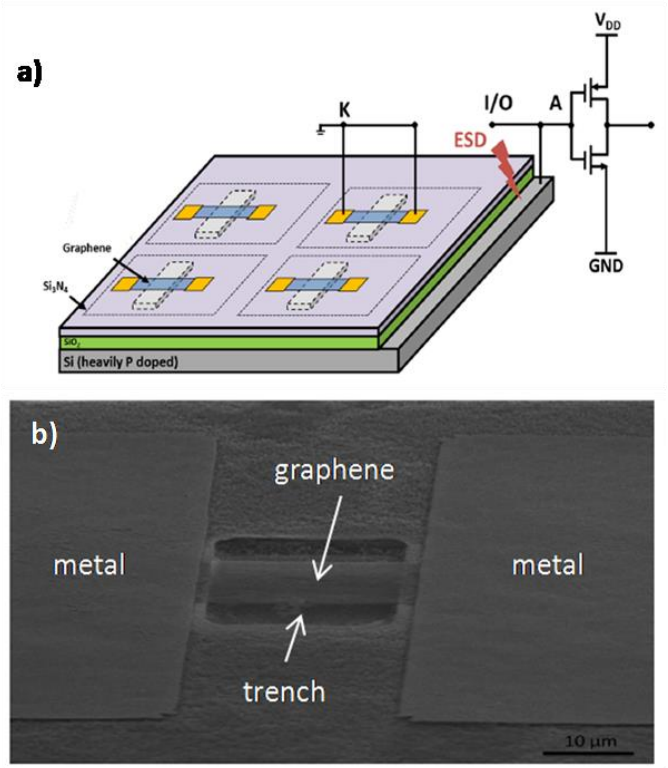

Fig. 2.5 Suspended graphene ribbon device. a) Schematic of the device and how it is connected for on-chip ESD protection [56]. b) Top-view SEM image of the device [57].

As mentioned in the previous section, this project focused on how to use suspended graphene ribbon devices for ESD applications, and this section serves as an introduction to the device in question. Fig. 2.5a shows a schematic of the device and how it is connected for on-chip ESD protection [56]. The two terminals of the device are the suspended graphene ribbon and the conducting p++ Si floor beneath it. The device is connected to the I/O pads or anywhere that is vulnerable to an ESD event. Fig. 2.5b shows a top-view SEM image of the as-fabricated device [57].

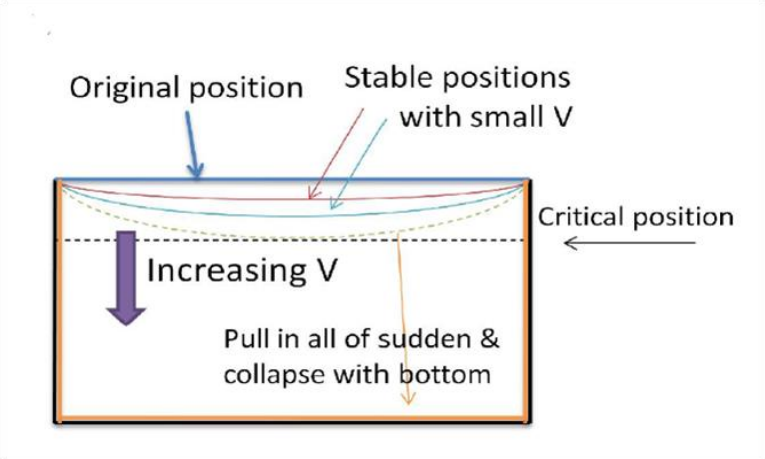

Fig. 2.6 Illustration of the MEMS pull-in phenomenon, the physical mechanism that provides ESD protection. Courtesy of Wei Zhang. [58]

The way the device provides ESD protection is with the MEMS pull-in phenomenon [59], illustrated in Fig. 2.6 [58]. When the ribbon is in the suspended position, the device is in the OFF state. When a voltage is applied across the top and bottom terminal of the device, an electrostatic force pulls the graphene ribbon down towards the floor. However, a mechanical restoring force is induced from the ribbon bending and acts in the opposite direction of the electrostatic force. At small voltages, the mechanical force can balance the electrostatic force, resulting in small and stable ribbon displacements. However, if we apply a sufficiently high voltage, the electrostatic force takes over, and the graphene ribbon pulls in and collapses to the floor. This is exactly what happens when there is a surge of charge, like an ESD event. At this point, the device is in the ON state. When the graphene makes contact with floor, there is a low impedance path for the charge to flow and the charge is dissipated through the floor. After discharge, the electrostatic force is released and, ideally, the mechanical restoring force props the ribbon back into its original suspended position, ready for the next ESD event. [58]

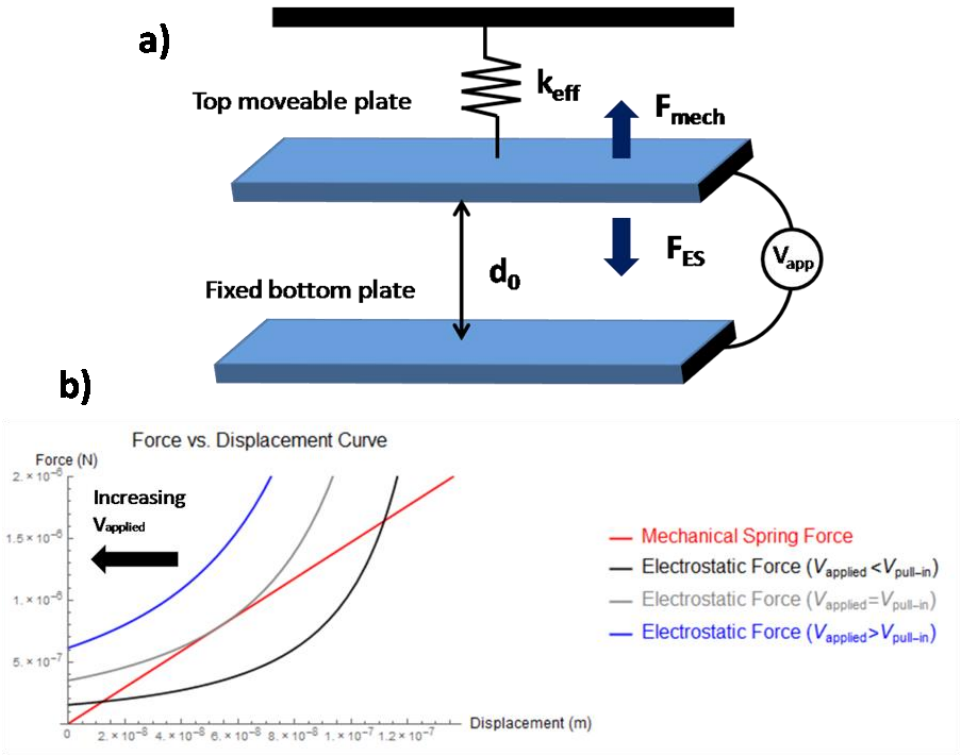

Fig. 2.7 Understanding the MEMS pull-in phenomenon using the capacitor plate model. a) Schematic of the capacitor plate model. b) Force vs. displacement curves for three different cases: 1) $V_{applied} < V_{pull-in}$, 2) $V_{applied} = V_{pull-in}$, and $V_{applied} > V_{pull-in}$. [60]

In order to understand the physics behind the MEMS pull-in phenomenon in greater detail, we can use the capacitor plate model, as seen in Fig. 2.7a. Here, the graphene ribbon, or any suspended structure for that matter, can be represented by two capacitors in which the bottom is fixed and the top is attached to a hanging spring with an effective spring constant, k_{eff}. When a voltage, $V_{applied}$, is applied across the two plates, an attractive electrostatic force, F_{ES}, is induced and the top plate is allowed to move towards the bottom. In doing so, there is a mechanical restoring force, F_{mech}, which fights against that movement. F_{ES} and F_{mech} are given by the following equations [57-58]:

$$F_{ES} = \frac{\varepsilon_0 A {V_{app}}^2}{2\left(d_0 - d(t)\right)^2} \tag{2.1}$$

$$F_{mech} = k_{eff} d(t) \tag{2.2}$$

ε_0 is the vacuum permittivity, A is the effective area of the plate, d_0 is the initial distance between the plates (the trench depth), and d(t) is the time-dependent displacement of the top plate.

Fig. 2.7b shows the force vs. displacement curve of the F_{mech} and the F_{ES} for three different cases. F_{mech} is represented by the red line. At small voltages, F_{ES} is represented by the black curve. In this case, F_{mech} and F_{ES} intersect at two different points, which means that there exist two equilibrium states where F_{mech} can balance F_{ES}. The smaller displacement represents a stable equilibrium state whereas the larger displacement represents an unstable equilibrium state; therefore, the ribbon physical sits at the smaller displacement. When $V_{applied}$ is increased, the F_{ES} curve shifts to the left, as seen in Fig. 2.7b and in Eq. (2.1). Eventually, we get to a situation where the F_{mech} and F_{ES} curves only intersect at one point, as seen with the gray curve. The voltage that brings us here is called the pull-in voltage ($V_{pull\text{-}in}$) because if $V_{applied}$ is beyond that value, we get a situation as seen with the blue curve. Here, there are no equilibrium states in which the F_{mech} can balance F_{ES}. What physically happens is F_{ES} takes over due to its $(d_0 - d(t))^2$ dependence, and the graphene ribbon collapses to the floor. Again, this creates a low impedance path between the top and bottom terminal of the device and allows the surge of charge from an ESD event to dissipate through the floor, providing ESD protection. [58]

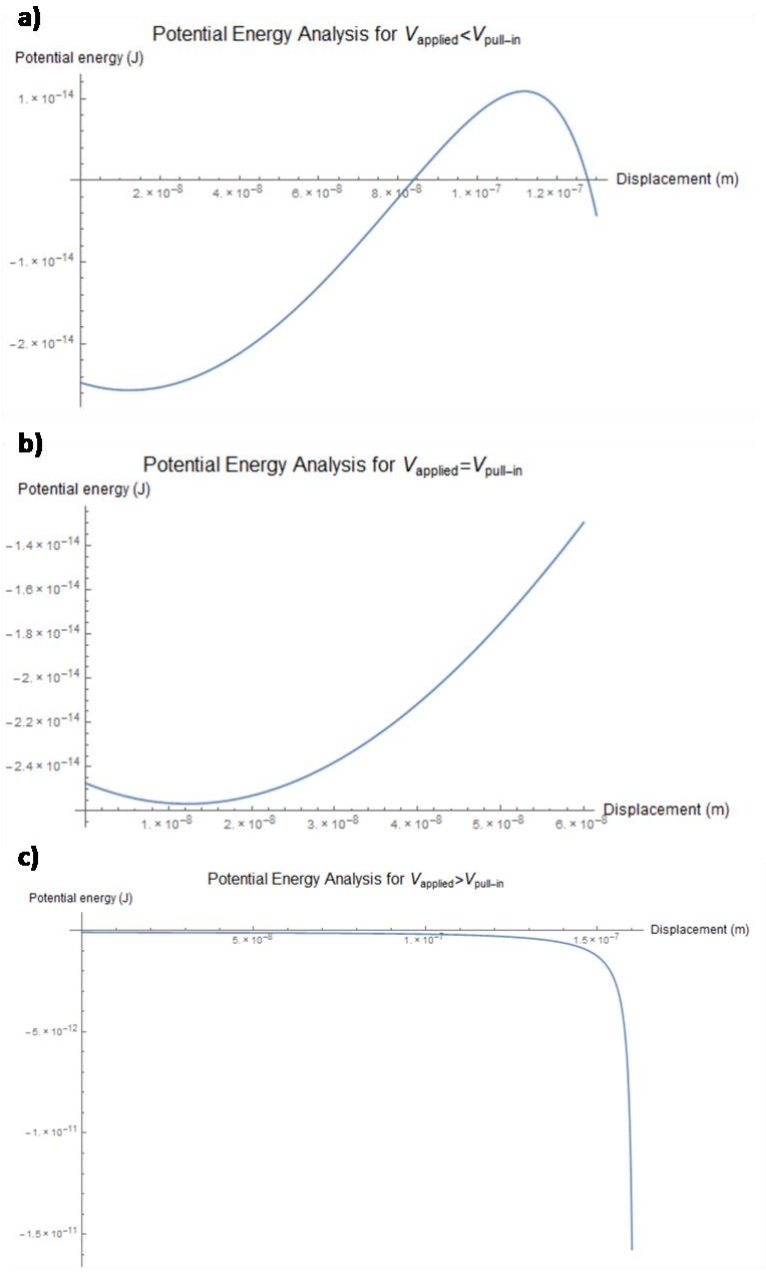

Fig. 2.8 Potential energy vs. displacement curves for the following three cases: 1) $V_{applied} < V_{pull-in}$, 2) $V_{applied} = V_{pull-in}$, and $V_{applied} > V_{pull-in}$. [60]

Fig. 2.8 explores the aforementioned MEMS pull-in phenomenon from a potential energy point of view. The potential energy was obtained by integrating F_{ES} - F_{mech} with respect to the

displacement. Fig. 2.8a shows the case for when $V_{applied} < V_{pull\text{-}in}$. Here, the minima and maxima correspond to where the F_{mech} and F_{ES} curves intersect in Fig. 2.7b. As seen in Fig. 2.8a, smaller displacement corresponds to a stable equilibrium position, a minima on the potential energy curve. This is where the ribbon physically sits. The larger displacement corresponds to an unstable equilibrium position, a maxima on the potential energy curve, and has no physical importance. When $V_{applied} = V_{pull\text{-}in}$, there is only one minima, corresponding to the only intersection point on Fig. 2.7b. When $V_{applied} > V_{pull\text{-}in}$, there are no minima, meaning that there are no equilibrium states where F_{mech} can balance F_{ES}.

By analyzing the situation in which F_{mech} and F_{ES} curves intersect at only one point in Fig. 2.7b, we can obtain an analytical expression for $V_{pull\text{-}in}$, which is given by the following equation [60]:

$$V_{pull-in} = \sqrt{\frac{8k_{eff}{d_0}^3}{27\varepsilon_0 A}} \tag{2.3}$$

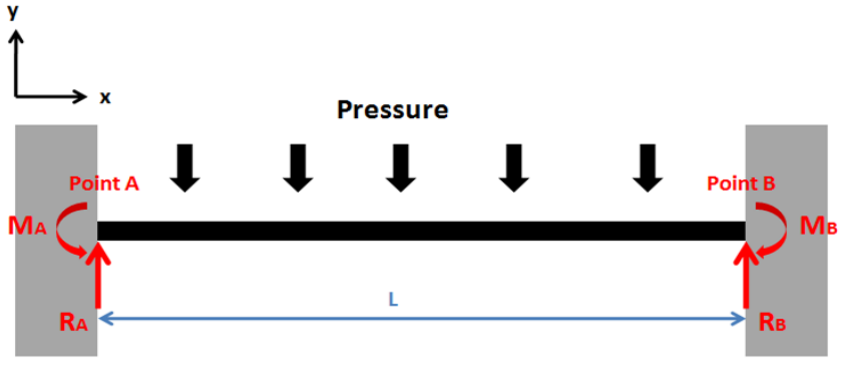

Fig. 2.9 The graphene ribbon modeled as a suspended beam clamped at both ends to obtain the k_{eff}. [62]

In order to get an analytical expression of $V_{pull\text{-}in}$ for our specific graphene ribbon case, we can analyze the generalized MEMS structure of a suspended doubly-clamped beam [63], as seen in Fig. 2.9. Here, the electrostatic force is assumed to be applied uniformly downwards across the beam. R_A and R_B are reaction forces at points A and B respectively. M_A and M_B are reaction moments at points A and B respectively. The deflection equation for this case is given by the following [62]:

$$EI\frac{d^2y}{dx^2} = M_A + R_A x \tag{2.4}$$

E is the Young's modulus of the beam and I is the moment of inertia. Integrating to solve for y in Equation 2.4 yields the following [62]:

$$y = \frac{M_A x^2}{2EI} + \frac{R_A x^3}{6EI} \tag{2.5}$$

Furthermore, for the case of the doubly clamped beam, the moment of inertia is given by the following [62]:

$$I = \frac{wt^3}{12} \tag{2.6}$$

w is the width of the beam and t is the thickness. Next, to calculate the k_{eff}, we invoke the general definition for the effective spring constant [62]:

$$k_{eff} = \frac{P}{y_{\frac{L}{2}}} \tag{2.7}$$

L/2 is the position at the midpoint of the beam. We defined k_{eff} using this position because the midpoint experiences the greatest amount of deflection; therefore, it is the location of interest

when we are looking to analyze pull-in. Substituting x = L/2 and Eq. (2.6) into Eq. (2.5) and then substituting that result into Eq. (2.7) yields the following [62]:

$$k_{eff} = \frac{32Ewt^3}{L^3} \tag{2.8}$$

Finally, by substituting Eq. (2.8) into Eq. (2.3), we get an analytical expression for $V_{pull\text{-}in}$ that is dependent on the device dimensions and the material properties [57]:

$$V_{pull-in} \sim \sqrt{\frac{E{d_0}^3 t^3}{\varepsilon_0 L^4}} \tag{2.9}$$

Equation (2.9) is important because it is the voltage needed to make the graphene ribbon collapse and make contact with the floor; that is, if we are using the suspended graphene ribbon device for ESD protection, then $V_{pull\text{-}in}$ is the voltage at which the device turns on, also called the trigger voltage, and is a critical ESD protection parameter.

Another critical ESD protection parameter is the mechanical response time, t_r. Because ESD events are transient in nature, ESD protection devices should be fast enough to respond to the stray charge seen in typical ESD events. If the suspended graphene ribbon device is used for ESD protection, then t_r would be the time it takes for the graphene ribbon to collapse to the bottom when $V > V_{pull\text{-}in}$. t_r is calculated by solving the following equation of motion:

$$m\frac{d^2d(t)}{dt^2} = F_{ES} - F_{mech} \tag{2.10}$$

$$m\frac{d^2d(t)}{dt^2} = \frac{\varepsilon_0 A{V_{app}}^2}{2\big(d_0 - d(t)\big)^2} - k_{eff}d(t) \tag{2.11}$$

The displacement of the ribbon as a function of time, d(t), is numerically solved for using Eq. (2.11). Then, t_r can be solved for by setting the displacement equal to the trench depth and then solving for the time:

$$d(t_r) = d_0 \tag{2.12}$$

There is also an electrical response time that must be acknowledged, the characteristic RC time. This tells us how much time it takes for the ribbon to charge up, so F_{ES} will act on it. I will not be taking this response time into account because it turns out that the electrical response time is many orders of magnitude below the mechanical response time in devices with dimensions of interest. Therefore, the ribbon can be approximated to charge instantaneously and how quickly the device can respond to an ESD transient is limited by the mechanical response time.

Another critical ESD protection parameter is the parasitic capacitance, $C_{parasitic}$, which is due to the graphene-air-Si p++ structure. Assuming that device will be used to protect semiconductor ICs from ESD, $C_{parasitic}$ is critical in that it could interfere with the IC's clock speed. A higher $C_{parasitic}$ means that it takes longer for things to charge up; therefore, it decreases the switching frequency. $C_{parasitic}$ is given by the following equation:

$$C_{parasitic} = \frac{\varepsilon_0 A}{d_0} \tag{2.12}$$

Of course, there are many other ESD protection parameters that must be taken into account if a device is to be used for actual ESD protection. I only covered the most important ones here for brevity.

2.4 Device fabrication

In this section, I will briefly go over the fabrication of the suspended graphene device, as outlined in Fig. 2.10. First, I begin with a Si p++ substrate and then a layer of thermally grow SiO_2 and deposit a 100 nm layer of SiN using PECVD (Fig. 2.10a). The Si p++ acts as the conducting floor of the device and the SiO_2 thickness determines the trench depth of the device. Then, photolithography and reactive ion etching is done to etch away trenches in the SiN (Fig. 2.10b). Part of the SiO_2 is exposed, so the graphene ribbon can be suspended later on. SiO_2 is also exposed around the perimeter of the chip. Next, another round of photolithography and HF-BOE is done to expose the Si p++ at the perimeter of the chip (Fig. 2.10c). Then, CVD graphene is grown and transferred onto the substrate, as described in sections 1.5 and 1.6 respectively (Fig. 2.10d). Then, another round of photolithography and O_2 plasma etching is done to pattern the graphene into the desired designs (Fig. 2.10e). Then, one last step of photolithography and e-beam metal deposition is done to deposit Ti/Pd/Au contact pads (Fig. 2.10f). There are two contact pads that are placed at the ends of the ribbon. There is third contact pad that is placed 50 μm away from the second, which form a metal network and a fourth contact pad connected to the Si p++ floor. Finally, HF vapor etching is used to dig out the trench under the graphene ribbon and the third and fourth contact pads shown are soldered together (Fig. 2.10g and h). This allows the metal network to be connected to the Si p++ floor and makes it easier for us to make measurements within a microscope field of view. The red arrows in Fig. 2.10h indicate where probe tips are placed to make pull-in I-V curve measurements.

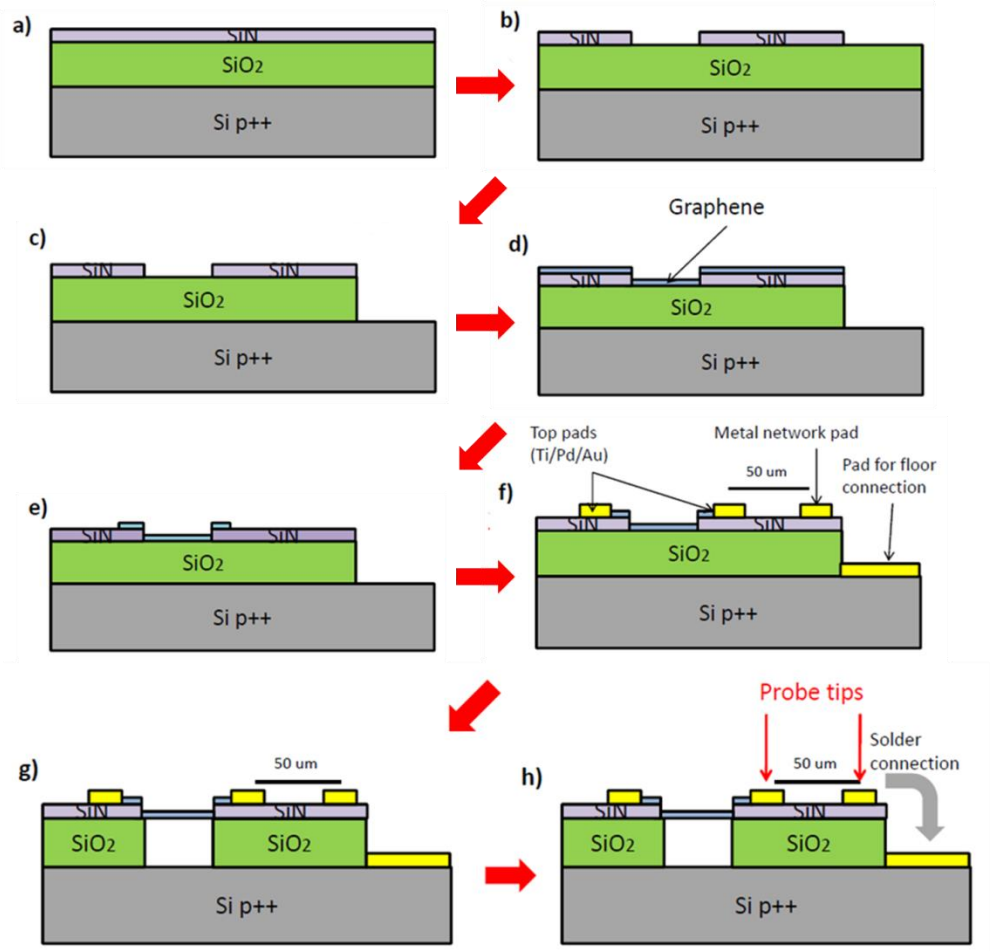

Fig. 2.10 Process flow for device fabrication.

2.5 Characterization

The three main techniques used to characterize the suspended graphene ribbon device for ESD protection: SEM, Raman, and electrical measurements (DC and TLP). SEM images were taken of the devices to ensure proper fabrication. A top view SEM image is shown in Fig. 2.11 as an example [64].

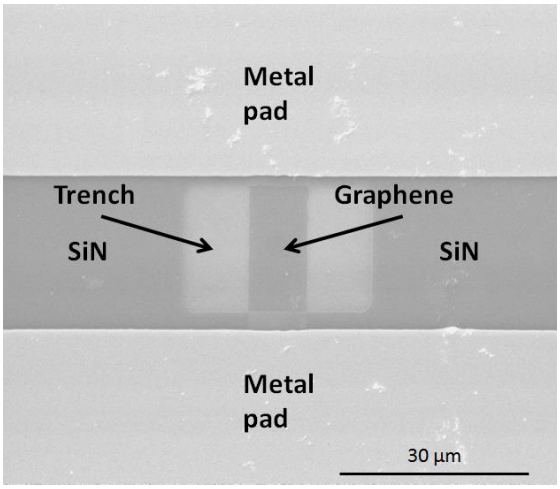

Fig. 2.11 Top view SEM image of the as-fabricated suspended graphene ribbon device [64].

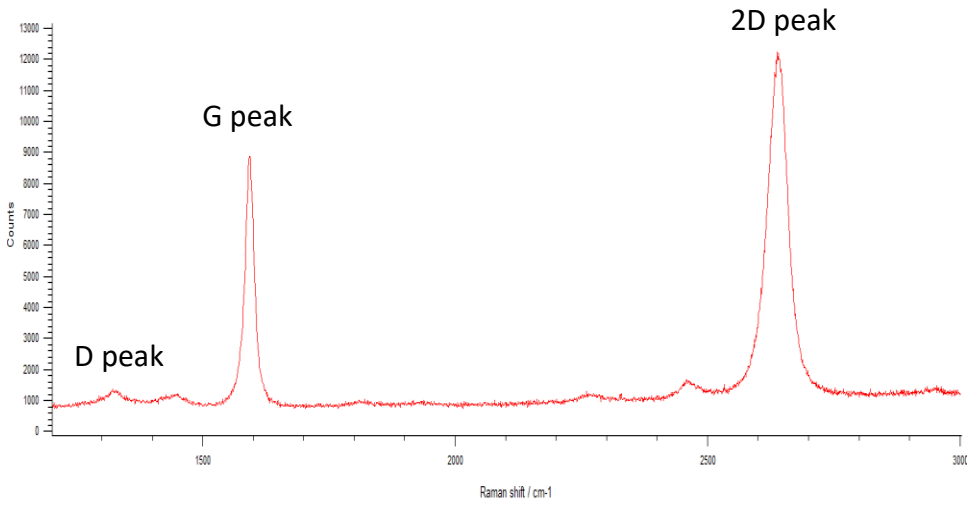

Fig. 2.12 Typical Raman spectrum of single layer graphene.

Furthermore, Raman spectroscopy was used to ensure that the graphene ribbon was intact and was of high quality. A review of Raman spectroscopy of graphene is given in section 1.7. An

example Raman spectrum experimentally obtained from the graphene we used to make our devices is shown in Fig. 2.12.

Lastly, the device's pull-in behavior was measured using DC and TLP probe stations. Pull-in I-V curve measurements were made using the measurement scheme shown in Fig. 2.10h. DC measurements are commonly done, so I will not cover them here. However, I will talk briefly about TLP, or transmission line pulse, measurements because they are important in ESD industry. TLP pulses are used simulate ESD shocks, which is why they are used in standardized ESD testing. According to the human body model, an ESD event is characterized by a constant charge discharge via transient surge, not a constant DC voltage. The rise time and duration time of the TLP pulse are made to match with the parameters set by the human body model, which are set to 10 ns and 100 ns respectively. An I-V curve is obtained from the TLP measurements by subjecting the device to these pulses while incrementally increasing the pulse height and then measuring the response. The pulse height and the current generated represent the voltage and current on the I-V curve respectively. [51] The BARTH Model 4002, the machine used for TLP testing, is shown in 2.13.

Fig. 2.13 BARTH Model 4002 TLP tester used for TLP testing.

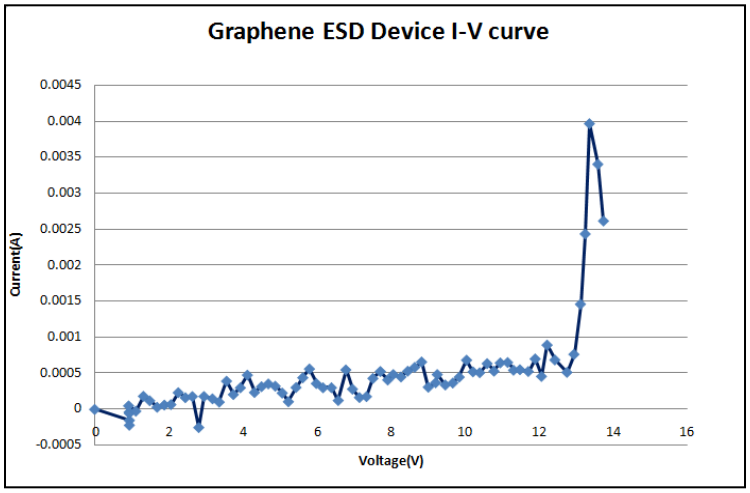

Fig. 2.14 Pull-in I-V curve obtained from TLP testing on a suspended graphene ribbon device with dimensions length = 7 μm, width = 5 μm, and trench depth = 850 nm.

A typical I-V curve taken from the TLP tester is shown in Fig. 2.14 as an example. As expected, at low voltages, the current is also low. However, at shortly above 12 V, there is a sharp increase in the current. At this point, the graphene ribbon pulls in and collapses to the floor, resulting in a low impedance path between the top pad and bottom pad of the device. In this way, the $V_{pull\text{-}in}$ of as-fabricated devices can be experimentally measured. Pull-in I-V curves were also obtained using DC; however, they show very similar behavior and are not shown here for brevity.

2.6 Experimental studies on the electromechanical responses of suspended graphene

In this section, I describe experimental studies on the electromechanical responses of our suspended graphene ribbon devices with the characterization methods as described in section 2.5. First, SEM and Raman spectroscopy were done to ensure device fabrication went well and the graphene ribbons are intact. Then, pull-in I-V curves were obtained using a DC probe station for suspended graphene ribbon devices with various lengths and trench depths to see if the results held up to theory. Pull-in I-V curve results are shown in Fig. 2.15. Here, pull-in I-V curves for different cases are superimposed on the same graph. For example, Fig. 2.15a shows pull-in I-V curves for devices with the same length but varying trench depths (350, 550, and 850 nm). Fig 2.15b shows devices with the same trench depth but varying lengths (7, 10, 15, and 20 μm). [65]

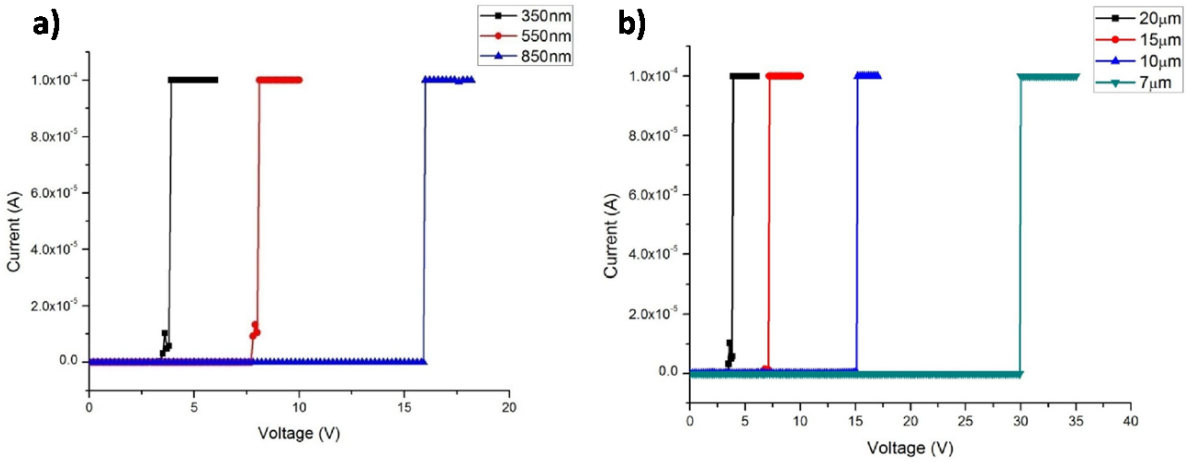

Fig. 2.15 a) I-V curves of suspended graphene ribbons with varying trench depth.

b) I-V curves of suspended graphene ribbons with varying length. [65]

From Fig. 2.15, we can see that the observed functional dependences match those predicted by our theoretical model: $V_{pull\text{-}in} \alpha d_0^{3/2}$ and $V_{pull\text{-}in} \alpha 1/L^2$. However, it is important to note here that the pull-in I-V curves seen on this figure are representative of a collection of pull-in I-V curves of the same dimensions. In actuality, there is variation $V_{pull\text{-}in}$ among devices with the same dimensions. It is only by averaging the measured $V_{pull\text{-}in}$'s that we find the aforementioned functional dependences. A follow-up study was done on the cause of this variation, and we found that it was due to significant structural contributions from polymer residue in the transfer and photolithography steps during device fabrication. The details of this study can be found in chapter 4.

The same pull-in I-V curve measurements were also done using the TLP probe station presented in section 2.5. The results were similar to that of the DC measurements and were not

included here for brevity. However, it is important to note that the TLP pulses used here were 100 ns, showing that the suspended graphene ribbons can effectively respond to transient shocks on this time scale.

To conclude this chapter, I will leave some remarks to summarize the results and leave the reader with takeaways. It turns out that our experimental results show suspended graphene ribbons can be modeled using the models mentioned in section 2.3. This gives us a set of equations we can use to design suspended graphene ribbon devices for ESD protection. Furthermore, compared to traditional Si devices, this reveals a novel and simpler way of providing ESD protection, in which ESD protection parameters can be easily tuned by modifying the device geometry. Lastly, by doing TLP pull-in measurements, we showed that the ribbons can respond to transients up to 100 ns and satisfy stringent ESD industry requirements.

Chapter 3: Nail structure optimization

3.1 $V_{pull\text{-}in}$ reliability issue

Unfortunately, the results shown in section 2.5 and 2.6 from the previous chapter conceal a very important problem: the device pulls-in as expected the first time a measurement is made but fails to pull-in again with every subsequent measurement. Fig. 3.1 illustrates what I mean. Here, the pull-in I-V curve was measured for the device shown in Fig. 2.14 ten times. The first measurement yielded expected pull-in behavior. However, all subsequent measurements showed resistor-like behavior. We believe the reason for this is as follows. After the first measurement, the ribbon experiences pull-in and collapses to the floor. However, due to slippage between graphene and the layers of metal and the SiN it is sandwiched between, graphene remains collapsed and does not return to its original suspended position after the electrostatic bias has been released. As such, there is a permanent connection between the top metal pad and the floor of the device, resulting in resistor-like behavior on the I-V curve for each subsequent measurement.

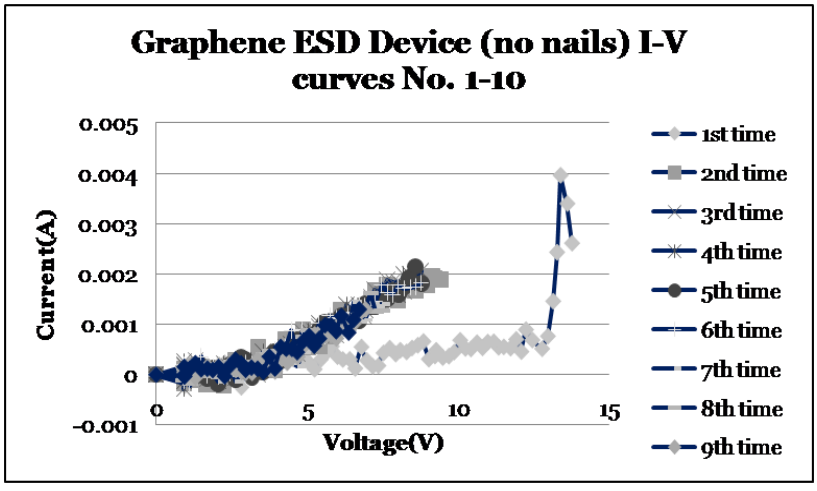

Fig. 3.1 Pull-in I-V curve measured on the same device 10 times.

If this device was used for ESD protection applications, this would mean that the device would just protect against only the first ESD shock it senses. Therefore, there is a $V_{pull\text{-}in}$ reliability issue. To remedy this, holes were "drilled" into where the graphene meets the metal pad, and then metal was deposited over it creating pillars that act as nails to pin the graphene ribbon down. The remainder of this chapter details the challenges in implementing nails.

3.2 Investigation of various nail structures using finite element simulations

In designing the geometry for the nail structures, the primary goal was to minimize the stress concentration where the nails and graphene sheet met when the ribbon pulled-in. Fig. 3.2 shows the various nail structures we decided to study [38].

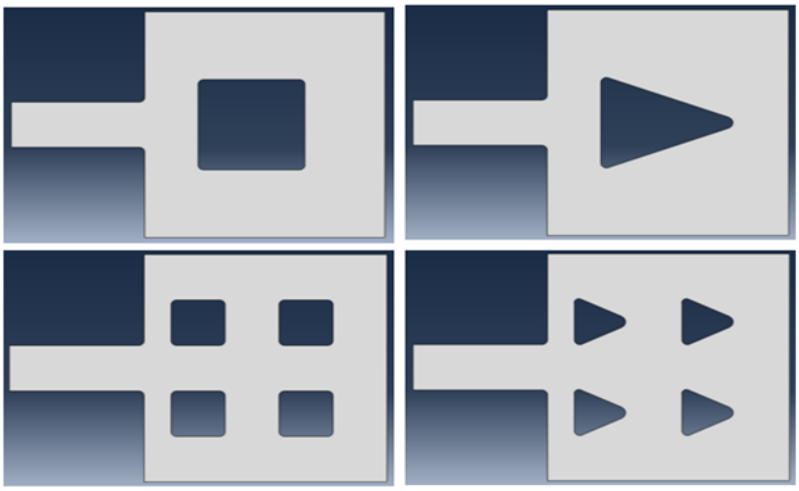

Fig. 3.2 Four different nail structures we chose to study in an attempt to minimize the stress concentration on the graphene sheet during pull-in. [38]

If you intuitively thought that circular nails would work best and were wondering why we chose to investigate nails with sharp edges, then you would be correct. It turns out that circular

nails do work best, and I will discuss this later. However, our reasons for choosing to the nail structures shown in Fig. 3.2 are due to the photolithography limitations we have. It turns out that to draw a circle on the photomask, it must be made of a collection of straight lines. Therefore, the resolution limitations of the mask writer you use and how small you want your circle to be determines how "blocky" your circle will turn out. Our limited "pad real estate" imposes a constraint on how small of a decent circle can be achieved. What we chose to do in this situation was to simply use square and triangle nails study the system in question before proceeding to determine which nails would minimize stress concentration.

Finite element simulations were conducted to study the behavior of these nail structures. Here, the graphene sheet was assumed to have material properties of polycrystalline graphene with grain sizes on the order of μm, which is what we make using CVD growth in our lab. The nails were assumed to be fixed rigid bodies, and the sharp edges were rounded to avoid any singularity points. The mesh density around sharp corners was increased for better accuracy because we expected stress to be concentrated there.

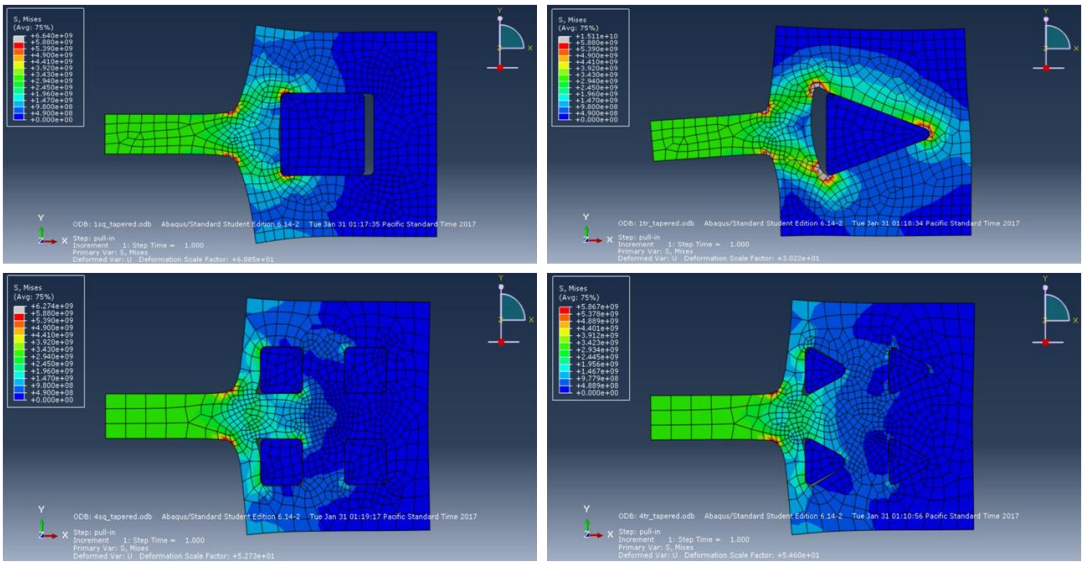

Fig. 3.3 Finite element simulation results of the four nail structures mentioned in this section. [38]

The simulation results are shown in Fig. 3.3. Pull-in was simulated by exerting a force pulling the graphene sheet to the left. The scale bar was made the same among these simulations, making easier to compare the stress concentration among them. Furthermore, red and gray areas in the graphene sheet indicate where stress concentration is greatest whereas blue areas indicate little to no stress concentration. From these results, we came to the following conclusions. First, as expected, stress concentration is centralized at the sharp edges of the ribbon. However, it is important to note that stress concentration not only occurs where the nails meet the graphene sheet. Second, the structures with four nails reveal that the two nails in the back do not have much of an effect. The physical reason for this is as follows. By assuming the nails are rigid and fixed, when the graphene sheet is pulled, all the displacement in the sheet occurs near the

location of the front two nails. As such, the part of the graphene sheet behind the two front nails experience little to no displacement; therefore, there is no stress concentration there either. [38]

3.3 Optimized nail structure

Using the insights extracted from the results in previous section, we moved forward by running additional finite element simulations in hopes to minimize the stress concentration in the graphene sheet. It turns out that two nails side by side can effectively reduce the stress concentration. Knowing this allowed us to optimize our use of pad real estate and use circular nails. Here, we ran finite element simulations using the same assumptions as described in section 3.2 for circular nails with different size and at different locations that satisfy our fabrication constraints.

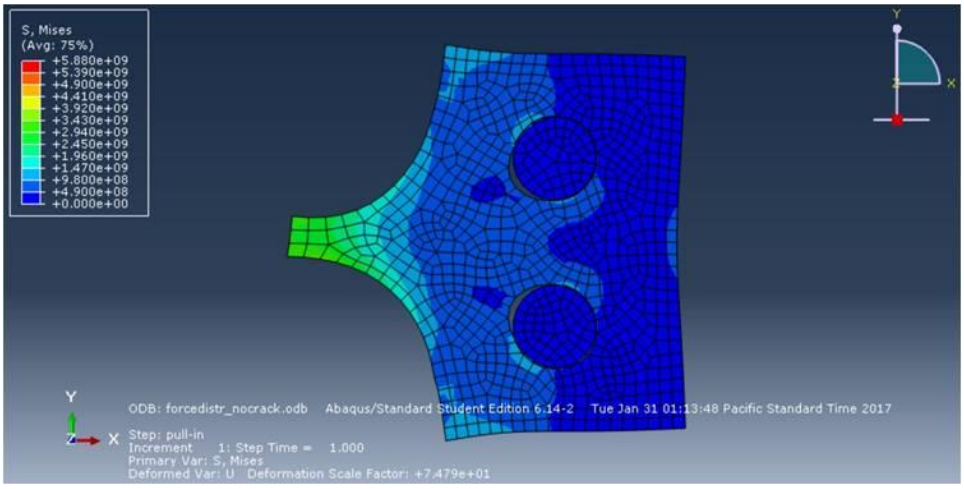

Fig. 3.4 Finite element simulation results of the optimized nail structure. [38]

After much iteration, we were able to find the optimal nail structure, and the simulation results for this is shown in Fig. 3.4 [38]. The scale bars were made the same as those in Fig. 3.3,

making it easier to compare stress concentrations across the different element simulations. It is also worthwhile to note that the region leading up to the ribbon was tapered to avoid sharp corners as much as possible.

To quantitatively measure how well this optimized structure distributes stress, a maximum stress to pull-in pressure ratio was used. This ratio is the maximum stress indicated on a simulation result divided by the pull-in pressure. A greater ratio means higher stress concentration, whereas a ratio closer to one means lower stress concentration. A ratio of one is the best achievable. Table 3.1 tabulates the ratios for the four nail structures shown in Fig. 3.3 and the optimized structure shown in Fig. 3.4. [38]

Nail Structure	**Value of interest**	
	Maximum stress (GPa)	***Maximum stress to pull-in pressure ratio***
One square nail	6.64	2.21
One triangular nail	15.11	5.04
Four square nails	6.27	2.09
Four triangular nails	5.88	1.96
Two circular nails (optimized structure)	3.61	1.20

Table 3.1 Table summarizing the maximum stress to pull-in pressure ratio for all the nail structures mentioned. [38]

As seen from Fig. 3.5, the ratios for the four nail structures from Fig. 3.3 vary greatly and the optimized circular nail structure is clearly the best. Furthermore, with a ratio of 1.20, it is

very close to the best achievable [38]. Therefore, the circular nail structure was implemented to pin down the suspended graphene sheet in our future devices.

3.4 Implementation of Nails into the Fabrication Process

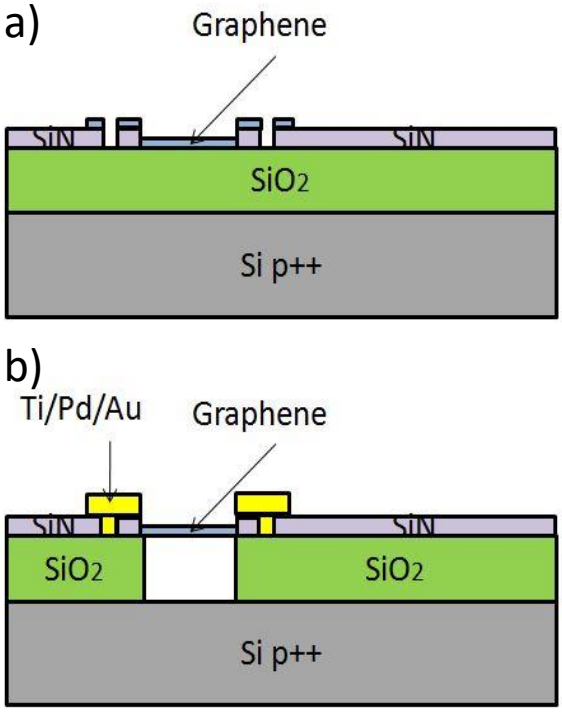

Fig. 3.5 Schematics illustrating how nails were implemented into the fabrication process.

Fig. 3.5 illustrates how nails were actually implemented into the fabrication process. Only a slight modification to the fabrication process outlined in Fig. 2.10 was made. First, when the SiN layer and graphene were etched (Fig. 2.10b and Fig. 2.10d respectively), holes were etched with the optimized nail structure design from section 3.3 at the location of the nails (Fig. 3.5a). Then, when metallization occurs (Fig 2.10f), the holes are filled with metal, effectively creating pillars that act as nails (Fig. 3.5b). The rest of the fabrication process does not change.

Chapter 4: Effect of Polymer Residue on the Pull-in of Suspended Graphene

4.1 Motivation for study

This next chapter addresses an issue introduced in chapter 2. The functional dependences obtained for the $V_{pull\text{-}in}$ presented in section 3.6 as were calculated using the *average* $V_{pull\text{-}in}$ for devices with varying dimensions. As we will explore in this chapter, it turns out that there is a variation in the *actual* $V_{pull\text{-}in}$ values. This chapter identifies the cause to be due to the variation in polymer residue thickness introduced during the device fabrication process and quantitatively assesses its effects. This study has implications in the manufacturing of suspended graphene MEMS devices with desired parameters (k_{eff}, $V_{pull\text{-}in}$, etc.).

First, in choosing to build MEMS devices with graphene, we must consider the trade-offs between two types of graphene: single crystalline (SCG) and polycrystalline (PCG) [66]. SCG has a Young's modulus of ~1 TPa, a fracture strength of ~130 GPa, and the ability to stretch up to ~1.25 times its original length before fracturing [16]. The fact that it is atomically thin means SCG is ideal for applications involving fast mechanical movement. Furthermore, SCG has a high charge carrier mobility (upwards of 15,000 cm^2/Vs at room temperature) [67]. Lastly, SCG has been shown to be chemically inert, which renders it easy to use and promising for use in biological systems [9].

Despite the progress that has been made in graphene research, it is still very difficult to produce large-area films (> 1 in^2) of SCG [28], [68]. Although, methods have been developed for growing large-area high-quality polycrystalline graphene (PCG) [68]. Concerns that the mechanical and electrical properties of PCG are far inferior to those of SCG due to the presence of grain boundaries were addressed in section 1.4. It has been shown that the sheet resistance of

PCG levels off after the grain size exceeds 10 μm because charge scattering within the grains becomes more significant than charge scattering due to the grain boundaries [22]. In regards to mechanical properties, PCG has imperfect C-C bonding at the grain boundaries, leading to diminished mechanical strength; however, it has been shown that PCG is still relatively strong and has a fracture strength of ~35 GPa [21], [64]. Thus, PCG typically suffices for many applications.

Currently, the most prominent method to produce PCG is chemical vapor deposition (CVD) on copper foil because of its low cost, large-area growth, good control of monolayer growth, and ability to transfer onto arbitrary substrates, as explained in section 1.5 [69]–[71]. For these reasons, PCG would be the realistic candidate in MEMS applications. Therefore, PCG is the focus of this study and will be referred to in the remainder of this chapter simply as graphene.

One hurdle in using CVD to grow graphene is the subsequent transfer process (outlined in section 1.6), which commonly involves spin-coating a thin polymer film (typically PMMA) onto graphene. The polymer acts a structural support while graphene is moved from the Cu foil onto the target substrate. Furthermore, any photolithography done after graphene has been transferred involves spin-coating polymer as well. The problem is that it is very difficult to completely remove the polymer and a thin residual layer remains (typically a few nanometers thick) [72], [73].

Our suspended graphene MEMS device, as well as many other graphene devices, involves the MEMS pull-in phenomenon in which a voltage bias is used to mechanically collapse a suspended structure. Although the pull-in of suspended graphene has been studied [56], [58], [74], the effects of polymer residue have been largely unexplored. It is known that polymer

residue p-dopes graphene, affecting graphene's electronic properties [13]. Furthermore, the polymer layer is relatively thick compared to the graphene [73] and should, therefore, have a mechanical effect on its behavior. For these reasons, we studied how polymer residue affects the pull-in of graphene, presenting the details of the study in this chapter.

4.2 Suspended graphene ribbon compliant mechanism design

To study the effects of polymer contamination on pull-in, the graphene ribbons were redesigned using compliant mechanisms and concepts introduced in chapter 2. First, the new suspended graphene structures' behavior was again assumed to be captured by the capacitor plate model, as shown in Fig. 2.7. This model yields Eq. (2.3) for $V_{pull\text{-}in}$. The difference between the $V_{pull\text{-}in}$ of the new designs and the old designs will be captured by the new k_{eff}.

The ribbons were made to have varying k_{eff} using three different lamina emergent mechanisms that could be patterned into the graphene [75], [76]. Each design consists of two main components: a combination of flexures and a platform [77]. The designs are shown in Fig. 4.1 and are named 1Blade, 2Blade, and Tiki. By lengthening the flexures using switchbacks, we increased the amount the platform can displace without failing but also decrease k_{eff} in the process. By adding more flexures in parallel, however, we compensated for this decrease in stiffness and still achieved a sufficiently high k_{eff}, ensuring we could easily experimentally make $V_{pull\text{-}in}$ measurements. Furthermore, 5 sizes were made (XS, S, M, L, and XL) for each design, in which the length of the flexures and the platform area, A, were increased. These changes affected $V_{pull\text{-}in}$, as shown in Eq. (2.3), which allowed us to study trends in the data we collected. We designed the ribbon to have a large platform region in the center, with areas ranging from 54 to 1260 μm^2.

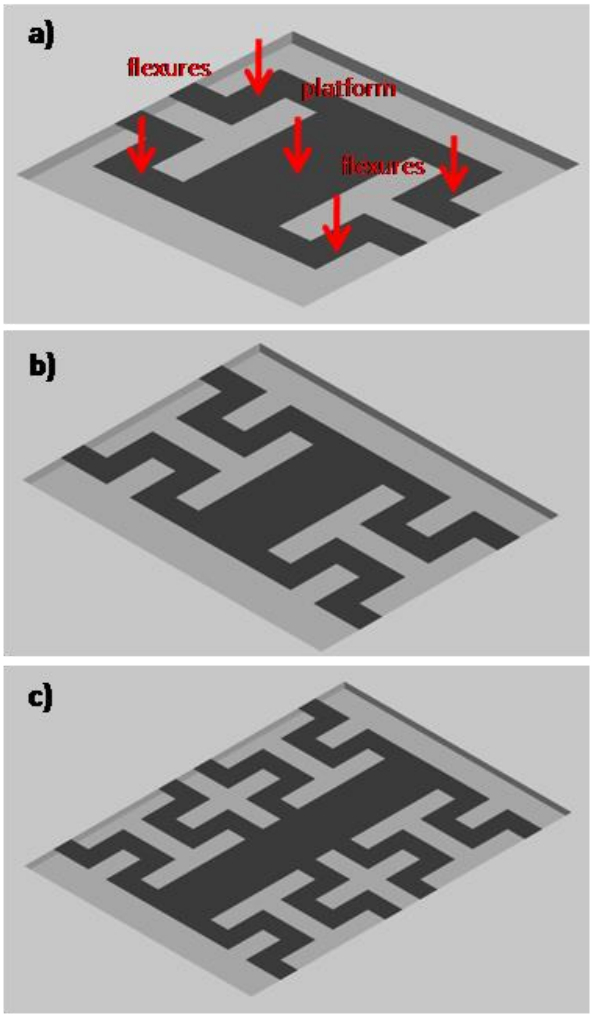

Fig. 4.1 Schematic of the graphene ribbon designs used in this study: a) 1Blade, b) 2Blade, and c) Tiki. The location of the flexures and the platform are indicated in Fig. 2a.

This choice of geometry made it possible to easily measure the relative polymer contamination levels using large-area Raman mapping because the laser spot size is ~ 1 μm in diameter. The flexures and platform mentioned are labeled in Fig. 4.1a. Finally, circular nails

were optimized and applied to prevent the graphene from slipping during pull-in, as described in chapter 3 [38].

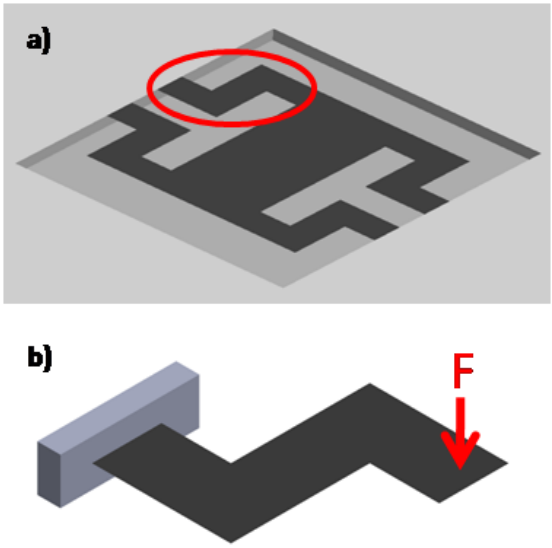

Fig. 4.2 Illustration showing how we calculated k_{eff} using Castigliano's Theorem. a) Flexure leg of 1Blade design. b) Location of where the downward force is assumed on the flexure leg.

We calculated the k_{eff} of each ribbon by treating each flexure leg as a spring in parallel holding up the center platform. We employed Castigliano's Theorem [78] to calculate the effective stiffness of each flexure leg, k_i. Fig. 4.2 shows how this was done using the 1Blade design as an example. First, we assumed that a downward vertical force, F, was applied where the flexure leg meets the platform to simulate platform movement during pull-in, as seen in Fig. 4.2b. Integrating the strain energy along each segment, we calculated the vertical displacement of each segment of the flexure leg. Then, we calculated k_i by dividing F by the total vertical displacement, following the general definition of the effective stiffness. After k_i was calculated,

we calculated k_{eff} by treating the flexure legs as springs in parallel holding up the center platform using the following equation:

$$k_{eff} = \left(\sum_i {k_i}^{-1} \right)^{-1} \tag{4.1}$$

We substituted k_{eff} and the geometric parameters into Eq. (2.3) to calculate $V_{pull\text{-}in}$ for each ribbon design and size. Table 4.1 summarizes the predicted relative $V_{pull\text{-}in}$ values for all the ribbons in our study, with the $V_{pull\text{-}in}$ of the 1Blade XL design normalized to 1 to show how the predicted $V_{pull\text{-}in}$ values incrementally change with the design and size.

		Design		
		1Blade (V)	2Blade (V)	Tiki (V)
Size	XS	9.32	3.87	3.87
	S	6.22	2.86	2.8
	M	2.65	2.34	2.3
	L	1.99	1.84	2.1
	XL	1	1.14	1.32

Table 4.1 Summary of predicted $V_{pull\text{-}in}$ in units of volts for all ribbons used in the study calculated using Eq. (2.3).

4.3 Device fabrication and characterization

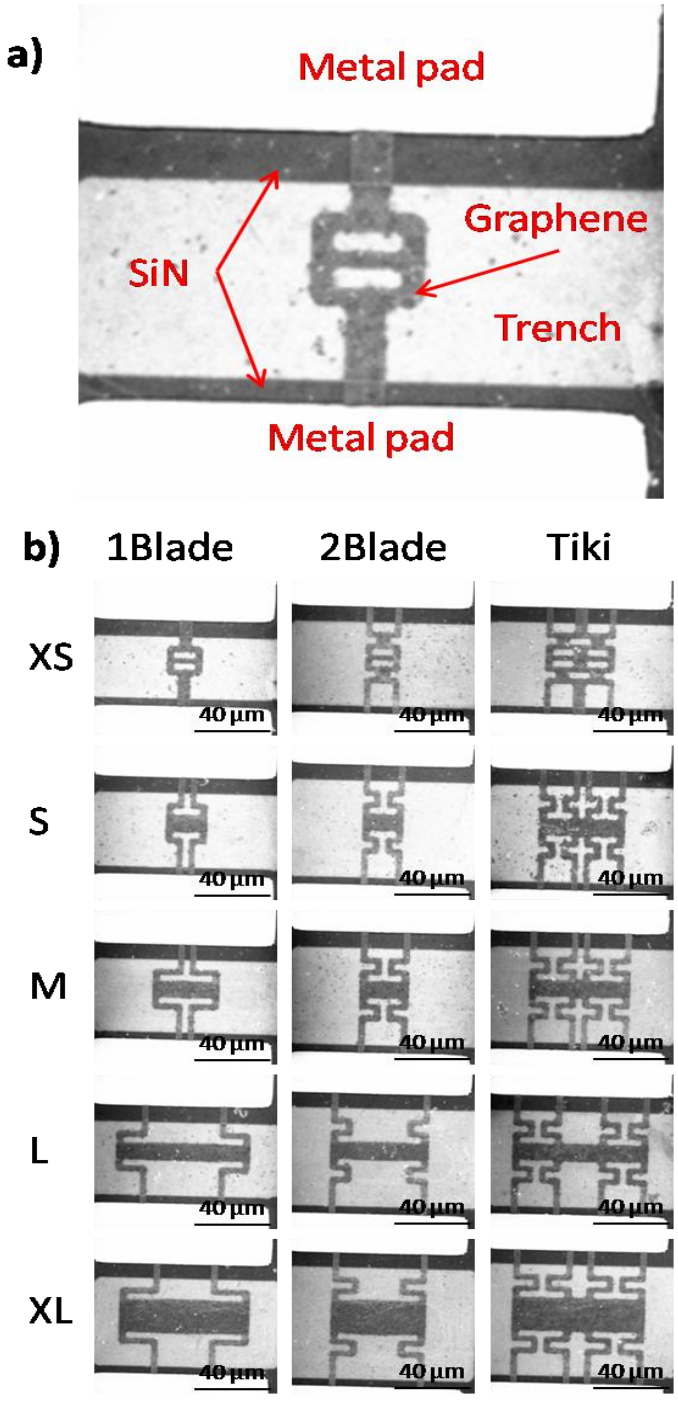

Fig. 4.3 Top-view SEM images of as-fabricated devices. a) 1Blade XS device with its relevant features labeled. b) Collage of all device designs and sizes used in the study.

The devices were fabricated using a process similar to the one outlined in section 2.4. The only difference is that during the O_2 plasma etching step, the graphene was patterned into the compliant mechanism designs we presented in section 4.2.

After device fabrication, the devices were characterized using SEM. Figure 4.3 shows top-view SEM images of the as-fabricated devices. Figure 4.3a shows a close-up of a 1Blade XS ribbon with relevant features labeled as an example. Figure 4.3b shows all the device designs and sizes used in this study.

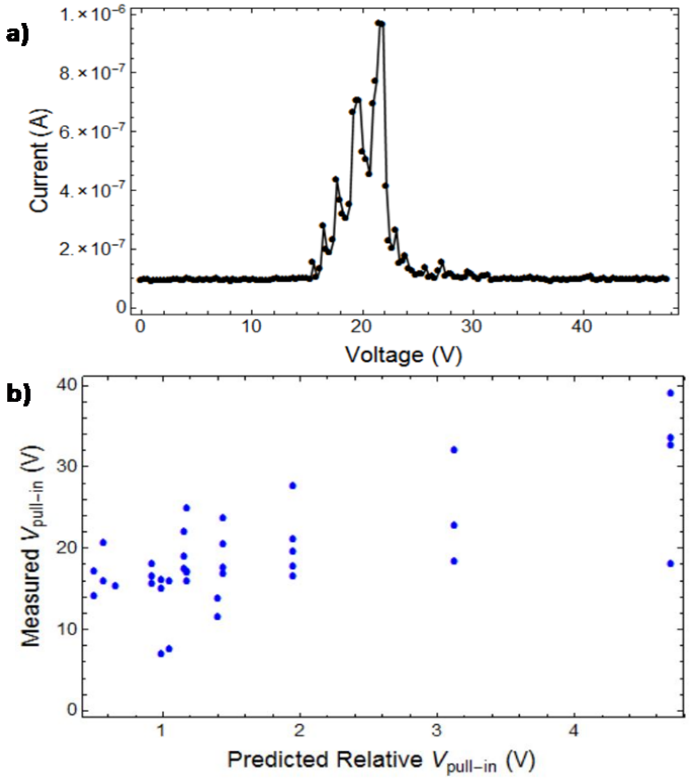

Fig. 4.4 a) Typical pull-in I-V curve, measured using 2Blade L device. b) The measured $V_{pull-in}$ plotted against the predicted $V_{pull-in}$ for devices studied from section 2.4.

To characterize the devices' pull-in behavior, we measured $V_{pull\text{-}in}$ by obtaining I-V curves using the measurement scheme shown in Fig. 2.10h. We then plotted the actual measured $V_{pull\text{-}in}$ against the relative predicted $V_{pull\text{-}in}$. The trend found was expected, but we also observed a significant variation in the measured $V_{pull\text{-}in}$, in which the aim of this study was to investigate. Figure 4.4a shows a typical pull-in I-V curve. At pull-in, there is a sharp increase in current because the graphene ribbon collapses to the floor, creating a low-resistance path between the top and bottom pad. The voltage that causes this sharp increase is the device's $V_{pull\text{-}in}$. At sufficiently high current, local heating effects cause parts of the graphene to react with oxygen in air to form CO_2, burning holes in the graphene and causing an open circuit as described by Chen et al. [54]. For this reason, breakdown occurs and the measured current plummets, as expected. $V_{pull\text{-}in}$ measurements were made for different devices and plotted against the predicted $V_{pull\text{-}in}$ in Fig. 4.4b.

4.4 Potential causes of $V_{pull\text{-}in}$ variation

To investigate the discrepancies between our predicted $V_{pull\text{-}in}$ values and the measured $V_{pull\text{-}in}$ values, we considered the effects of each geometric parameter on the $V_{pull\text{-}in}$. Any variation in these parameters due to fabrication error would cause variation in $V_{pull\text{-}in}$. For simplicity, we illustrate these effects here using the $V_{pull\text{-}in}$ of a simple solid doubly-clamped graphene ribbon, which is a function of ribbon thickness, width, and length. The stiffness values for the 1Blade, 2Blade and Tiki designs are also functions of ribbon thickness, width, and length and are of similar form. The equation for $V_{pull\text{-}in}$ of the simple solid ribbon is the following [58]:

$$V_{pull-in}^{simple\ ribbon} \sim \sqrt{\frac{E_g {t_g}^3 {d_0}^3}{\varepsilon_0 L^4}} \tag{4.2}$$

E_g is the Young's modulus of graphene, t_g is the thickness of graphene, and L is the length of the ribbon. Using Eq. (4.2), we identified the geometric parameters that influence $V_{pull\text{-}in}$: the trench depth d_0, the ribbon length L, and the thickness t.

To check if there was a variation in d_0, we measured the SiO_2 thickness at 10 different locations on the wafer. As shown in Fig. 2.10a, the SiO_2 thickness ultimately determines the trench depth. SiO_2 thickness measurements were done using the Nanospec Model #101-0180. We did the measurements at 10 points around the wafer and found that each point was within ~10 nm of the target SiO_2 thickness (1 μm). From this survey, we concluded that the variation in trench depth is not significant enough to cause the observed variation in $V_{pull\text{-}in}$.

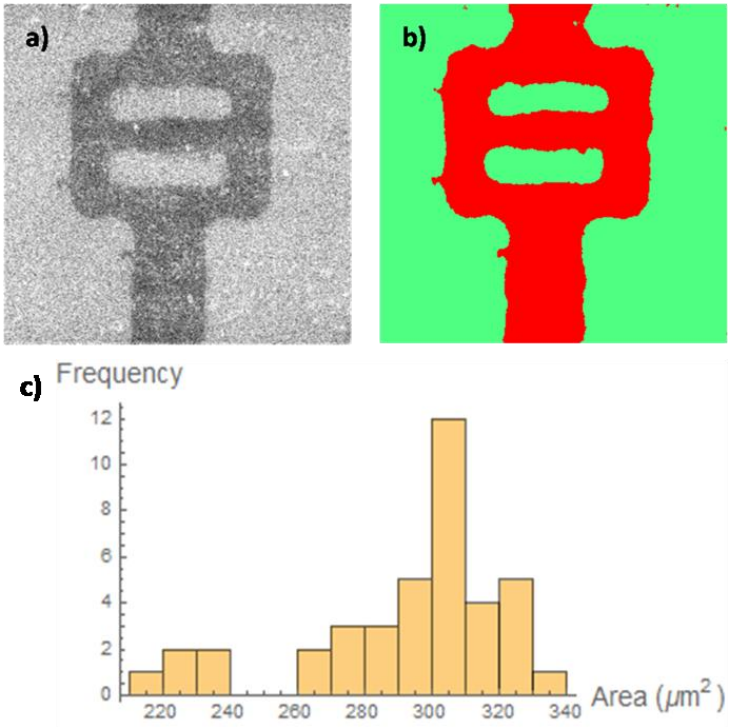

Fig. 4.5 a) SEM image of 1Blade XS ribbon and b) its image segmentation. c) A histogram of the calculated areas of 40 1Blade XS using image segmentation.

To investigate if there was variation in the area across devices of the same size and design, we measured the areas of the as-fabricated 1Blade XS ribbons. This is because these ribbons have the smallest area and thus are most prone to area variation. To check, we took SEM images of 40 1Blade XS devices. Next, we used ImageJ software to conduct image segmentation and calculated the actual areas of these ribbons. These areas were then compared to the expected area from our design. An example of a 1Blade XS ribbon SEM image and its image segmentation is shown in Fig. 4.5a and 4.5b respectively. We then made a histogram to check the variation in these areas, as shown in Fig. 4.5c. Using the histogram, we observe that the majority of the 1Blade XS ribbons fall within ~20 μm^2 of the expected area (306 μm^2). There are a few

ribbons that have areas ~200 to 240 μm^2. Upon further inspection, we found that these ribbons had many cracks due to damage endured during the fabrication process. However, from the SEM images and the histogram, we can see that the majority of ribbons are not damaged. From the many ribbons which were intact, we concluded that the area variation was not significant enough to cause the $V_{pull\text{-}in}$ variation.

To investigate the thickness, Raman spectroscopy was used to ensure our graphene was indeed monolayer. Figure 4.7 shows a typical Raman spectrum obtained from the graphene used to fabricate the devices. The Raman spectra indicate that the graphene is completely monolayer; therefore, there was no variation in the thickness of the graphene.

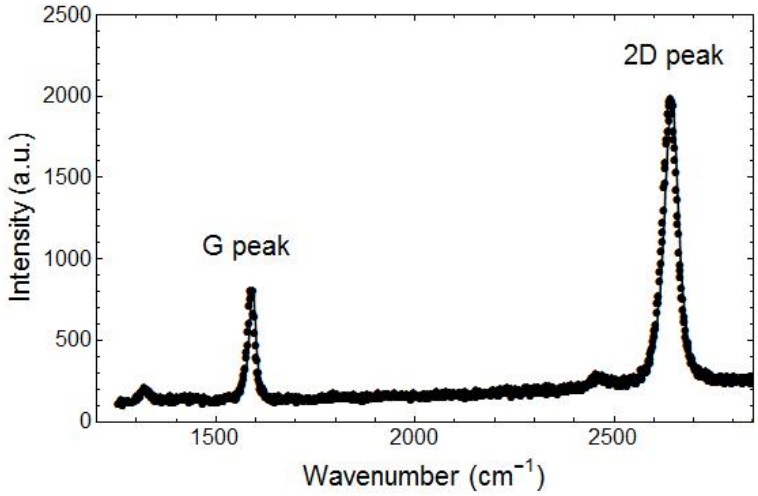

Fig. 4.6 Typical Raman spectrum of graphene from a ribbon, with its characteristic peaks (G peak and 2D peak) indicated.

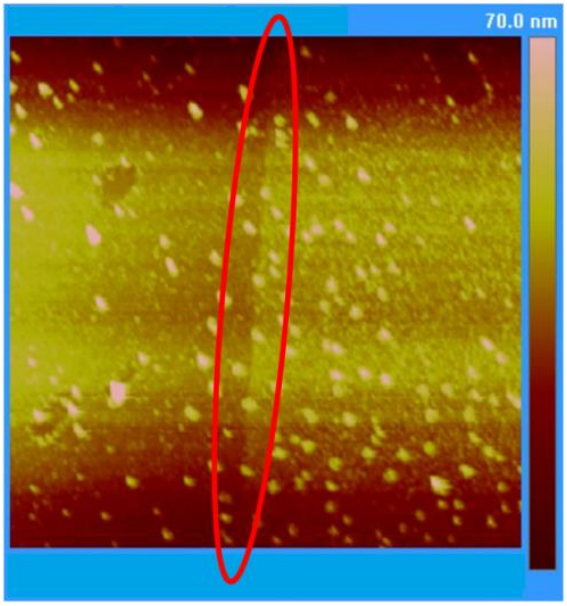

Fig. 4.7 AFM image used to measure the thickness of the polymer residue. The location of the step is circled in red.

However, polymer residue from the device fabrication process was also investigated because they are typically reported to be about a few nanometers thick [73]. Considering the fact that graphene is only one atomic layer, polymer residue can be relatively thick and can significantly affect the rigidity of the entire structure. Thus, variation in the polymer residue layer thickness can lead to $V_{pull\text{-}in}$ variation. In order to investigate the variation in residue thickness, an AFM image was taken of a 1Blade XS flexure leg before the SiO_2 was dug out using a Digital Instruments Multimode AFM, as shown in Fig. 4.7. We used the height contrast between SiO_2 and polymer/graphene to calculate the thickness of the polymer residue, assuming that the thickness of graphene is 0.34 nm [79]. The additional thickness of the polymer residue is approximated as a spring in parallel with the graphene ribbon, and a modified version of Eq. (4.2) was used to analyze the structural effects of the residue on $V_{pull\text{-}in}$:

$$V_{pull-in}^{simple\ ribbon} \sim \sqrt{\frac{(E_g {t_g}^3 + E_p {t_p}^3){d_0}^3}{\varepsilon_0 L^4}} \tag{4.3}$$

E_p and t_p are the Young's modulus and thickness of the polymer respectively. The AFM results are shown in Fig. 4.7. Using these results we calculated the thickness of the polymer residue to be 4.12 nm. Assuming graphene's thickness is 0.34 nm [79] and the polymer's Young's modulus is 3 GPa [80], the polymer residue thickness was significant enough to affect $V_{pull\text{-}in}$ according to Eq. (4.3).

In addition to being thick enough to affect $V_{pull\text{-}in}$, polymer residue, especially PMMA, is also known to p-dope graphene [13]. Therefore, we analyzed 75 ribbons to confirm whether there was variation in polymer residue by measuring p-doping in those ribbons. For each ribbon, 20+ Raman spectra were obtained using Raman mapping with a Reinshaw inVia Raman Microscope. To obtain the relative p-doping levels, we looked at the ratio of graphene's 2D peak intensity to G-peak intensity, I_{2D}/I_G [13]. We fitted each spectrum's 2D and G peak to a Gaussian sitting on top of a 3rd degree polynomial baseline and extracted the I_{2D} and I_G using Wire 4.3 software. Then, we calculated the average I_{2D}/I_G for each ribbon and used it to measure the relative doping level variation.

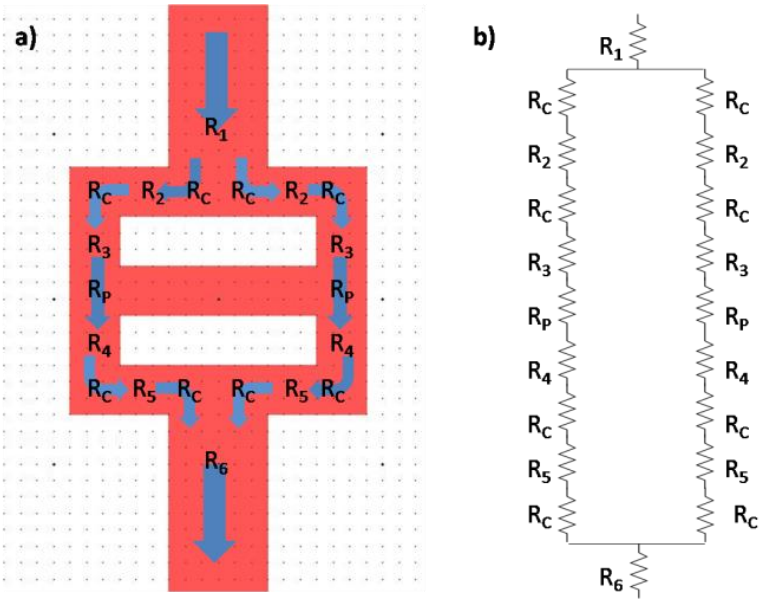

Fig. 4.8 Example of 1Blade XS ribbon modeled as a resistor network used to calculate its resistivity. a) A schematic of the 1Blade XS ribbon with blue arrows indicating the flow of current. b) The ribbon's corresponding resistor network.

We also ensured there was consistency in our results by measuring the resistivity of these ribbons. To do this, we treated each ribbon as a resistor network. Figure 4.8 shows an example of this modeling for the 1Blade XS ribbon. The resistance of each ribbon segment, R_i, was calculated using the following equation:

$$R_i = \rho \frac{L_i}{w_i} \tag{4.4}$$

ρ is the resistivity and L_i and w_i are the length and width of the segment respectively. This equation was modified from the common resistance equation of 3D bulk materials to fit 2D materials (area → width). We included resistances R_C and R_P representing where the current turned a corner and flowed across the platform respectively. By summing all the resistance

components in series and parallel, the through-the-ribbon resistance, R_{ribbon}, is given by the following equation:

$$R_{ribbon} = C\rho \tag{4.5}$$

C is a constant that depends solely on the geometry of the ribbon. This modeling was done for all ribbon designs in this study. Then, we experimentally measured R_{ribbon} of each ribbon and divided this value by its C value to calculate each ribbon's resistivity.

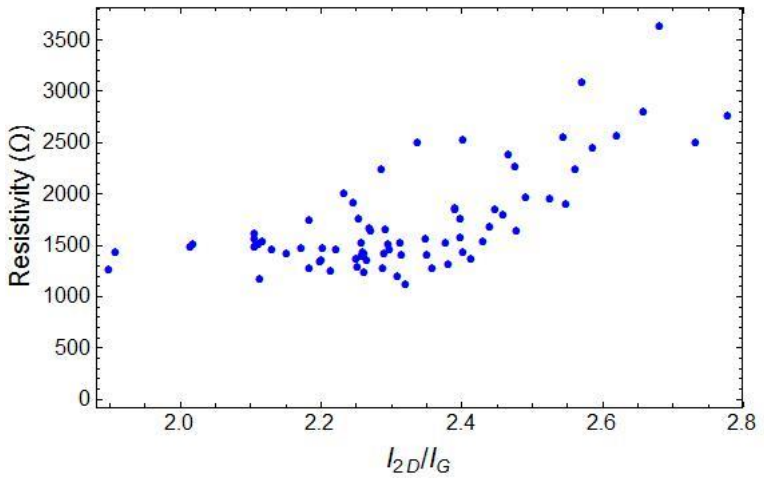

Fig. 4.9 Plot of the resistivity against the average I_{2D}/I_G of the ribbons studied. Regression analysis was performed by fitting what to a 5th degree polynomial. A coefficient of correlation of +0.81 was subsequently determined.

We then plotted average I_{2D}/I_G against the resistivities of the 75 ribbons, as seen in Fig. 4.9. Then, we conducted regression analysis by fitting the data set to a 5th degree polynomial, finding a coefficient of correlation of +0.81 and confirming a relationship between the average I_{2D}/I_G and the resistivities. From Fig. 4.9, we see that our results are consistent. Ribbons with a lower average I_{2D}/I_G have higher levels of p-doping and thus lower resistivity and vice versa [13].

Our results indicate that there is indeed a variation in p-doping levels and polymer residue thickness.

4.5 Polymer residue removal treatments

We then used a more effective polymer residue removal method and characterized the devices again to see if this method decreased the $V_{pull\text{-}in}$ variation.

We attempted the following polymer residue removal methods:

1. 2 hour acetone
2. 24 hour acetone
3. 3 hour vacuum anneal (base pressure ~ 10 mTorr) at 300 °C + 5 min air anneal at 450 °C
4. 1 hour chloroform

Method #1 served as a control; we used this throughout the device fabrication process introduced in section 2.4. Method #2 leaves the sample in acetone for a longer duration than in method #1, allowing more time for acetone to remove polymer residue. In method #3, the initial vacuum anneal was used to decompose the polymer into amorphous carbon; then, the subsequent air anneal was used to oxidize said amorphous carbon. Method #4 uses chloroform, a very toxic but more effective solvent.

We experimented with each method to remove polymer residue from graphene after the transfer and photolithography steps described in section 2.4. To characterize each method's effectiveness, Raman mapping was done at 20 different locations with each Raman map

consisting of 20+ points. Again, the average I_{2D}/I_G was calculated. We also extracted the 2D peak positions, pos(2D), from the spectra and calculated the average pos(2D) in the same way the average I_{2D}/I_G was calculated. We plotted the average I_{2D}/I_G against the average pos(2D) in Fig. 4.10, using them as metrics to measure the relative p-doping levels [13].

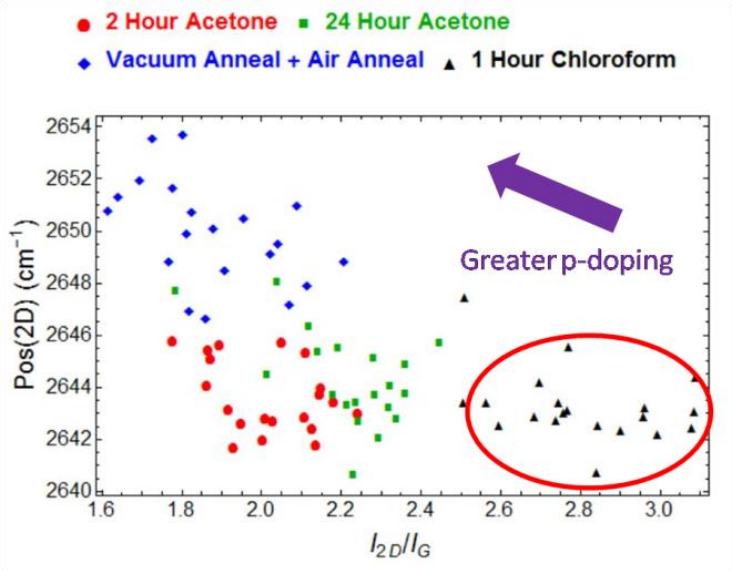

Fig. 4.10 Plot of average *pos(2D)* vs. average I_{2D}/I_G for ribbons studied. From these results, we found that chloroform was best at removing polymer residue (circled in red).

We found that method #4 worked best and then fabricated a new batch of devices using chloroform to remove polymer during the graphene transfer and photolithography steps. Then, $V_{pull\text{-}in}$ measurements were taken; however, all I-V curves obtained showed resistor-like behavior followed by breakdown, as shown in Fig. 4.11. By effectively removing the polymer residue, the graphene ribbon starts off collapsed touching the floor; there is already a connection between the top and bottom pad, resulting in resistor-like behavior as described Ng et al. [38].

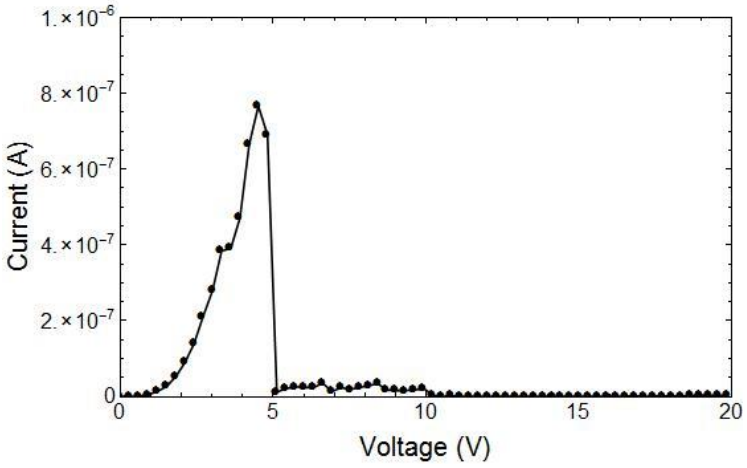

Fig. 4.11 Pull-in I-V curve of ribbon 1Blade XL ribbon treated with chloroform to remove polymer residue from graphene transfer and photolithography.

This phenomenon can be understood by performing an energy analysis of our system. Whether graphene begins suspended or not depends on the graphene-substrate interaction energy if graphene conforms to the substrate, $E_{g\text{-}s\ interaction}$, and the strain energy induced by graphene stretching, E_{strain}. The total energy of the system is given by this equation [81]:

$$E_{total} = E_{g-s\ interaction} + E_{strain} \tag{4.6}$$

$E_{g\text{-}s\ interaction}$ is negative because the attractive interaction between graphene and its substrate, albeit weak, reduces the total energy of our system. On the other hand, E_{strain} is positive because it requires energy to stretch graphene. If $|E_{g\text{-}s\ interaction}| > |E_{strain}|$, the energy reduced from graphene conforming outweighs the energy increased from graphene stretching. In this case, graphene will conform to the substrate. However, if $|E_{g\text{-}s\ interaction}| < |E_{strain}|$, then the opposite is true and graphene will remain suspended [81]. By using chloroform to remove polymer residue, we believe that strain energy required to stretch graphene was reduced, and the system moves

from the latter regime into the former regime. Therefore, we found that polymer residue on graphene plays two important roles: 1) its variation in thickness causes variation in $V_{pull\text{-}in}$ and 2) it helps to suspend the graphene by making it more energy intensive for graphene to conform to the substrate if the substrate is too corrugated.

4.6 Conclusion

In this chapter, we studied how polymer residue affects $V_{pull\text{-}in}$ of suspended graphene devices. By using an array of ribbon designs and sizes, we incrementally changed the stiffness and the area and thus $V_{pull\text{-}in}$. After fabrication, we observed a variation in $V_{pull\text{-}in}$ and investigated the cause. We found that polymer residue, although thin (4.12 nm), was relatively thick compared to graphene (0.34 nm [79]) and had a significant effect on the structure's rigidity and $V_{pull\text{-}in}$. Variation in the polymer residue thickness was confirmed, and it was identified to be the cause of the variation in $V_{pull\text{-}in}$ through process of elimination. Furthermore, after removing the polymer residue with a more effective chloroform treatment, we found that the graphene structure was no longer able to suspend itself due to the decreased strain energy needed to collapse the graphene ribbons. Therefore, polymer residue was found to cause variation in $V_{pull\text{-}in}$ but was also found to help in graphene's suspension if the substrate is too corrugated.

Chapter 5: Modeling of a Suspended Graphene Resonator for High Frequency DC-to-AC Conversion

5.1 Introduction

Before I begin, I want to make clear that the project in this chapter is different than the projects in the previous chapters. To give you some context, as I was studying the electromechanical responses of suspended graphene, my PI had an idea simmering in the back of his mind. The idea was to use the device that we've been studying for another application: as resonator for high frequency DC-to-AC conversion. Towards the end of my PhD, we decided to pursue this idea, which lead to me doing a theoretical (modeling) study investigating the resonator's feasibility. The remainder of this chapter presents the details of this study.

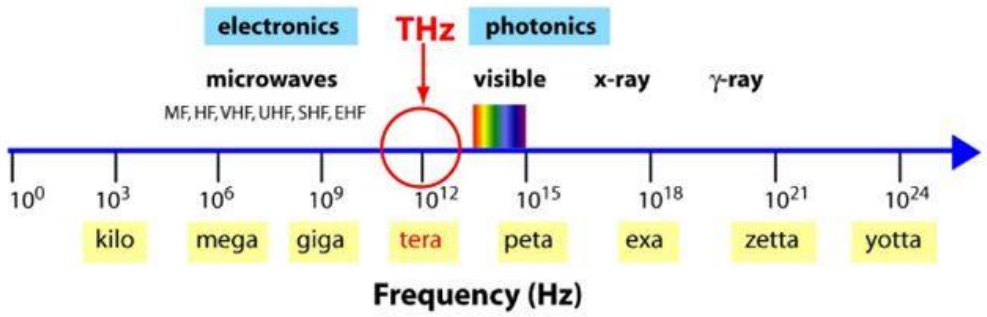

Fig 5.1 THz gap within the electromagnetic spectrum [82].

The history of using MEMS devices for high frequency applications started in 1991 when L. E. Larson presented a MEMS switch that had switching frequencies up to ~0.1 GHz [83]. Since then, the frequency of MEMS devices has incrementally climbed and these devices have slowly attempted to infiltrate the infamous "THz gap" (~0.1 to 10 THz) [84], the band of

frequencies in which practical technologies for generating and detecting radiation do not exist, as shown in Fig. 5.1. Being able to generate THz radiation is important because the radiation is non-ionizing, compatible with biological materials, able to penetrate visibly opaque objects, and interacts strongly with water. For these reasons, advancement of THz technology has applications ranging from medical imaging to national security. The reason for this gap is that we run into limits when trying to innovate with mature technology from either side of the gap. Using electronic generators to come in from the left side is impractical at THz frequencies because power is too low. Using photonics that depend on electronic transitions in atoms and materials to come in from the right side also fails because the photons emitted are generally too energetic. Due to these reasons, this gap has remained difficult to fill and is an ongoing research topic to this day. [82]

Novel devices that combine MEMS and nano-materials, such as graphene, allow production of sufficiently high frequency signals and offers potential for further penetration into the THz gap. Single crystalline graphene has a Young's modulus of ~1 TPa, a fracture strength of ~130 GPa, and the ability to withstand a strain of ~25% before fracturing [16]. Furthermore, graphene's light mass, very high tensile strength, and very high endurance fatigue limit makes it ideal for high frequency applications [19].

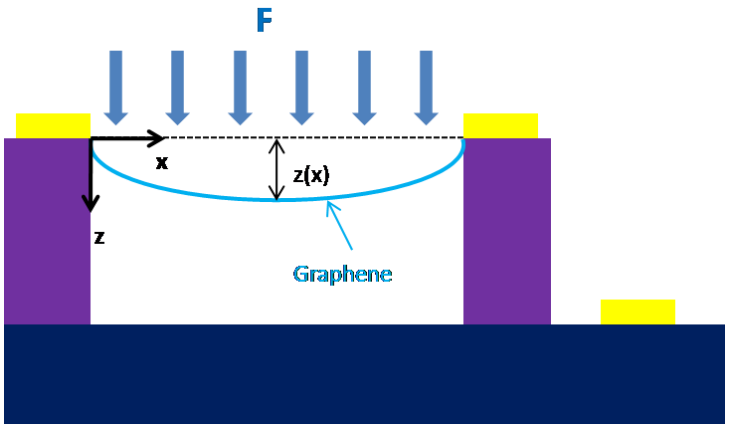

Fig. 5.2 Illustration showing the deflection in a simple graphene ribbon when a uniformly distributed force, F, is applied downwards.

In this section, we first outline how to use a suspended graphene ribbon resonator for high frequency DC-to-AC conversion. The resonator is a suspended graphene ribbon clamped at its two ends and held up above a conducting floor by layers of insulating material with an air gap in between, as shown in Fig. 5.2 [58], [64]. For this study, it is worth noting that we are not using the compliant mechanism ribbon designs presented in chapter 4; instead, we are using the simple straight doubly clamped ribbon design introduced in chapter. The electromechanical modeling, the device design criteria, and values of interest for high frequency power conversion applications are discussed.

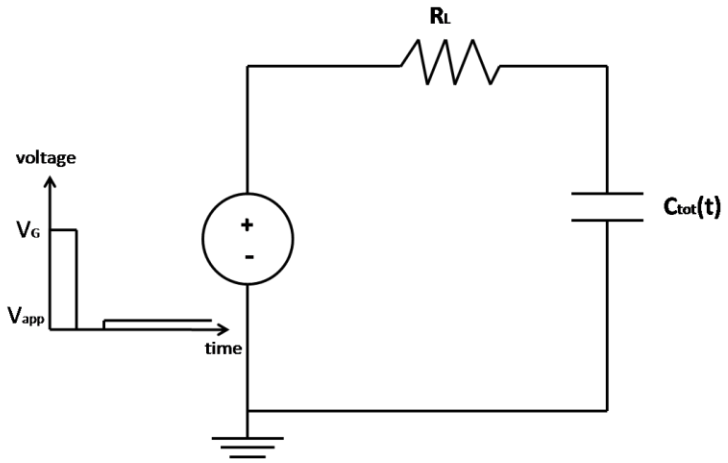

Fig. 5.3 A circuit diagram showing how DC-to-AC conversion is achieved using the suspended graphene resonator.

Fig. 5.3 is a circuit diagram showing how DC-to-AC conversion will be achieved. The graphene resonator is modeled as an oscillating capacitor with a total capacitance, C_{tot}, which will drive an oscillating voltage drop across the load resistor, R_L. C_{tot} takes into consideration both the classical and quantum capacitance, which will be explained in the section 5.2. The steps to obtain DC-to-AC conversion are as follows:

1. A gate voltage, V_G, is applied between the graphene and the floor, inducing an electrostatic force which bends the ribbon to its initial displacement. This will be when graphene reaches 10% strain, which is the generally accepted threshold before the onset of plastic deformation [85]. Going beyond the 10% strain threshold will lead to dislocations in graphene, which is undesirable if the resonator is to operate reliably.

2. V_G will be released, allowing the mechanical restoring force to cause the ribbon to oscillate. A value of R_L is chosen so that charging and discharging is effectively instantaneous.
3. As the ribbon oscillates, a lesser voltage, V_{app}, is applied such that the charge induced on the ribbon will not interfere with its oscillatory behavior. V_{app} is then held constant, which also causes a voltage drop across R_L.
4. The oscillating ribbon results in an oscillating capacitance and charge in the circuit. This ultimately drives an oscillating voltage drop across R_L, resulting in DC-to-AC conversion.

5.2 Electromechanical Modeling:

This section outlines how the suspended graphene resonator was electromechanically modeled and how values of interest in high frequency power conversion applications were extracted. The graphene ribbon was assumed to behave as a 1D elastic string with a finite width and thickness. The ribbon was also assumed to be made to oscillate using a uniformly applied force pushing it downwards in the vertical direction, as seen in Fig. 5.1. The vertical deflection as a function of x, z(x), is given by the following equation [86]:

$$z(x) = z_0 \left(\frac{4}{{L_0}^2}\right)\left[\left(\frac{{L_0}^2}{2}\right)^2 - x^2\right] \tag{5.1}$$

L_0 is the original length of the ribbon before any deflection and z_0 is the deflection at the midpoint of the ribbon. Eq. (5.1) indicates that if we know z_0, we also know the bending geometry; therefore, z_0 can be used to track how the ribbon bends as it oscillates and will be used

frequently in this section. The force was approximated as uniformly distributed because the difference in charge density in the ribbon for dimensions of interests is no more than ~2%.

To verify the force-deflection behavior predicted by the 1D elastic string model on the nano-material, the LAMMPS molecular dynamics software package was used (found at http://lammps.sandia.gov [87]). 4 nm x 4 nm area was chosen for the graphene sheet in our simulation because that was as much as the supercomputer we used could reasonably handle. The AIREBO potential was used to calculate intermolecular forces between individual carbon atoms [30], and a uniformly distributed pressure was gradually applied on the mobile domain of the ribbon to approximate static loading. Once equilibrated under the load, the atom positions were exported into MATLAB and a polynomial curve fit of the ribbon's curvature was performed.

The result of the LAMMPS simulation is shown in Fig. 5.4a. The deflections predicted by the 1D elastic string model and the LAMMPS simulation are compared in Fig. 5.4b. Fig. 5.4b shows that the disparity is small. The edges deviate from this behavior, but that area makes up a negligible amount in ribbons that have dimensions of interest. Therefore, the 1D elastic string model is valid and was used because it is much less computationally intensive than using LAMMPS simulations.

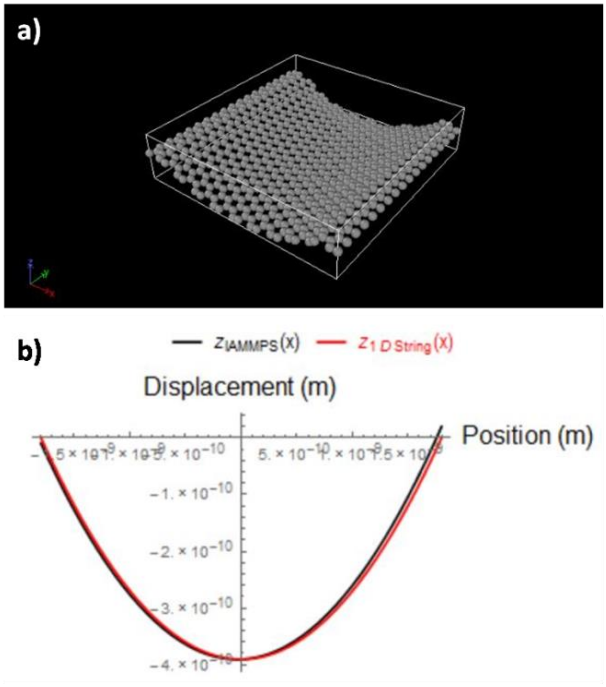

Fig. 5.4 a) LAMMPS simulation results. b) Plot of the z(x) function as predicted by the LAMMPS simulations and 1D elastic string model. The graphene ribbon in question has a length of 36 Å and a width of 40 Å. The LAMMPS simulation models the graphene sheet as a collection of carbon atoms, taking into consideration the interatomic forces among them, whereas 1D elastic string model considers graphene as a continuous film.

Using Eq. (5.1) from the 1D elastic string model, the ribbon's length, L, and classical capacitance, C_C, were calculated from the bending geometry by applying the arc-length formula [88]:

$$L[z_0] = \int_{-\frac{L_0}{2}}^{\frac{L_0}{2}} \sqrt{1 + \left(\frac{dz}{dx}\right)^2}\, dx \tag{5.2}$$

$$C_C[z_0] = \varepsilon_0 w \int_{-\frac{L_0}{2}}^{\frac{L_0}{2}} \frac{\sqrt{1+\left(\frac{dz}{dx}\right)^2}}{d_0 - z(x)} dx \tag{5.3}$$

ε_0 is the vacuum permittivity and w is the ribbon width. Eq. (5.2) and (5.3) indicate that by using z_0, we can track the length and classical capacitance as the ribbon oscillates.

It is important to note here that L and C_C are functionals of z_0 and can be calculated numerically only after a value of z_0 is given. To electromechanically model the device, it's useful to have L and C_C as simply functions of z_0, $L(z_0)$ and $C_C(z_0)$ respectively. In order to obtain these functions, a set of values for z_0 were generated in the range that we are concerned with. Then, L and C_C were calculated at each value and interpolating functions were extracted from those data points. Figure 5.5 illustrates an example of this for $L(z_0)$. $C_C(z_0)$ was obtained in a similar fashion.

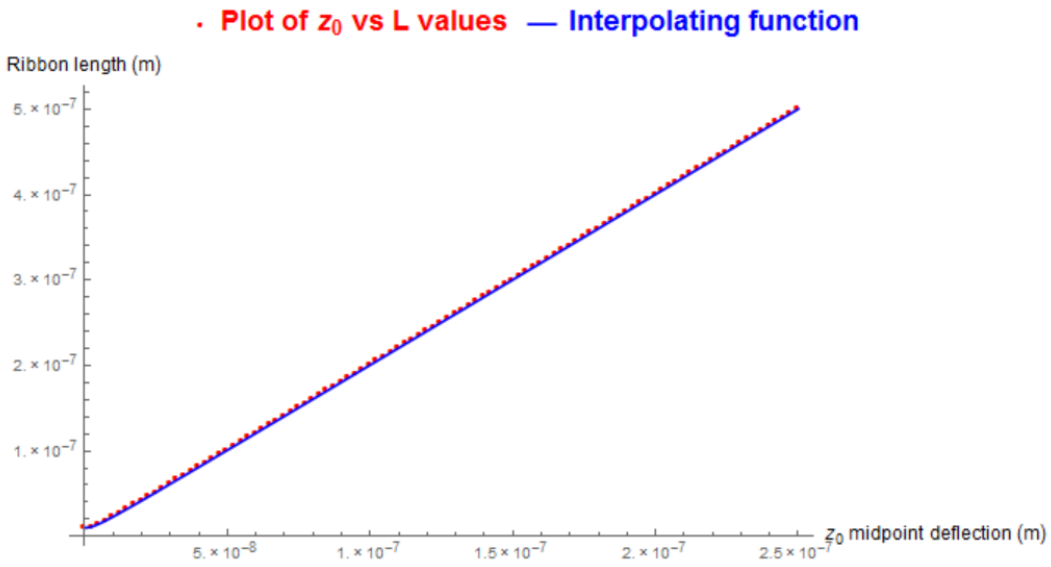

Fig. 5.5 A plot of the L vs. z_0 values and the interpolating function extracted from those values. Device dimensions: L_0 = 10 nm, width w = 10 nm, and trench depth d_0 = 1000 nm.

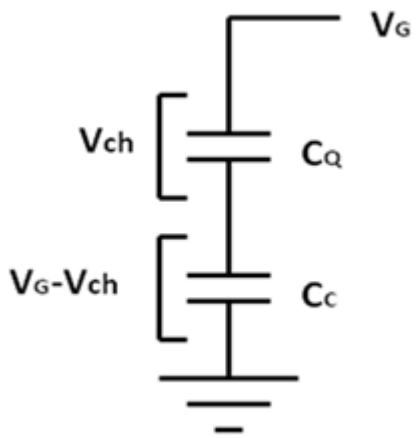

Fig. 5.6 Circuit diagram modeling the quantum and classical capacitance in suspended graphene.

Because graphene, a low density-of-states material, is one of our capacitor electrodes, its quantum capacitance, C_Q, was also taken into consideration. The generally accepted way to model the quantum capacitance is as an extra capacitance in series with the classical capacitance, as shown in Fig. 5.6. Then, C_Q is given by the following [89]:

$$C_Q(z_0) = \left(\frac{e^3}{(\hbar v_F)^2}\right)\left(\frac{2}{\pi}\right) wL(z_0)V_{ch}(z_0) \tag{5.4}$$

e is the electron charge, ħ is the reduced Plank's constant, v_F is the Fermi velocity (~ 10^5 m/s), and V_{ch} is the voltage drop across C_Q assuming the series capacitance model. By invoking charge conservation and knowing the bending geometry and the V_G, C_Q was numerically calculated. Knowing both C_C and C_Q yields the total capacitance, C_{tot}, which is needed for modeling the electrostatic force.

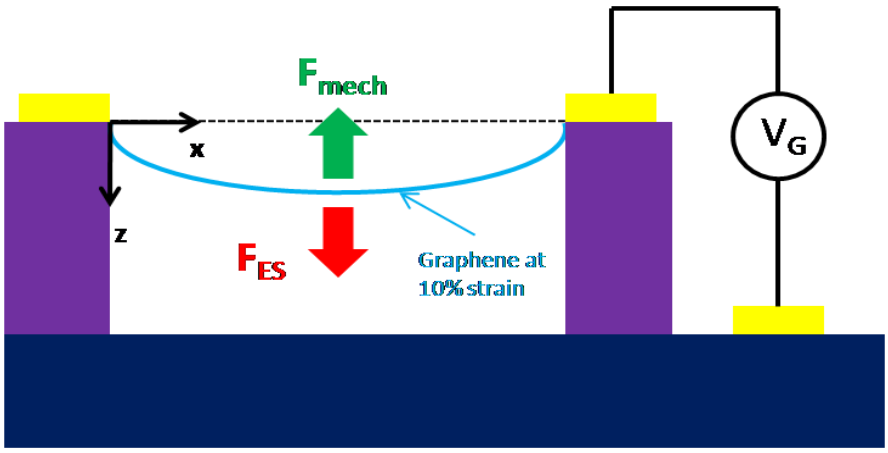

Fig. 5.7 Illustration of suspended graphene ribbon at equilibrium bent to 10% strain.

When V_G is applied to the ribbon, an electrostatic force, $F_{ES,}$ pulls it downwards and a mechanical restoring force, F_{mech}, acts in the opposite direction, as shown in Fig. 5.7. To determine V_G necessary to bend the ribbon to 10% strain, the ribbon in equilibrium was analyzed, captured by Eq. (5.5) and (5.6). F_{ES} and F_{mech} is given by the following [61], [86]:

$$F_{mech} = F_{ES} \tag{5.5}$$

$$\frac{256Ewtz_0{}^3}{9L^3} = \frac{1}{2}\frac{\partial C_{tot}}{\partial z_0}V_G{}^2 \tag{5.6}$$

Eq. (5.6) was solved numerically to calculate the V_G needed to bend the ribbon to 10% strain. Afterwards, the electrostatic force was released by dropping V_G to 0, allowing the ribbon to oscillate. Then, a smaller voltage, V_{app}, was applied such that the charge induced by it will not interfere with the ribbon's oscillation.

Our simulations indicate that $V_{app} = 0.1V_G$ suffices. This was found by solving the equations of motion when no voltage is applied and $V_{app} = 0.1V_G$ is applied and then comparing their solutions. The equations of motion are given below:

$$m\frac{d^2z_0}{dt^2} = -\frac{256Ewtz_0(t)^3}{9L^3} \tag{5.7}$$

$$m\frac{d^2z_0}{dt^2} = -\frac{256Ewtz_0(t)^3}{9L^3} + \frac{1}{2}\frac{\partial C_{tot}}{\partial z_0}{V_{app}}^2 \tag{5.8}$$

m is the mass of the ribbon. The solutions $z_0(t)$, midpoint deflections as a function of time, for the equation of motions above were obtained numerically and then were plotted and shown in Fig. 5.8 for comparison. In this figure, we can see that there is little disparity between the ribbon's oscillation governed by Eq. (5.7) and (5.8). Therefore, having $V_{app} = 0.1V_G$ would not interfere with the ribbons oscillation. This V_{app} is then held constant, allowing an oscillating voltage drop across R_L.

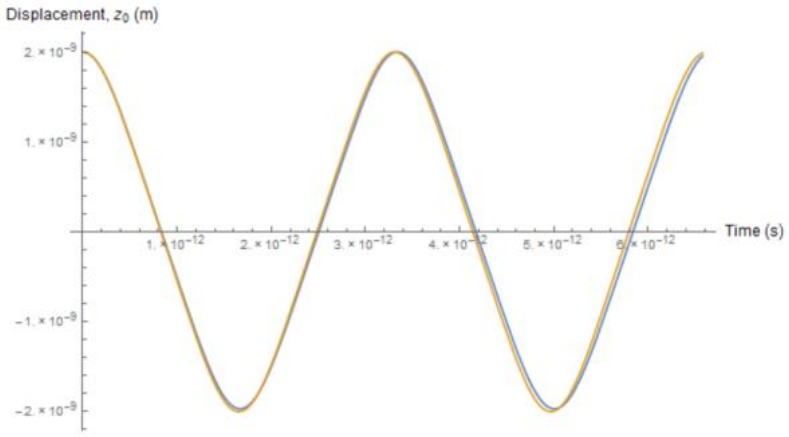

Fig. 5.8 Solutions $z_0(t)$ of Equation (5.7) and (5.8) plotted for comparison. The suspended graphene ribbon structure had the following dimensions: original length L_0 = 10 nm, width w = 10 nm, and trench depth d_0 = 1000 nm.

When applying $V_{app} = 0.1V_G$ and taking into consideration the classical and quantum capacitance of the graphene ribbon, the following differential equation was obtained using Kirchhoff's law and the circuit diagram in Fig. 5.2:

$$0 = 0.1V_G - \left(\frac{dQ}{dt}\right)R_L - \frac{Q(t)}{C_C(t)} - \frac{Q(t)}{C_Q(t)} \tag{5.9}$$

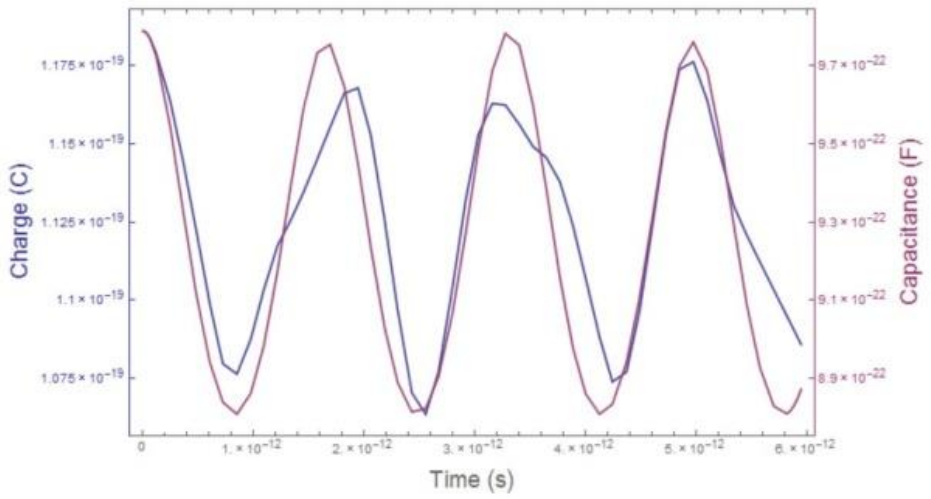

Fig. 5.9 A plot of Q(t) and $C_{tot}(t)$ for a suspended ribbon structure the following dimensions: L_0 = 10 nm, w = 10 nm, and d_0 = 1000 nm.

Eq. (5.9) was solved numerically for Q(t). The boundary condition Q(t=0) = 0 was used to solve it because it was assumed that the ribbon has completely discharged after releasing V_G. Fig. 5.9 shows Q(t) and $C_{tot}(t)$ on the same graph for a device with dimensions L_0 = 10 nm, w = 10 nm, and d_0 = 1000 nm as an example. This shows that the charge is in step with the capacitance, as expected. Lastly, the oscillating voltage drop across R_L, $V_R(t)$, can be calculated using Eq. 5.10:

$$V_R(t) = \left(\frac{dQ}{dt}\right) R_L \tag{5.10}$$

Using this algorithm, we calculated the following values of interest for high frequency power conversion applications: the oscillation frequency, absolute power generated, and the power conversion efficiency. The oscillation frequency, f, was calculated by taking the Fourier

transform of the signal and then identifying the dominant frequency. The absolute power generated, P_R, and power conversion efficiency, η, were calculated using Eq. (5.9) and (5.10) respectively:

$$P_R = \frac{{V_{R,RMS}}^2}{R_L} \tag{5.9}$$

$$\eta = \frac{V_{R,RMS}}{V_{app}} \tag{5.10}$$

$V_{R,RMS}$ is the root mean square voltage of the signal, which more appropriate than simply using the voltage if we have an oscillating signal.

5.3. Results and Discussion

This section discusses the results and their implications to high frequency power conversion applications. The primary value of interest for our application is the oscillation frequency; therefore, this value is discussed first. The results show that the oscillation frequency increases as the ribbon length decreases. This agrees with the 1D elastic string model because shorter ribbons are expected to be tauter. The oscillation frequencies for various ribbon lengths are summarized in Table 5.1. Our model indicates that lengths ranging from ~ 5 to 50 nm give oscillation frequencies within the THz gap. Although the best technology today can only achieve 10 nm feature lengths, 5 nm feature lengths may become a possibility by 2020 according to the International Technology Roadmap of Semiconductors [90]. This indicates that there is possibility that the graphene resonator device can cover a decent part of the THz gap in the near future.

L	5 μm	2 μm	1 μm	500 nm	200 nm
f	1.25 GHz	3.12 GHz	6.23 GHz	12.5 GHz	31.2 GHz
L	100 nm	50 nm	20 nm	10 nm	5 nm
f	62.3 GHz	125 GHz	312 GHz	623 GHz	1.25 THz

Table 5.1 Table summarizing oscillation frequencies for various suspended graphene ribbon lengths.

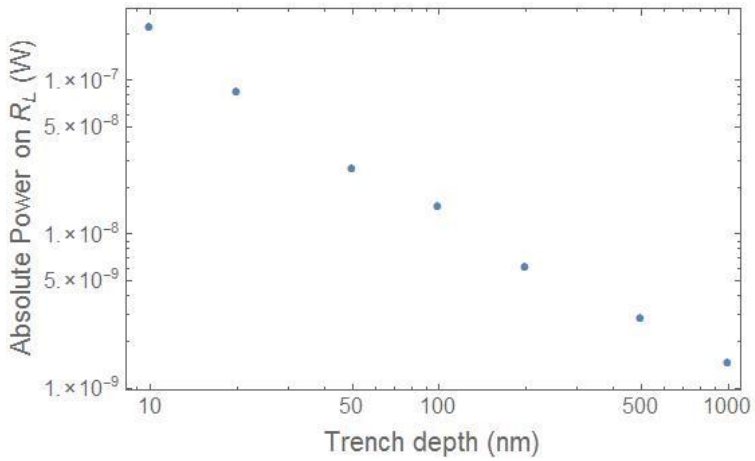

Fig. 5.10 A plot of the absolute power across the load resistor vs. the trench depth for a suspended graphene ribbon with L_0 = 10 nm and w = 10 nm.

Furthermore, the results show that the absolute power and conversion efficiency decreases with the trench depth. This is because as the trench depth increases, more voltage is dropped across the capacitor and less is dropped across R_L; therefore, less power is generated.

The absolute power for ribbons with L_0 = 10 nm, w = 10 nm, and various trench depths is plotted in Fig. 5.10 to illustrate this trend. The power conversion efficiency follows a similar trend

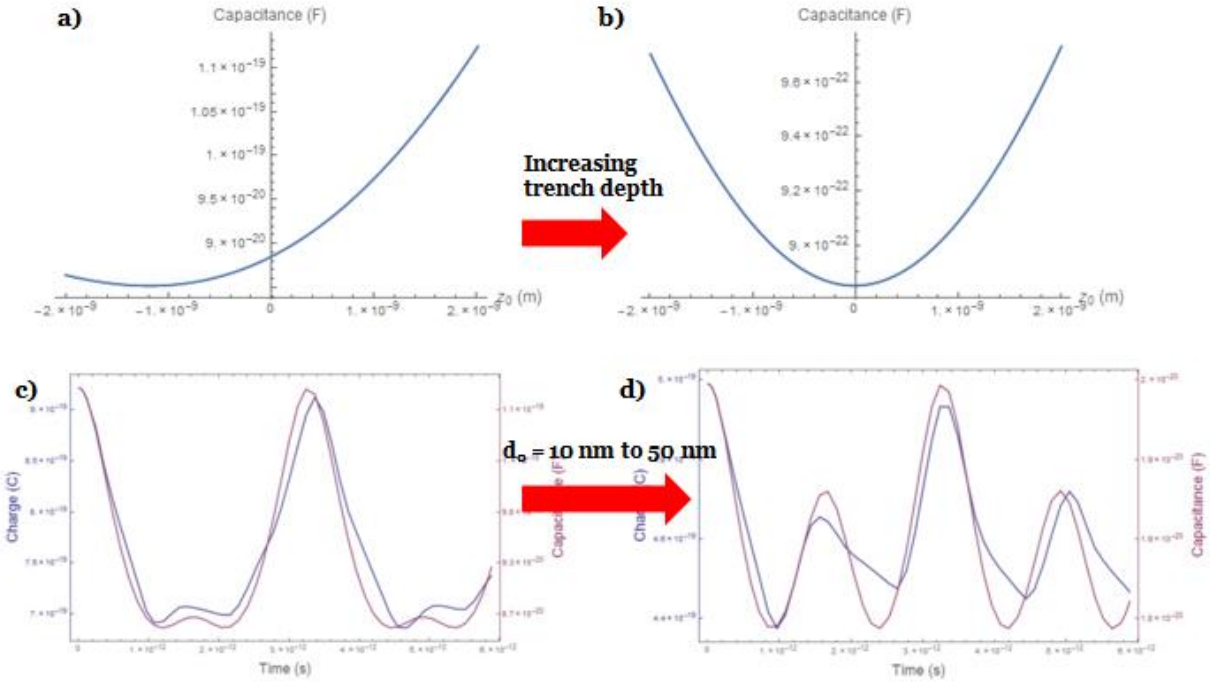

Fig. 5.11 a-b) Plots showing the decrease in capacitance asymmetry with increasing trench depth. c-d) Plots showing the decrease in height distortion with increasing trench depth.

These results suggest that the trench depth needs to be decreased as much as possible for high power generation. However, there is a tradeoff in that the signal becomes drastically distorted at sufficiently low trench depths. This is due to the capacitance being asymmetric when the trench depth is on the order of the ribbon length. This signal distortion phenomenon is illustrated in Fig. 5.11. Fig. 5.11a and 5.11b shows the capacitance as a function z_0 for a device with a relatively small trench depth and a relatively large trench depth respectively. From Fig. 5.11a, we can see that there is asymmetry about the y-axis for the small trench depth device. The

reason for this is as follows. As the ribbon bends towards the floor (z_0 advances in the positive direction), the capacitance increases as expected. However, as the ribbon bends away from the floor (z_0 advances in the negative direction), two variables that affect the capacitance compete with each other. The length increases, which increases the capacitance; however, the distance between the ribbon and floor also increases, which decreases the capacitance. The result is that the capacitance first decreases and then increases again as z_0 advances in the negative direction. At greater trench depths, the change in the distance between the ribbon and the floor make smaller contributions to the capacitance; therefore, as the trench depth increases, the capacitance asymmetry decreases, as seen in Fig. 5.11b.

This capacitance asymmetry causes a distortion in the capacitance as the ribbon oscillates over time. Because the charge follows the capacitance as the ribbon oscillates, this leads to a distorted signal. Fig. 5.11c and 5.11d show the capacitance and charge as a function of time for a small trench depth device and a slightly larger trench device respectively. As the trench depth increases, the capacitance asymmetry and signal distortion begins to disappear.

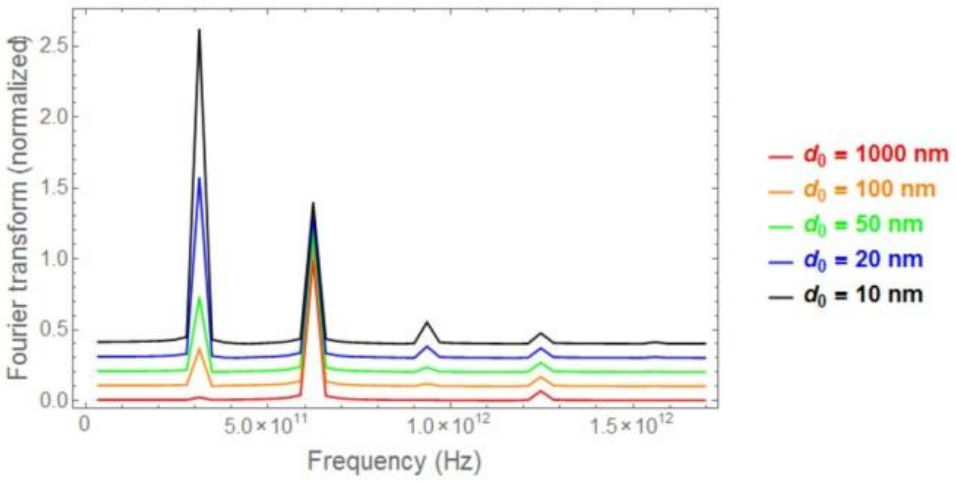

Fig. 5.12 Plots of the Fourier transforms of the capacitance for devices with L_0 = 10 nm, w = 10 nm, and varying trench depths. The amplitude at the expected oscillation frequency (623 GHz) was normalized to 1, and an offset is provided for easier comparison. As trench depth decreases, other frequencies become more dominant, especially the ~ 312 GHz frequency.

To characterize the degree of distortion, the capacitance for devices with varying trench depth were scrutinized. Their Fourier transforms were taken and how the dominant frequencies changed were tracked. Fig. 5.12 shows a plot of Fourier transforms for a device with an expected oscillation frequency of ~623 GHz and various trench depths. The amplitudes of the Fourier transforms at the expected oscillation frequency were normalized to 1, and an offset is provided for easier comparison. As the trench depth decreases, other frequencies, especially the ~312 GHz frequency, become more dominant, leading to a more distorted signal. To characterize the degree of distortion, the ratio between the expected frequency (~623 GHz) and the distortion frequency (~312 GHz) can be taken. In short, devices with smaller trench depths result in greater absolute power generated; however, smaller trench depths also lead to greater distortion in the signal.

These tradeoffs must be taken into account when designing suspended graphene resonators for high frequency applications, and the amount of distortion that is tolerable will ultimately depend on the specific application.

5.4 Conclusion

In conclusion, we presented a suspended graphene ribbon resonator that can be used for high frequency DC-to-AC conversion. Our model indicates that resonators made with sufficiently short ribbons (L_0 < about 50 nm) can achieve oscillation frequencies within the infamous THz gap. THz technologies have found diverse applications in fields including but not limited to communications, medical imaging, and homeland security. In communications, being able to operate within the THz gap will result in lower losses from weather conditions such as fog and the scintillation effect [91]. Medical imaging relies on the sensitivity of THz absorption to water content, allowing researchers to measure the degree of hydration and thus the disease state of human tissue. THz imaging studies on skin, breast, and colon cancer have already been conducted [92]. Even commercial security imaging systems use components that now operate at > 150 GHz [93]. Despite this, the technology available today has only barely begun to penetrate the THz gap. These fields and many more stand to gain through expanding available frequencies, and the proposed graphene resonator allows us to go one step further into the THz gap.

Chapter 6: Conclusion and Future Directions

Graphene is a carbon based material that is ideal to build MEMS devices with. It has an incredible Young's modulus, fracture strength, and flexibility. Furthermore, it is extremely conductive at room temperature, chemically inert, and exhibits a high endurance fatigue limit. For these reasons, we explored the electromechanical responses of suspended graphene and its applications by fabricating and studying MEMS devices made using suspended graphene ribbons. Also, in this dissertation, a survey of different growth and transfer methods were presented. We chose to use chemical vapor deposition due to its ability to grow large-area high quality polycrystalline graphene and polymer assisted wet transfer due to its costs and convenience.

We first explored the device's electrostatic discharge applications. The idea here was to use the suspended graphene device as a mechanical switch, acting as a trapdoor to shuttle stray charge away from vulnerable areas on IC chips. The device is hooked up so that when stray charge appears on the ribbon, an electrostatic force pulls graphene towards the floor (MEMS pull-in phenomenon). After contact, the floor acts as a sink for the charge. Once the charge has dissipated, the electrostatic force is released and the mechanical spring force of the ribbon ideally propels the ribbon back to its original suspended position. Fabricated devices underwent standard ESD industry testing and were shown to behave as predicted by theory. This shows that the device parameters can be tuned by change the device geometry, offering a novel and unique way of providing ESD protection. However, we also encountered a variation in the pull-in voltages, which we addressed later.

Despite our success with ESD applications, we encountered a reliability problem. Once the ribbon pull-in, the ribbon remains collapsed in contact with the floor. This is undesirable because the graphene ribbon is expected to re-suspend so that it is ready for the next ESD event and can operate reliably. To circumvent this issue, nail structures were proposed to pin down the graphene as the ribbon pulls in. Before implementing nails, finite element simulations were done to determine optimal nail structures and minimize the stress induced during pull-in. We found that the two circular nail structures were optimal and implemented them in future devices.

Another issue we countered was the variation in the pull-in voltage; thus, we conducted a study investigating the cause of it. We did this by first redesigning the ribbons using compliant mechanism designs. The flexures allowed greater flexibility and for the effective spring constant to be tuned. The large-area platform allowed us to easily measure the relative levels of polymer residue, which will be important later on. After redesigning the ribbons and fabricating a new batch of devices, we investigated the variation in different parameters that could potentially cause a variation in the pull-in voltage: trench depth, area, and thickness. After a thorough investigation and through process of elimination, we concluded that the variation in polymer residue thickness was the primary cause of the variation in the pull-in voltage. Graphene is 0.34 nm thick whereas polymer residue is usually a few nanometers thick; therefore, polymer residue could greatly affect suspended graphene's rigidity and thus pull-in voltage. However, by experimenting with more effective polymer residue removal methods, we found that graphene no longer suspends after reducing the polymer residue. It turns out that polymer residue creates a more rigid structure, which helps suspend graphene if the substrate is too corrugated. These findings have implications when manufacturing reliable suspended graphene devices with desired target parameter.

After conducting the experimental studies presented above, we decided to explore using the suspended graphene ribbon device for another potential application: a resonator for high frequency DC-to-AC conversion. We carried out a theoretical study electromechanically modeling the graphene resonator for this purpose. Our results indicated that the resonator's oscillation frequency increases as the ribbon length decreases; furthermore, we found that ribbon lengths of 5 to 50 nm can achieve oscillation frequencies that can penetrate the infamous THz gap. However, we also found a tradeoff between the power generated and signal quality, which both depend on the trench depth. If the trench depth is too high, then the power is low. If the trench depth is too low, there will be a capacitance asymmetry which leads to signal distortion. Therefore, these tradeoffs must be considered when designing resonators and the appropriate trench depth will depend on the specific application.

At last, what is left is work for the future. First, although we quantitatively assessed the effects of polymer residue on suspended graphene, there is still a knowledge gap in the literature on why the polymer residue that is few nanometers thick even exists. That is, adhesive interaction is expected between polymer and graphene only at the interface. Therefore, after polymer removal with a solvent, what we expect to remain should only be a one-layer thick polymer film on top of graphene instead of a multiple-layer film. The physical mechanism which causes the relatively thick polymer layer observed remains a mystery and will be explored in the future.

Second, there are a couple of changes we can make to our suspended graphene resonator model so that it is more realistic. First, the model we presented ignores friction. By including this, we expect the graphene resonator's oscillations to realistically damp over time. To remedy

this, a periodic pulse needs to be applied so that the oscillation amplitude remains above some minimum set threshold, which will again likely depend on the specific application the resonator is used for. All these factors must be taken into consideration so that our model is a faithful representation of reality.

Furthermore, there remains a host of unexplored graphene ribbon designs for the resonator. One such design is the “drum”, which is circular graphene sheet effectively clamped at all ends. This design is attractive for the following reasons: 1) being clamped at all ends makes the graphene sheet tauter, resulting in a higher achievable oscillation frequency for a given resolution limit, and 2) its simplicity allows for it to be easily fabricated. However, using a circular drum design eliminates a degree of freedom; that is, instead of being able to change the length and the width, we can only change the radius when using the drum design. Though, this issue can be circumvented by using an “ellipse”, which is yet another research avenue that can be explored. Finally, for the resonator to be useful fabrication is required, which is our ultimate goal.

Chapter 7: References

[1] A. K. Geim and K. S. Novoselov, "The rise of graphene," *Nat. Mater.*, vol. 6, no. 3, pp. 183–191, 2007.

[2] S. Iijima, "Direct observation of the tetrahedral bonding in graphitized carbon black by high resolution electron microscopy," *J. Cryst. Growth*, vol. 50, no. 3, pp. 675–683, 1980.

[3] X. Wang, Q. Li, J. Xie, Z. Jin, J. Wang, Y. Li, K. Jiang, and S. Fan, "Fabrication of ultralong and electrically uniform single-walled carbon nanotubes on clean substrates," *Nano Lett.*, vol. 9, no. 9, pp. 3137–3141, 2009.

[4] L. Landau, "Zur Theorie der Phasenumwandlungen II," *Phys. Z. Sowjet*, vol. 11, pp. 26–35, 1937.

[5] R. E. Peierls, "Quelques proprietes typiques des corpses solides," *Ann. I. H. Poincare*, vol. 5, no. 3, pp. 177–222, 1935.

[6] K. S. Novoselov, A. K. Geim, S. V Morozov, D. Jiang, Y. Zhang, S. V Dubonos, I. V Grigorieva, and A. A. Firsov, "Electric field effect in atomically thin carbon films.," *Science*, vol. 306, no. 5696, pp. 666–9, 2004.

[7] A. K. Sood, I. Lund, Y. R. Puri, H. Efstathiadis, P. Haldar, N. K. Dhar, J. Lewis, M. Dubey, E. Zakar, P. Wijewarnasuriya, D. L. Polla, and M. Fritze, *Review of Graphene Technology and Its Applications for Electronic Devices*. 2015.

[8] R. Arvidsson, D. Kushnir, S. Molander, and B. A. Sandén, "Energy and resource use assessment of graphene as a substitute for indium tin oxide in transparent electrodes," *J.*

Clean. Prod., vol. 132, pp. 289–297, 2015.

[9] C. I. L. Justino, A. R. Gomes, A. C. Freitas, A. C. Duarte, and T. A. P. Rocha-Santos, "Graphene based sensors and biosensors," *TrAC - Trends in Analytical Chemistry*, vol. 91. pp. 53–66, 2017.

[10] M. Lemme, "Current Status of Graphene Transistors," *Diffus. defect data. Solid state data. Part B*, pp. 1–12, 2010.

[11] A. H. . Castro Neto, N. M. R. . Peres, K. S. . Novoselov, A. K. . Geim, and F. Guinea, "The electronic properties of graphene," *Rev. Mod. Phys.*, vol. 81, no. 1, pp. 109–162, 2009.

[12] F. Schwierz, "Graphene transistors," *Nature Nanotechnology*, vol. 5, no. 7. pp. 487–496, 2010.

[13] C. Casiraghi, S. Pisana, K. S. Novoselov, A. K. Geim, and A. C. Ferrari, "Raman fingerprint of charged impurities in graphene," *Appl. Phys. Lett.*, vol. 91, no. 23, 2007.

[14] A. Das, S. Pisana, B. Chakraborty, S. Piscanec, S. K. Saha, U. V. Waghmare, K. S. Novoselov, H. R. Krishnamurthy, A. K. Geim, A. C. Ferrari, and A. K. Sood, "Monitoring dopants by Raman scattering in an electrochemically top-gated graphene transistor," *Nat. Nanotechnol.*, vol. 3, no. 4, pp. 210–215, 2008.

[15] D. Akinwande, C. J. Brennan, J. S. Bunch, P. Egberts, J. R. Felts, H. Gao, R. Huang, J. Kim, T. Li, Y. Li, K. M. Liechti, N. Lu, H. S. Park, E. J. Reed, P. Wang, B. I. Yakobson, T. Zhang, Y.-W. Zhang, Y. Zhou, and Y. Zhu, "A Review on Mechanics and Mechanical Properties of 2D Materials - Graphene and Beyond," *Extrem. Mech. Lett.*, vol. 13, pp. 42–

77, 2016.

[16] C. Lee, X. Wei, J. W. Kysar, and J. Hone, “Measurement of the elastic properties and intrinsic strength of monolayer graphene,” *Science (80-.).*, vol. 321, no. 5887, pp. 385–388, 2008.

[17] F. Liu, P. Ming, and J. Li, “Ab initio calculation of ideal strength and phonon instability of graphene under tension,” *Phys. Rev. B - Condens. Matter Mater. Phys.*, vol. 76, no. 6, 2007.

[18] X. Wei, B. Fragneaud, C. A. Marianetti, and J. W. Kysar, “Nonlinear elastic behavior of graphene: Ab initio calculations to continuum description,” *Phys. Rev. B - Condens. Matter Mater. Phys.*, vol. 80, no. 20, 2009.

[19] G. Paradee, “Fatigue Properties of Graphene Interconnects on Flexible Substrates,” vol. 15, no. 3, pp. 423–428, 2014.

[20] Y. Zhang, L. Zhang, and C. Zhou, “Review of chemical vapor deposition of graphene and related applications,” *Acc. Chem. Res.*, vol. 46, no. 10, pp. 2329–2339, 2013.

[21] P. Y. Huang, C. S. Ruiz-Vargas, A. M. Van Der Zande, W. S. Whitney, M. P. Levendorf, J. W. Kevek, S. Garg, J. S. Alden, C. J. Hustedt, Y. Zhu, J. Park, P. L. McEuen, and D. A. Muller, “Grains and grain boundaries in single-layer graphene atomic patchwork quilts,” *Nature*, vol. 469, no. 7330, pp. 389–392, 2011.

[22] A. Isacsson, A. W. Cummings, L. Colombo, L. Colombo, J. M. Kinaret, and S. Roche, “Scaling properties of polycrystalline graphene: A review,” *2D Mater.*, vol. 4, no. 1, 2017.

[23] I. Vlassiouk, S. Smirnov, I. Ivanov, P. F. Fulvio, S. Dai, H. Meyer, M. Chi, D. Hensley, P. Datskos, and N. V. Lavrik, "Electrical and thermal conductivity of low temperature CVD graphene: The effect of disorder," *Nanotechnology*, vol. 22, no. 27, 2011.

[24] A. W. Cummings, D. L. Duong, V. L. Nguyen, D. Van Tuan, J. Kotakoski, J. E. Barrios Vargas, Y. H. Lee, and S. Roche, "Charge transport in polycrystalline graphene: Challenges and opportunities," *Adv. Mater.*, vol. 26, no. 30, pp. 5079–5094, 2014.

[25] K. Yagi, A. Yamada, K. Hayashi, N. Harada, S. Sato, and N. Yokoyama, "Dependence of field-effect mobility of graphene grown by thermal chemical vapor deposition on its grain size," *Jpn. J. Appl. Phys.*, vol. 52, no. 11 PART 1, 2013.

[26] D. Lee, G. D. Kwon, J. H. Kim, E. Moyen, Y. H. Lee, S. Baik, and D. Pribat, "Significant enhancement of the electrical transport properties of graphene films by controlling the surface roughness of Cu foils before and during chemical vapor deposition," *Nanoscale*, vol. 6, no. 21, pp. 12943–12951, 2014.

[27] M. Yang, S. Sasaki, M. Ohnishi, K. Suzuki, and H. Miura, "Electronic properties and strain sensitivity of CVD-grown graphene with acetylene," *Jpn. J. Appl. Phys.*, vol. 55, no. 4, 2016.

[28] T. Wu, X. Zhang, Q. Yuan, J. Xue, G. Lu, Z. Liu, H. Wang, H. Wang, F. Ding, Q. Yu, X. Xie, and M. Jiang, "Fast growth of inch-sized single-crystalline graphene from a controlled single nucleus on Cu-Ni alloys," *Nat. Mater.*, vol. 15, no. 1, pp. 43–47, 2016.

[29] R. Grantab, V. B. Shenoy, and R. S. Ruoff, "Anomalous strength characteristics of tilt grain boundaries in graphene," *Science (80-.).*, vol. 330, no. 6006, pp. 946–948, 2010.

[30] Y. Wei, J. Wu, H. Yin, X. Shi, R. Yang, and M. Dresselhaus, “The nature of strength enhancement and weakening by pentagong-heptagon defects in graphene,” *Nat. Mater.*, vol. 11, no. 9, pp. 759–763, 2012.

[31] T. H. Liu, G. Gajewski, C. W. Pao, and C. C. Chang, “Structure, energy, and structural transformations of graphene grain boundaries from atomistic simulations,” *Carbon N. Y.*, vol. 49, no. 7, pp. 2306–2317, 2011.

[32] G. H. Lee, R. C. Cooper, S. J. An, S. Lee, A. Van Der Zande, N. Petrone, A. G. Hammerberg, C. Lee, B. Crawford, W. Oliver, J. W. Kysar, and J. Hone, “High-strength chemical-vapor-deposited graphene and grain boundaries,” *Science (80-.).*, vol. 340, no. 6136, pp. 1074–1076, 2013.

[33] J. Kotakoski, A. V. Krasheninnikov, U. Kaiser, and J. C. Meyer, “From point defects in graphene to two-dimensional amorphous carbon,” *Phys. Rev. Lett.*, vol. 106, no. 10, 2011.

[34] C. S. Ruiz-Vargas, H. L. Zhuang, P. Y. Huang, A. M. Van Der Zande, S. Garg, P. L. McEuen, D. A. Muller, R. G. Hennig, and J. Park, “Softened elastic response and unzipping in chemical vapor deposition graphene membranes,” *Nano Lett.*, vol. 11, no. 6, pp. 2259–2263, 2011.

[35] Y. Hernandez, V. Nicolosi, M. Lotya, F. M. Blighe, Z. Sun, S. De, I. T. McGovern, B. Holland, M. Byrne, Y. K. Gun’ko, J. J. Boland, P. Niraj, G. Duesberg, S. Krishnamurthy, R. Goodhue, J. Hutchison, V. Scardaci, A. C. Ferrari, and J. N. Coleman, “High-yield production of graphene by liquid-phase exfoliation of graphite,” *Nat. Nanotechnol.*, vol. 3, no. 9, pp. 563–568, 2008.

[36] S. N. Yannopoulos, A. Siokou, N. K. Nasikas, V. Dracopoulos, F. Ravani, and G. N. Papatheodorou, “CO2-Laser-Induced Growth of Epitaxial Graphene on 6H-SiC(0001),” *Adv. Funct. Mater.*, vol. 22, no. 1, pp. 113–120, 2012.

[37] J. Ng and Y.-H. Xie, “Source identification and method for drastic reduction of Fe contamination on wet transferred graphene,” *Thin Solid Films*, vol. 639, 2017.

[38] J. Ng, W. Zhang, Y.-H. Xie, Q. Chen, R. Ma, and A. Wang, “Optimization of suspended graphene NEMS devices for electrostatic discharge applications,” in *2017 IEEE 12th International Conference on Nano/Micro Engineered and Molecular Systems, NEMS 2017*, 2017.

[39] Lee, Park, and Whitesides, “Solvent compatibility of poly (dimethylsiloxane)-based microfluidic devices,” *Anal. Chem. Dc-*, vol. 75, no. 23, pp. 6544–6554, 2003.

[40] L. Jiao, B. Fan, X. Xian, Z. Wu, J. Zhang, and Z. Liu, “Creation of Nanostructures with Poly (methyl methacrylate) -Mediated Nanotransfer Printing,” *Society*, pp. 2–4, 2008.

[41] Z. Cheng, Q. Zhou, C. Wang, Q. Li, C. Wang, and Y. Fang, “Toward intrinsic graphene surfaces: A systematic study on thermal annealing and wet-chemical treatment of SiO2-supported graphene devices,” *Nano Lett.*, vol. 11, no. 2, pp. 767–771, 2011.

[42] W. W. Liu, J. N. Wang, and X. X. Wang, “Charging of unfunctionalized graphene in organic solvents,” *Nanoscale*, vol. 4, no. 2, pp. 425–428, 2012.

[43] K. S. Kim, Y. Zhao, H. Jang, S. Y. Lee, J. M. Kim, K. S. Kim, J. H. Ahn, P. Kim, J. Y. Choi, and B. H. Hong, “Large-scale pattern growth of graphene films for stretchable transparent electrodes,” *Nature*, vol. 457, no. 7230, pp. 706–710, 2009.

[44] J. D. Caldwell, T. J. Anderson, J. C. Culbertson, G. G. Jernigan, K. D. Hobart, F. J. Kub, M. J. Tadjer, J. L. Tedesco, J. K. Hite, M. A. Mastro, R. L. Myers-Ward, C. R. Eddy, P. M. Campbell, and D. K. Gaskill, "Technique for the dry transfer of epitaxial graphene onto arbitrary substrates," in *ACS Nano*, 2010, vol. 4, no. 2, pp. 1108–1114.

[45] S. Bae, H. Kim, Y. Lee, X. Xu, J. S. Park, Y. Zheng, J. Balakrishnan, T. Lei, H. Ri Kim, Y. Il Song, Y. J. Kim, K. S. Kim, B. Özyilmaz, J. H. Ahn, B. H. Hong, and S. Iijima, "Roll-to-roll production of 30-inch graphene films for transparent electrodes," *Nat. Nanotechnol.*, vol. 5, no. 8, pp. 574–578, 2010.

[46] J. Kang, S. Hwang, J. H. Kim, M. H. Kim, J. Ryu, S. J. Seo, B. H. Hong, M. K. Kim, and J. B. Choi, "Efficient transfer of large-area graphene films onto rigid substrates by hot pressing," *ACS Nano*, vol. 6, no. 6, pp. 5360–5365, 2012.

[47] A. C. Ferrari and D. M. Basko, "Raman spectroscopy as a versatile tool for studying the properties of graphene," *Nat. Nanotechnol.*, vol. 8, no. 4, pp. 235–246, 2013.

[48] P. Wang, M. Xia, O. Liang, K. Sun, A. F. Cipriano, T. Schroeder, H. Liu, and Y. H. Xie, "Label-Free SERS Selective Detection of Dopamine and Serotonin Using Graphene-Au Nanopyramid Heterostructure," *Anal. Chem.*, vol. 87, no. 20, pp. 10255–10261, 2015.

[49] "10 myths about electrostatic discharge in electronics manufacturing." .

[50] "Maxim leads the way in ESD protection." .

[51] A. Wang, *On-chip ESD protection for integrated circuits: an IC design perspective*, 1st ed. New York, NY: Kluwer Academic Publishers, 2001.

[52] E. Merrill, R and Issaq, “ESD Design Methodology,” *Proc. ESD/EOS Symp.*, pp. 233–237, 1993.

[53] O. N. Acosta, “Zener Diode - A Protecting Device Against Voltage Transients,” *IEEE Trans. Ind. Gen. Appl.*, vol. IGA-5, no. 4, pp. 481–488, 1969.

[54] Q. Chen, R. Ma, W. Zhang, F. Lu, C. Wang, O. Liang, F. Zhang, C. Li, H. Tang, Y. H. Xie, and A. Wang, “Systematic Characterization of Graphene ESD Interconnects for On-Chip ESD Protection,” *IEEE Trans. Electron Devices*, vol. 63, no. 8, pp. 3205–3212, 2016.

[55] W. Zhang, Q. Chen, M. Xia, R. Ma, F. Lu, C. Wang, A. Wang, and Y. H. Xie, “TLP evaluation of ESD protection capability of graphene micro-ribbons for ICs,” in *Proceedings - 2015 IEEE 11th International Conference on ASIC, ASICON 2015*, 2016.

[56] Q. Chen, C. Li, J. Ng, F. Lu, C. Wang, F. Zhang, R. Ma, Y.-H. Xie, and A. Wang, “Transient characterization of graphene NEMS switch ESD protection structures,” in *2017 IEEE Electron Devices Technology and Manufacturing Conference, EDTM 2017 - Proceedings*, 2017.

[57] W. Zhang, R. Ma, Q. Chen, M. Xia, J. Ng, A. Wang, and Y.-H. Xie, “The electro-mechanical responses of suspended graphene ribbons for electrostatic discharge applications,” *Appl. Phys. Lett.*, vol. 108, no. 15, 2016.

[58] W. Zhang, “The Electromechanical Responses of Suspended Graphene for Electrostatic Discharge Applications,” University of California Los Angeles, 2016.

[59] H. C. Nathanson, W. E. Newell, R. A. Wickstrom, and J. R. Davis, “The Resonant Gate

Transistor," *IEEE Trans. Electron Devices*, vol. ED-14, no. 3, pp. 117–133, 1967.

[60] W. M. Zhang, H. Yan, Z. K. Peng, and G. Meng, "Electrostatic pull-in instability in MEMS/NEMS: A review," *Sensors Actuators, A Phys.*, vol. 214, no. August, pp. 187–218, 2014.

[61] D. J. Griffiths, *Introduction to Electrodynamics*, 4th ed. Cambridge University Press, 2012.

[62] N. S. Barker, "Distributed MEMS Transmission Lines," University of Michigan, 1999.

[63] S. Pamidighantam, R. Puers, K. Baert, and H. A. C. Tilmans, "Pull-in voltage analysis of electrostatically actuated beam structures with xed- xed and xed-free end conditions, J," *Micromech. Microeng.*, vol. 12, pp. 458–464, 2002.

[64] J. Ng, Q. Chen, Y.-H. Xie, A. Wang, and T. Wu, "Comparative study between the fracture stress of poly-and single-crystalline graphene using a novel nanoelectromechanical system structure," *Micro Nano Lett.*, vol. 12, no. 11, 2017.

[65] W. Zhang, R. Ma, Q. Chen, M. Xia, J. Ng, A. Wang, and Y. H. Xie, "The electro-mechanical responses of suspended graphene ribbons for electrostatic discharge applications," *Appl. Phys. Lett.*, vol. 108, no. 15, 2016.

[66] A. Isacsson, A. W. Cummings, L. Colombo, L. Colombo, J. M. Kinaret, and S. Roche, "Scaling properties of polycrystalline graphene: A review," *2D Materials*, vol. 4, no. 1. 2017.

[67] K. S. Novoselov, A. K. Geim, S. V. Morozov, D. Jiang, M. I. Katsnelson, I. V.

Grigorieva, S. V. Dubonos, and A. A. Firsov, “Two-dimensional gas of massless Dirac fermions in graphene,” *Nature*, vol. 438, no. 7065, pp. 197–200, 2005.

[68] W. Choi, I. Lahiri, R. Seelaboyina, and Y. S. Kang, “Synthesis of graphene and its applications: A review,” *Crit. Rev. Solid State Mater. Sci.*, vol. 35, no. 1, pp. 52–71, 2010.

[69] C. Mattevi, H. Kim, and M. Chhowalla, “A review of chemical vapour deposition of graphene on copper,” *J. Mater. Chem.*, vol. 21, no. 10, pp. 3324–3334, 2011.

[70] X. Li, W. Cai, J. An, S. Kim, J. Nah, D. Yang, R. Piner, A. Velamakanni, I. Jung, E. Tutuc, S. K. Banerjee, L. Colombo, and R. S. Ruoff, “Large-area synthesis of high-quality and uniform graphene films on copper foils,” *Science (80-.).*, vol. 324, no. 5932, pp. 1312–1314, 2009.

[71] J. W. Suk, A. Kitt, C. W. Magnuson, Y. Hao, S. Ahmed, J. An, A. K. Swan, B. B. Goldberg, and R. S. Ruoff, “Transfer of CVD-grown monolayer graphene onto arbitrary substrates,” *ACS Nano*, vol. 5, no. 9, pp. 6916–6924, 2011.

[72] J. Kang, D. Shin, S. Bae, and B. H. Hong, “Graphene transfer: key for applications,” *Nanoscale*, vol. 4, no. 18, p. 5527, 2012.

[73] Y. C. Lin, C. C. Lu, C. H. Yeh, C. Jin, K. Suenaga, and P. W. Chiu, “Graphene annealing: How clean can it be?,” *Nano Lett.*, vol. 12, no. 1, pp. 414–419, 2012.

[74] X. Liu, N. G. Boddeti, M. R. Szpunar, L. Wang, M. A. Rodriguez, R. Long, J. Xiao, M. L. Dunn, and J. S. Bunch, “Observation of pull-in instability in graphene membranes under interfacial forces,” *Nano Lett.*, vol. 13, no. 5, pp. 2309–2313, 2013.

[75] L. L. Howell, S. P. Magleby, and B. M. Olsen, *Handbook of Compliant Mechanisms*. 2013.

[76] J. O. Jacobsen, B. G. Winder, L. L. Howell, and S. P. Magleby, "Lamina Emergent Mechanisms and Their Basic Elements," *J. Mech. Robot.*, vol. 2, no. 1, p. 011003, 2010.

[77] J. B. Hopkins and M. L. Culpepper, "Synthesis of precision serial flexure systems using freedom and constraint topologies (FACT)," *Precis. Eng.*, vol. 35, no. 4, pp. 638–649, 2011.

[78] F. Hartmann, "Castigliano's theorem and stiffness matrices," *Ingenieur-Archiv*, vol. 54, no. 3, pp. 182–187, 1984.

[79] H. Shioyama, "Interactions of two chemical species in the interlayer spacing of graphite," *Synth. Met.*, vol. 114, no. 1, pp. 1–15, 2000.

[80] U. Ali, K. J. B. A. Karim, and N. A. Buang, "A Review of the Properties and Applications of Poly (Methyl Methacrylate) (PMMA)," *Polymer Reviews*, vol. 55, no. 4. pp. 678–705, 2015.

[81] T. Li and Z. Zhang, "Substrate-regulated morphology of graphene," *J. Phys. D. Appl. Phys.*, vol. 43, no. 7, p. 075303, 2010.

[82] R. Kleiner, "Applied physics: Filling the terahertz gap," *Science*, vol. 318, no. 5854. pp. 1254–1255, 2007.

[83] L. E. Larson, R. H. Hackett, and R. F. Lohr, "Microactuators for GaAs-based microwave integrated circuits," in *TRANSDUCERS '91: 1991 International Conference on Solid-*

State Sensors and Actuators. Digest of Technical Papers, 1991, pp. 743–746.

[84] J. Oberhammer, "THz MEMS - Micromachining enabling new solutions at millimeter and submillimeter frequencies," in *2016 Global Symposium on Millimeter Waves, GSMM 2016 and ESA Workshop on Millimetre-Wave Technology and Applications*, 2016.

[85] S. Zhao and J. Xue, "Mechanical properties of hybrid graphene and hexagonal boron nitride sheets as revealed by molecular dynamic simulations," *J. Phys. D. Appl. Phys.*, vol. 46, no. 13, 2013.

[86] W. Weaver, S. Timoshenko, and D. H. Young, "Vibration problems in engineering," *Text*, vol. 207, no. 2, pp. 286–287, 1990.

[87] S. Plimpton, "Fast parallel algorithms for short-range molecular dynamics," *J. Comput. Phys.*, vol. 117, no. 1, pp. 1–19, 1995.

[88] J. Stewart, "Calculus, concepts and contexts," *Cole, Pacific Grove, CA*, p. 1131, 1998.

[89] S. Dröscher, P. Roulleau, F. Molitor, P. Studerus, C. Stampfer, K. Ensslin, and T. Ihn, "Quantum capacitance and density of states of graphene," *Appl. Phys. Lett.*, vol. 96, no. 15, pp. 98–101, 2010.

[90] ITRPV, "International Technology Roadmap for Semiconductors," 2016.

[91] J. Federici and L. Moeller, "Review of terahertz and subterahertz wireless communications," *Journal of Applied Physics*, vol. 107, no. 11. 2010.

[92] Q. Sun, Y. He, K. Liu, S. Fan, E. P. J. Parrott, and E. Pickwell-MacPherson, "Recent advances in terahertz technology for biomedical applications," *Quant. Imaging Med.*

Surg., vol. 7, no. 3, pp. 345–355, 2017.

[93] M. Tonouchi, “Cutting-edge terahertz technology,” *Nature Photonics*, vol. 1, no. 2. pp. 97–105, 2007.